

# University of Alberta

Nanophotonic detection of nanomechanical structures for use toward mass sensing applications

by

Vincent Theo Karel Sauer

A thesis submitted to the Faculty of Graduate Studies and Research  
in partial fulfillment of the requirements for the degree of

Doctor of Philosophy  
in  
Microsystems and Nanodevices

Department of Electrical and Computer Engineering

©Vincent Theo Karel Sauer  
Spring 2014  
Edmonton, Alberta

Permission is hereby granted to the University of Alberta Libraries to reproduce single copies of this thesis and to lend or sell such copies for private, scholarly or scientific research purposes only. Where the thesis is converted to, or otherwise made available in digital form, the University of Alberta will advise potential users of the thesis of these terms.

The author reserves all other publication and other rights in association with the copyright in the thesis and, except as herein before provided, neither the thesis nor any substantial portion thereof may be printed or otherwise reproduced in any material form whatsoever without the author's prior written permission.

*To Allison and my mom for their support throughout the years.*

# Abstract

Nanomechanical beam resonators show much promise for use in integrated on-chip mass sensing systems. This follows from their own very small masses and also their ability to store the mechanical energy of their oscillations to produce strong measurable mechanical response signals. To achieve higher mass sensitivities the size of these nanomechanical beams is decreasing and as a result the transduction of their mechanical motion is becoming more difficult. This follows from smaller nanomechanical devices operating at higher frequencies and with smaller ranges of motion. Nanophotonics is very well suited to measure devices with these properties in mind. Optical signals of nanoptomechanical system (NOMS) devices are not limited due to high frequency roll-off like traditional electronic measurement techniques, and they have exhibited very high mechanical displacement sensitivities. The nanophotonic transduction and actuation of nanomechanical cantilevers is demonstrated using integrated nanophotonic structures. Mach-Zehnder interferometer and nanophotonic racetrack resonator optical cavity transduction is demonstrated with good results for size independent nanomechanical cantilever beams. The devices are studied with the application of mass sensing in mind and multiplexed operation is demonstrated to mitigate the small capture area of individ-

ual nanomechanical beams. A nanostencil structure fabrication process is also developed using materials compatible with integrated optical systems. These overshield structures function to both protect the nanophotonic structures from uncontrolled analyte interactions along with removing the ambiguity of a mass loading event by eliminating uncertainty in mass loading location. This control of mass loading location can also be used to limit the deposition area of analyte on the beam to ensure maximum mechanical responsivity for each mass loading event. The NOMS detection method shows good promise for integrating nanomechanical beams into future mass sensing systems.

# Acknowledgments

I would first like to thank Dr. Wayne Hiebert who introduced me to the field of nanotechnology during my undergraduate research project all those years ago. He gave me the opportunity to continue the work first as his employee at the National Institute for Nanotechnology, and then through his capacity as a project leader during my time in graduate studies. I am not sure if I would have pursued a graduate degree if it wasn't for him. Wayne has been an excellent mentor throughout this entire process.

I would next like to thank the second mentor who guided me along this path. Dr. Mark Freeman co-hired me during my time at NINT and subsequently became my co-supervisor for my doctoral degree. I will forever be grateful for the opportunities you provided which have allowed me to freely pursue my academic goals.

The final mentor I would like to thank is Dr. Ying Tsui. As my other co-supervisor you opened up many new doors for me and ensured I took advantage of every possible opportunity. I extremely appreciate your knowledge and guidance on both the technical and non-technical aspects of my studies.

I feel all three of you took a chance on me back when I started, and I hope you all realize how lucky I am to have worked with you during my degree. You have provided me with the freedom to pursue my goals and the guidance to help achieve them. I cannot imagine working for a better group of people.

Next, I would like to thank all my colleagues who helped me along the way. I have had the opportunity to work with many excellent people and for that I

am grateful. I would especially like to thank Zhu Diao for his hard work and our many fruitful discussions regarding the project.

I would like to thank the staff at the University of Alberta nanoFAB not only for their training but also for their upkeep of the facility. It made my life much easier to only have to worry about device designs and processes and not about fixing or maintaining any of the fabrication systems. I would also like to thank the technical staff at the National Institute for Nanotechnology, specifically the staff in the electron microscopy group and the cleanroom facility. It would have been much more difficult to complete any of my projects without your expertise. I would lastly like to thank CMC Microsystems for their design competition programs which have allowed my later sets of samples to be fabricated at a professional foundry.

A final thank you goes to all of the institutions and funding agencies which have financially supported my research throughout the years. This includes the University of Alberta and the National Institute for Nanotechnology, along with Alberta Innovates Technology Futures, the National Research and Science Council of Canada, the informatics Circle of Research Excellence (iCORE), the Canadian Institute for Advanced Research, and the Canada Research Chairs.

# Contents

<b>1</b>	<b>Introduction</b>	<b>1</b>
<b>2</b>	<b>Nanomechanical mass sensing</b>	<b>5</b>
2.1	Introduction . . . . .	5
2.2	Nanomechanical resonant frequency . . . . .	6
2.2.1	Mechanical resonator boundary conditions . . . . .	7
2.2.2	Mode shape of a resonant beam . . . . .	8
2.3	Frequency shift of a resonator due to the addition of a point mass	9
2.4	Harmonic motion . . . . .	11
2.4.1	Simple harmonic motion . . . . .	11
2.4.2	Damped harmonic motion . . . . .	11
2.5	Effective mass of a resonating beam . . . . .	12
2.6	Estimating the mass sensitivity of a nanomechanical beam resonator . . . . .	14
2.7	Conclusion . . . . .	15

<b>3</b>	<b>Nanophotonics</b>	<b>17</b>
3.1	Introduction . . . . .	17
3.2	Light coupling from an optical fiber to an optical chip . . . . .	18
3.3	On-chip light propagation . . . . .	20
3.4	Integrated optical devices for nanomechanical beam interaction	23
3.4.1	Effective index of refraction . . . . .	23
3.4.2	Waveguide based transduction schemes . . . . .	25
3.4.3	Optical cavity based transduction schemes . . . . .	27
3.5	Integrated optical actuation . . . . .	28
3.6	Conclusion . . . . .	29
<b>4</b>	<b>Experimental Setup</b>	<b>31</b>
4.1	Confocal laser scanning system for nanophotonic chip coupling	31
4.2	Pump probe optical setup . . . . .	33
<b>5</b>	<b>MZI detection of cantilevers</b>	<b>36</b>
5.1	Introduction . . . . .	36
5.2	Device design and fabrication . . . . .	37
5.3	MZI device detection . . . . .	41
5.4	MZI device optomechanical calculations . . . . .	45
5.5	MZI NOMS pump probe . . . . .	47
5.6	MZI readout discussion . . . . .	49
5.7	Conclusion . . . . .	50

<b>6</b>	<b>Racetrack resonator transduction</b>	<b>52</b>
6.1	Introduction . . . . .	52
6.2	Nano-optomechanical system geometry . . . . .	53
6.3	Derivation of the nanophotonic transduction responsivity . . . . .	54
6.4	Extraction of absolute displacement and the $g_{om}$ . . . . .	56
6.5	Device fabrication . . . . .	57
6.5.1	Measurement system . . . . .	61
6.6	Thermomechanical noise measurements, analysis and $g_{om}$ extraction . . . . .	62
6.7	Optical pump and probe measurements . . . . .	65
6.8	Atmospheric pressure thermomechanical noise measurement . . . . .	68
6.9	Discussion on the optomechanical transduction and mass sensitivity . . . . .	70
6.10	Consideration of other effects on the transduction responsivity . . . . .	72
6.11	Future perspectives . . . . .	74
6.12	Conclusion . . . . .	75
<b>7</b>	<b>Multiplexing using NOMS</b>	<b>77</b>
7.1	Introduction . . . . .	77
7.2	Multiplex NOMS device design . . . . .	78
7.3	Wavelength-division multiplexing measurements . . . . .	80
7.4	Determining the probe channel of individual nanomechanical resonators . . . . .	83
7.5	Conclusion . . . . .	84

<b>8</b>	<b>DOME structures</b>	<b>87</b>
8.1	Introduction . . . . .	87
8.2	DOME structure fabrication . . . . .	88
8.3	Characterization . . . . .	92
8.4	Discussion . . . . .	96
8.5	Conclusion . . . . .	100
<b>9</b>	<b>Future Work</b>	<b>101</b>
9.1	Introduction . . . . .	101
9.2	Basic mass measurements . . . . .	102
9.3	Nanophotonic DOME integration . . . . .	104
9.4	Advanced mass detection . . . . .	105
9.5	Conclusion . . . . .	107
<b>10</b>	<b>Conclusion</b>	<b>108</b>
	<b>Bibliography</b>	<b>111</b>
	<b>Appendices</b>	<b>122</b>
<b>A</b>	<b>Publications</b>	<b>123</b>
A.1	Archival Journal . . . . .	123
A.1.1	Published . . . . .	123
A.1.2	In review . . . . .	125
A.2	Book Chapters . . . . .	125
A.2.1	In review . . . . .	125
A.3	Selected conference presentations . . . . .	126

# List of Tables

2.1	Consecutive roots of beam frequency equations . . . . .	8
5.1	List of cantilever dimensions, resonant frequencies, and mechanical quality factors . . . . .	44
8.1	Mechanical response of doubly clamped beam DOME devices .	96

# List of Figures

3.1	Channel waveguide types . . . . .	22
3.2	Schematic for solving using the effective index method . . . . .	25
4.1	Confocal laser scanning nanophotonics probe setup . . . . .	33
4.2	NOMS pump and probe schematic . . . . .	34
5.1	SEM of MZI cantilever detection device . . . . .	39
5.2	Optical mode simulation of a MZI waveguide arm and adjacent cantilever . . . . .	40
5.3	DC optical wavelength scan of an MZI structure . . . . .	42
5.4	Mechanical frequency response of a MZI transduced cantilever . . . . .	43
5.5	Phase detection scheme verification for MZI device . . . . .	46
5.6	All optical nanomechanical pump/probe with MZI NOMS . . . . .	48
6.1	Racetrack resonator optical DC transmission curve . . . . .	54
6.2	SEM of racetrack resonator cantilever NOMS . . . . .	59
6.3	Optical mode simulation of racetrack resonator . . . . .	60
6.4	TM response of racetrack detected cantilever . . . . .	63
6.5	TM signal strength of cantilevers of varying length and gap spacing . . . . .	64
6.6	Extracted optomechanical coupling constants from TM noise . . . . .	65

6.7	Thermomechanical cantilever tip displacement . . . . .	66
6.8	Optical pump and probe cantilever mechanical response . . . .	67
6.9	TM noise detection of cantilever at atmosphere . . . . .	69
7.1	SEM of multiplexed NOMS devices . . . . .	80
7.2	DC transmission spectrum of a multiplexed racetrack resonators	81
7.3	TM noise response of a multiplexed device at different probe wavelengths . . . . .	82
7.4	Selective heating used determine the mechanical beam probe wavelengths . . . . .	85
8.1	DOME structure fabrication process flow . . . . .	89
8.2	DOME structure exploded view . . . . .	92
8.3	DOME structure SEM . . . . .	93
8.4	Mechanical response of doubly clamped beam with a DOME structure . . . . .	95
8.5	Q-factors of DOME structures . . . . .	97
8.6	Evaporation onto a DOME structure . . . . .	98

# List of Symbols

$A$	cross sectional area of a beam . . . . .	7
$E$	Young's modulus . . . . .	7
$I$	second moment of area of a beam. . . . .	7
$Q$	mechanical quality factor . . . . .	12
$T_0$	power entering optical resonator . . . . .	55
$\alpha$	extinction ratio of optical resonance dip measured in dB . . . . .	55
$\beta$	nanomechanical beam displacement factor . . . . .	46
$\chi$	proportional length of the beam to the optical cavity length. . . . .	55
$\lambda$	free space nanophotonic probe wavelength . . . . .	45
$\mathfrak{F}$	finesse of the optical cavity . . . . .	52
$\mathfrak{R}$	mass responsivity. . . . .	15
$\omega$	angular mechanical resonant frequency of beam . . . . .	7
$\omega_{\text{opt}}$	optical frequency of the waveguide eigenmode. . . . .	28
$\omega_{n,\Delta m}$	frequency of combined beam - particle system. . . . .	10
$\rho$	mass density . . . . .	7
$a$	peak amplitude of beam oscillation . . . . .	7
$f$	mechanical resonant frequency of a beam . . . . .	8
$g$	waveguide-resonator gap spacing . . . . .	45

$g_{\text{om}}$	optomechanical coupling constant . . . . .	29
$k_y$	spring constant of the beam . . . . .	13
$l$	nanomechanical beam length . . . . .	6
$l_c$	optical cavity length . . . . .	55
$m_{\text{eff}}$	effective mass of a resonator beam . . . . .	13
$n_{\text{eff}}$	effective index of refraction of the optical mode . . . . .	45
$t$	beam thickness in the oscillating direction . . . . .	8
$w$	beam width perpendicular to direction of oscillation . . . . .	8
$\Delta m$	mass of the analyte particle . . . . .	10
$m_{\text{beam}}$	mass of the vibrating beam . . . . .	10

---

---

# CHAPTER 1

---

## Introduction

Rapid advances during this information age have brought many new technologies to the forefront. One example includes nanotechnology. Colloquial representation of the field includes microscopic robots floating around and manipulating objects a single molecule at a time. The technology has not yet progressed this far, and it's arguable as to whether it ever will, but what nanotechnology has become is an enabling technology.

Nanotechnology is a broad reaching field encompassing all aspects of science. If someone asks a chemist to define and describe it chances are they would give a very different answer than a physicist might. What can be agreed upon is that material and device properties change when working in the nanoscale. Access to these new properties is what is driving advances in the field.

Devices utilizing nanotechnology also give access to new paradigms of interaction with microscopic materials. Devices are now being built at size scales matching those of proteins, molecules and atoms and can interact with them directly. Since the fabrication of many nanotechnological devices and structures stems from integrated circuit fabrication processes, this new interaction paradigm is enabling the miniaturization of many existing larger scale devices onto much smaller computer chips.

One such device is the mass spectrometer. A mass spectrometer measures

the charge to mass ratio of an analyte material and based on this value is able to determine what the material is. Traditional mass spectrometers can detect masses below that of a single proton, and are generally large pieces of equipment which utilize strong electric and magnetic fields. As a result they are not very portable. Due to their cost, scientists will submit their samples to an outside lab for mass spectrometry analysis and not typically have a machine of their own. Using nanotechnology, however, new devices are being developed which could transform this large expensive piece of equipment into something that may fit in the palm of one's hand.

These devices are based on the fabrication of nanomechanical vibrating beams. These beam are created on a size scale where their direct interaction with analyte molecules may be measured. Generally, the frequency of oscillation of the nanomechanical beam is measured and a foreign mass landing on the beam changes this frequency in proportion to its size. In pursuing the highest mass sensitivity of these nanomechanical sensors the sizes of the resonating beams have become increasingly smaller. Although this decrease in device mass often leads to higher sensitivities [1] the transduction of the motion of the beam becomes more difficult to achieve. Advances in the nanomechanical sensing field have followed new device structures and transduction techniques. The work in this thesis follows this trend by fabricating novel nanomechanical resonating beam devices with mass sensing applications in mind.

The transduction difficulties of smaller devices may be caused by several issues. Expected displacements of nanomechanical beams generally decrease with smaller beam sizes so displacement sensitivities must improve as well. Very high displacement sensitivities are achieved with conventional free-space optics, but the method is diffraction limited which imposes minimum size constraints when probing nanomechanical devices [2, 3]. Constraints can also emerge with smaller devices as they tend to operate at higher mechanical frequencies [4]. Issues such as RLC roll-off and parasitic capacitance can negatively affect the transduction when using certain electronic read-out techniques.

Nano-optomechanical system (NOMS) devices have emerged as an excellent option for overcoming these issues to effectively transduce nanomechanical motion. This follows from their unprecedented displacement sensitivity [5, 6]. The use of on-chip optical cavities also allow transduction improvement as photons contained within the cavities can interact multiple times with the nanomechanical device before dissipation [7]. Diffraction limits are circumvented as the devices operate in the optical near-field, and the optical detection scheme, which is neither frequency nor bandwidth limited, is well suited for high frequency operation [5]. This work follows this rationale to both fabricate and study nanomechanical beam resonators which use nanophotonic structures for mechanical signal transduction. Practical implementation of the device into a mass sensing setup is also considered in relation to the design.

Some of the recent advances in the optomechanical field have used these integrated NOMS devices to conduct some truly astounding work. Foremost, this includes studies at the quantum limit [8, 9, 10]. These experiments monitor the mechanical motion of the integrated high quality optical cavity itself and take advantage of the direct coupling between the mechanical modes of motion and the cavity's optical properties. Optical cooling is also employed in these systems. Photonic crystal optical cavities and their mechanical breathing modes are especially useful to investigate such systems. These types of structures have also been used to monitor other physical phenomena such as the generation of squeezed light [11] and nano-optomechanical wavelength conversion [12]. Coupling between microwave electrical signals and optical photons has also been demonstrated through a piezoelectric optomechanical photonic crystal cavity [13]. These piezoelectric crystal cavity structures have been engineered for both high optical and mechanical quality factors to better couple electrical systems with these nano-optomechanical system devices [14, 15]. Integrated nano-optomechanical system devices are opening up many new avenues for studying interactions on a fundamental level.

Although these devices have demonstrated unprecedented sensitivity they may not be well suited for sensing external particles due to the nature of their oper-

ation. The devices are generally designed to interact only with themselves and external entities may induce losses in the system which could destroy the device's inherent sensitivity. As an example, a device relying on the high optical quality factor of a photonic crystal cavity would become ineffective if a foreign material is deposited on the cavity which scatters the optical mode. Following this rationale, this work will look at NOMS systems where the optical and mechanical structures are physically separated. The optical and mechanical interactions will not be as strong, and hence the mechanical motion sensitivity will not be as high, but the design should be more robust for external analyte detection.

Nanomechanical mass sensors using nanophotonic transduction have the potential to impact all fields which require particle analysis. With this technology, hand-held mass spectrometry systems may be possible due to the nanofabrication platform with large scale integration possibilities. This could lead to nanomechanical-based mass spectrometers replacing the large expensive systems used today. As a result, they could be integrated into lab-on-a-chip systems to make diagnostic tests more accessible, faster and less expensive. Chemical and biological analysis could be done instantaneously in individual labs or in the field. This added accessibility to mass spectrometry systems could see them become a standard tool wherever particle analysis is needed.

---

---

## CHAPTER 2

---

### Nanomechanical mass sensing

#### 2.1 Introduction

Nanomechanical resonating beams have been studied for many years for applications in on-chip mass sensing. There are two important reasons for this [1]. The first reason is that nanomechanical beams have very small masses which, in turn, allow them to detect very small masses. The second reason follows from their high mechanical quality factors and high signal to noise ratios. These parameters allow for a very accurate measurement of the mechanical device's resonant frequency. In dynamic mass sensing measurements this mechanical resonant frequency is the property used to extract the mass of the analyte particle. These types of dynamic mass measurements are discussed in detail in this chapter.

The ultimate sensitivity goal for on-chip nanomechanical mass sensors is reaching the sub-dalton regime. This coincides with the sensitivity of traditional mass spectrometry systems and allows for the differentiation of different proteins based on mass alone. A nanomechanical resonator device fabricated using a carbon nanotube has reached this sensitivity level [16] and confirmed earlier theoretical predictions on its possibility [17, 18]. An advantage of nanomechanical mass sensors compared to traditional mass spectrometers is that no analyte

ionization is required. Neutral species measurement removes the requirement for analyte ionization which can damage fragile proteins and molecules.

Other than mass spectrometry [19, 20, 21] nanomechanical mass sensors have been used as more general sensors to measure few numbers of atomic masses [22, 23, 24], single particles in the gas phase [25], analytes in gas chromatography systems [26, 27], and also particles in a fluid environment [28, 29, 30]. With any of these sensor types a distinct advantage of a nanomechanical system compared to conventional methods is the ability to integrate a large number of these devices onto a single chip. The high sensitivity and the ability to manufacture them integrated with computer chip components open the possibility of using these devices in inexpensive and portable sensor systems.

## 2.2 Nanomechanical resonant frequency

The mechanical resonant frequency of a nanomechanical beam is dependent on its physical characteristics such as its size, shape and composition. If one of these properties is altered the resonant frequency will change, and this is the principle of operation for gravimetric mass sensing. A foreign analyte mass is added to the mechanical beam and, assuming secondary effects are negligible, this change in the overall mass of the oscillating structure (now composed of the beam *and* the added mass) changes the resonant frequency [18]. To first find a mechanical beam's resonant frequency, Timoshenko beam theory is considered.

Looking at a prismatic beam in the  $x - y$  plane with the beam length,  $l$ , along the  $x$ -axis and deflection in the  $y$  direction the general equation for the beam's free vibration can be derived according to the free body diagram of a beam element,  $dx$  [31]:

$$EI \frac{\partial^4 y}{\partial x^4} dx = -\rho A dx \frac{\partial^2 y}{\partial t^2} \quad (2.1)$$

In the formula above  $E$  is the Young's modulus of the beam and  $I$  is the second moment of area of the beam such that  $EI$  corresponds to the beam's flexural rigidity. The mass density is defined by  $\rho$  and the cross-sectional area is  $A$ . Now, assuming that the deflection varies harmonically, let  $y(x, t) = aY(x)e^{i\omega t}$  where  $a$  is equal to the peak amplitude and  $\omega$  is equal to the angular frequency. Equation 2.1 can then be simplified to:

$$\frac{\partial^4 Y(x)}{\partial x^4} = \beta^4 Y(x) \quad (2.2)$$

where

$$\beta^4 = \frac{\rho A \omega^2}{EI} \quad (2.3)$$

A general solution for this partial differential equation, and hence the typical function representing transverse prismatic beam vibrations, is:

$$Y(x) = C_1 \sin \beta x + C_2 \cos \beta x + C_3 \sinh \beta x + C_4 \cosh \beta x \quad (2.4)$$

To solve for the angular resonant frequency,  $\omega$ , the equation must be solved using the beam's boundary conditions. These boundary conditions are set by the type of mechanical resonator such as if it is a cantilever or a doubly clamped beam.

### 2.2.1 Mechanical resonator boundary conditions

The boundary conditions are set by how the vibrating beam is clamped. Obviously  $Y$  represents the displacement and will be equal to zero if the beam is clamped. If the device is clamped the slope of the beam,  $Y'$ , will also be equal to zero assuming it is clamped perpendicular to the anchor.  $Y''$  and  $Y'''$  represent the bending moment and the shear force, respectively, and both will be equal to zero for a freely oscillating end.

Looking at the specific case of a cantilever beam (one clamped end, one free end) equation 2.4 reduces to the following:

$$\cos \beta l \cosh \beta l = -1 \quad (2.5)$$

and in the case of a doubly clamped beam (both ends clamped):

$$\cos \beta l \cosh \beta l = 1 \quad (2.6)$$

The solutions for these equations are listed in table 2.1.

Table 2.1: Consecutive roots of beam frequency equations

	$\beta_1 l$	$\beta_2 l$	$\beta_3 l$
cantilever	1.875	4.694	7.855
doubly clamped	4.730	7.853	10.996

Using these roots the resonant frequencies of a beam's different modes can now be calculated. Using equation 2.3 and the second moment of area of a rectangular beam  $I = wt^3/12$ , where  $w$  is the beam width perpendicular to the oscillating direction and  $t$  is the beam thickness in the oscillating direction, the resonant frequency,  $f$ , for a nanomechanical resonator is expressed as the following with  $\beta l = \gamma$ :

$$f = \frac{\beta^2 t}{2\pi} \sqrt{\frac{E}{12\rho}} = \frac{\gamma^2 t}{2\pi l^2} \sqrt{\frac{E}{12\rho}} \quad (2.7)$$

### 2.2.2 Mode shape of a resonant beam

The shape of the oscillating beam is also derived from the general beam equation. Taking the boundary condition of a clamping point at  $x = 0$  (for either a

cantilever or doubly clamped beam) it is found that  $C_1 = -C_3$  and  $C_2 = -C_4$ . Equation 2.4 can then be written in the following form:

$$Y(x) = C_1(\sin \beta x - \sinh \beta x) + C_2(\cos \beta x - \cosh \beta x) \quad (2.8)$$

with the ratio of the coefficients for a mode of oscillation,  $n$ , of a cantilever (doubly clamped beam) derived from the third (second) derivative of  $Y(x)$  at  $x = l$  as

$$\frac{C_{2,n}}{C_{1,n}} = \frac{\cos \beta_n l \pm \cosh \beta_n l}{\sin \beta_n l \mp \sinh \beta_n l} \quad (2.9)$$

## 2.3 Frequency shift of a resonator due to the addition of a point mass

The expected frequency shift of an analyte mass landing on a resonant mechanical beam sensor can be derived from the resonant frequency of the beam along with its mode shape [21, 32, 33]. The mode shape is important as the underlying mechanism can be attributed to the amount of kinetic energy transferred from the vibrating beam to the analyte mass. This energy amount transferred, and hence resultant frequency shift, will depend on where the analyte lands on the beam. If an analyte mass is deposited on a portion of the beam with the greatest amount of deflection the highest amount of kinetic energy will be transferred to the analyte particle. This will cause the greatest amount of frequency shift.

The Raleigh-Ritz theorem can be used to quantify this effect [32, 34]. It states that the maximum kinetic energy of the vibrating beam will be equal to the maximum potential energy due to beam strain following from the conservation of energy. In this case it is assumed that the loaded mass does not affect the mode shape or create external strain on the beam.

$$E_{\text{strain}} = E_{\text{kin}} + E_{\text{kin},\Delta m} \quad (2.10)$$

The kinetic energy of an unloaded beam can be calculated using its mode shape and the simple expression of  $\frac{1}{2}mv^2$ . Taking the beam shape of mode  $n$  from equation 2.4 and normalizing it such that  $Y_n(x) = a_n\bar{Y}_n(x)$  with  $\bar{Y}(x)$  itself normalized so  $\int_0^l \bar{Y}^2(x)dx = l$  this becomes

$$\begin{aligned} E_{\text{kin}} &= \int_V \frac{1}{2}\rho[\omega_n a_n \bar{Y}_n(x)]^2 dV = \frac{1}{2}\rho w t \omega_n^2 a_n^2 \int_0^l \bar{Y}_n^2(x) dx \\ &= \frac{1}{2}m_{\text{beam}}\omega_n^2 a_n^2 \end{aligned} \quad (2.11)$$

where  $m_{\text{beam}}$  is the mass of the vibrating beam.

When an analyte is added to the beam with a mass of  $\Delta m$  the kinetic energy of the particle is dependent on both where it lands on the beam at  $x_{\Delta m}$  and what the new frequency of oscillation for the combined beam - particle system is, defined by  $\omega_{n,\Delta m}$ .

$$E_{\text{kin},\Delta m} = \frac{1}{2}\Delta m \omega_{n,\Delta m}^2 a_n^2 \bar{Y}_n^2(x_{\Delta m}) \quad (2.12)$$

Since it is assumed the loaded mass does not affect the mode shape the strain energy can be approximated as the kinetic energy of an unloaded beam. Equation 2.10 expands to

$$\frac{1}{2}m_{\text{beam}}\omega_n^2 a_n^2 = \frac{1}{2}m_{\text{beam}}\omega_{n,\Delta m}^2 a_n^2 + \frac{1}{2}\Delta m \omega_{n,\Delta m}^2 a_n^2 \bar{Y}_n^2(x_{\Delta m}) \quad (2.13)$$

which can then be reduced to find the new frequency of oscillation of a beam loaded with an analyte point mass:

$$\omega_{n,\Delta m}^2 = \frac{\omega_n^2}{1 + \frac{\Delta m}{m_{\text{beam}}}\bar{Y}_n^2(x_{\Delta m})} \quad (2.14)$$

## 2.4 Harmonic motion

### 2.4.1 Simple harmonic motion

Now that the mechanics of mass loading onto a mechanical beam are understood the limits of detecting this frequency change, and hence the smallest resolvable loaded mass, can be discussed. In this regard a much simpler model can be used and the mechanical beam can be represented by a simple harmonic oscillator spring-mass system.

The system is composed of a point mass of magnitude  $m$  attached to a massless spring with a spring constant of  $k$ . Using Hooke's law the force of the spring on the mass is represented by the following differential equation:

$$m \frac{\partial^2 x}{\partial t^2} = -kx \quad (2.15)$$

The solution to equation 2.15 describes the motion of a simple harmonic oscillator

$$x(t) = A \cos\left(\sqrt{k/m} t + \phi\right) = A \cos(\omega t + \phi) \quad (2.16)$$

where  $\omega = \sqrt{k/m}$  is the angular frequency of the mass' motion while  $\phi$  is its phase. The relationship between frequency, mass and spring constant is important when estimating the mass sensitivity of a nanomechanical beam.

### 2.4.2 Damped harmonic motion

In any real device, such as a nanomechanical beam, dissipation will be present in the system. The dissipation is a useful metric when characterizing the mechanical response of nanomechanical beams. Extended from the previous

section the dissipation is typically proportional to the velocity of the mass and can be represented by the damping constant  $b$

$$m \frac{\partial^2 x}{\partial t^2} = -kx - b \frac{\partial x}{\partial t} \quad (2.17)$$

The solution to this partial differential equation is a harmonic oscillator with exponential decay

$$x(t) = Ae^{-\frac{b}{2m}t} \cos(\omega_d t + \phi) \quad (2.18)$$

$$\omega_d = \sqrt{\omega^2 - \frac{b^2}{4m^2}} \quad (2.19)$$

When working with dissipation it is often more useful to talk about the quality factor,  $Q$ , of the device. The  $Q$ -factor is a measure of the energy stored over the energy lost per cycle. In the case of low damping, which is typical for a nanomechanical beam under vacuum, the  $Q$ -factor is defined by the following equation

$$Q = \frac{\sqrt{km}}{b} \quad (2.20)$$

A more thorough look at dissipation and deriving the  $Q$ -factor can be found in reference [35].  $Q$ -factors for nanomechanical beams in vacuum are typically greater than 1000, and with such values it is worth noting that equation 2.19 can be approximated by the frequency of an undamped oscillator.

## 2.5 Effective mass of a resonating beam

Section 2.3 looked at how the mode shape and particle loading location are taken into account when determining the frequency shift of a nanomechanical

gravimetric mass sensor. In order to simplify further analysis when investigating the ultimate sensitivity of these devices it is useful to model the resonating beam as a harmonic oscillator. To do this the effective mass,  $m_{\text{eff}}$ , of a resonating beam must be introduced. The effective mass is used to account for the reality that the beam is not a point mass. Not only is its mass distributed along its length but also the displacement of each portion of the beam while it oscillates varies along its length [36, 37]. The potential energy of the spring must be equal to the kinetic energy of the beam so this kinetic energy will vary along the beam length due to the varying levels of peak displacement. The effective mass takes into account the mode shape of the beam to treat the system as an effective point mass at the end of a massless spring.

To calculate the effective mass we can use Rayleigh's method and once again equate the maximum kinetic energy of the moving beam with the maximum potential energy of the beam spring such that  $KE_{\text{max}} = PE_{\text{max}}$ . At this point the spring constant of the beam is introduced as  $k_y$ . The maximum potential energy when the beam is at maximum deflection is:

$$PE_{\text{max}} = \int_0^{Y(l)_{\text{max}}} k_y y \, dy = \frac{1}{2} k_y Y(l)_{\text{max}}^2 \quad (2.21)$$

and the maximum kinetic energy of the entire beam along its length is:

$$\begin{aligned} KE_{\text{max}} &= \int_0^l \frac{1}{2} \rho w t v^2(x) dx = \int_0^l \frac{1}{2} \rho w t (\omega Y(x))^2 dx \\ &= \frac{1}{2} \rho w t \omega^2 \int_0^l Y^2(x) dx \end{aligned} \quad (2.22)$$

Equations 2.21 and 2.22 reduce to give the following expression for the beam resonant frequency

$$\omega = \sqrt{\frac{k_y Y^2(l)_{\max}}{\rho w t \int_0^l Y^2(x) dx}} \quad (2.23)$$

in which the effective mass can be extracted from the frequency of a simple harmonic oscillator,  $\omega = \sqrt{k_y/m_{\text{eff}}}$ :

$$m_{\text{eff}} = \rho w t \int_0^l \left( \frac{Y(x)}{Y(l)_{\max}} \right)^2 dx \quad (2.24)$$

This can be further simplified with the function  $\hat{Y}(x)$  which is the mode shape normalized in the  $x$ -direction by its length and the  $y$ -direction by its maximum deflection. This gives the effective mass as a function of the beam mass and an effective mass factor:

$$m_{\text{eff}} = m_{\text{beam}} \int_0^1 \hat{Y}^2(x) dx \quad (2.25)$$

The effective mass factors for the fundamental modes of a cantilever and a doubly clamped beam resonator are approximately 0.242 and 0.735, respectively.

## 2.6 Estimating the mass sensitivity of a nanomechanical beam resonator

The change in the effective mass of a beam due to mass loading will lead to a change in its resonant frequency as described in detail in section 2.3. In the following analysis it is still assumed that the analyte mass is much smaller than the beam mass and the addition of the analyte does not affect other beam properties such as the mode shape or spring constant of the beam [18]. Looking at equation 2.14 the frequency shift can be assumed to be linear when the analyte mass is much smaller than the beam mass such that

$$\Delta m = \frac{\partial m_{\text{eff}}}{\partial \omega} \delta \omega = \mathfrak{R}^{-1} \delta \omega \quad (2.26)$$

where  $\mathfrak{R}$  is the mass responsivity of the mechanical resonator and gives the amount of frequency shift caused by an addition of mass.

Looking back to the frequency-mass relation of a simple harmonic oscillator, and remembering that the spring constant remains unchanged, the mass responsivity can be estimated using the partial differential of the frequency with respect to the effective mass

$$\mathfrak{R} = \frac{\partial}{\partial m_{\text{eff}}} \sqrt{\frac{k_y}{m_{\text{eff}}}} = -\frac{1}{2} \sqrt{\frac{k_y}{m_{\text{eff}}}} \frac{1}{m_{\text{eff}}} = -\frac{\omega}{2m_{\text{eff}}} \quad (2.27)$$

Equation 2.26 then simplifies to the following:

$$\Delta m = -2 \frac{m_{\text{eff}}}{\omega} \delta \omega \quad (2.28)$$

To detect the smallest possible  $\Delta m$  two options stand out. First, the  $m_{\text{eff}}$  can be reduced and smaller nanomechanical resonators can be used, and second the frequency stability of the system can be increased to reduce the ratio of  $\delta \omega / \omega$ . The frequency stability can be measured experimentally using the Allan deviation [38] and methods such as implementing the nanomechanical resonator into a phase-locked loop can be used to increase the frequency stability, and ultimately the mass resolution, of the nanomechanical mass sensor. Analysis of noise sources limiting the mass resolution of nanomechanical mass sensors can be found in reference [18].

## 2.7 Conclusion

Nanomechanical beam resonators are well suited for detecting point masses due to their extremely small mass. The analysis for such systems is governed

by fairly straight forward equations. The largest limits to using these devices as mass sensors comes from the noise in the system which limits the ability to determine the frequency shifts used for detecting added mass. This has driven research toward better nanomechanical transduction methods with the goal of reducing noise in the system. Compared to traditional mass spectrometry systems a fundamental advantage is the ability to detect analyte particles of a neutral charge. This could make fragile materials much easier to study if they no longer need to have a charge added to them. This coupled with opportunities for both reducing costs and increasing portability make chip-based nanomechanical mass sensors an exciting technology for development.

---

---

## CHAPTER 3

---

# Nanophotonics

### 3.1 Introduction

The field of nanophotonics studies light interactions in the optical near-field. This is typically achieved using integrated photonics systems. Integrated photonics miniaturize conventional optical components onto an optical chip (analogous to integrating transistors onto a computer chip), and the field studies waveguide optics combined with other optical disciplines such as electro-optics, acousto-optics, non-linear optics and opto-electronics. A nanophotonic chip will include integrated optical waveguides guiding light along the chip to interact with various on-chip optical devices [39]. In the context of this thesis nanophotonics will specifically refer to the interaction of these waveguides' evanescent fields with either integrated optical and/or nanomechanical structures.

Many different types of nanophotonic devices are required to utilize the system in detecting nanomechanical resonator motion. Light must first be coupled into and out of the optical chip, it must then be transported along the chip, and finally integrated optical structures are required to interact directly with the nanomechanical structures. The photonics industry initially developed these

structures for optical integrated circuits [40], but they have been very useful in studying nanomechanics as well [8].

Nano-optomechanical system (NOMS) devices have used many of the standardized materials and processes developed for the integrated photonics industry. Silicon-on-insulator substrates with dimensions consisting of a 220 nm thick silicon device layer and a 2  $\mu\text{m}$  buried oxide layer are commonly used to pair with the free-space wavelength range of 1530 nm to 1565 nm belonging to the infrared optical telecommunications C-band. The 220 nm is chosen to match half the laser wavelength in the medium. 500 nm wide silicon strip waveguides (described in section 3.3) are also typically used as it provides a good compromise between low loss light propagation and evanescent tail size. The evanescent tail is required for the waveguide to interact with other on-chip structures such as photonic or nanomechanical devices [40, 41].

## 3.2 Light coupling from an optical fiber to an optical chip

Several methods exist for coupling light from an external source onto a nanophotonic chip. Typically the external source is in the form of a single mode optical fiber and it is coupled into an integrated optical waveguide. Methods have been developed to either couple light to an entire chip or to just couple light to an individual nanophotonic structure.

One of the simplest ways to couple light onto a chip is end-fire coupling. It simply aligns the end of a single mode optical fiber to the butt end of an optical waveguide at the utmost edge of the photonic chip. Care must be taken to size-match the optical mode between the fiber and the waveguide, otherwise back reflections will occur and the coupling will experience higher losses [42, 43]. This optical mode matching is accomplished using tapers on the waveguide to adiabatically shift between the optical mode sizes of the fiber and the waveguide. Although this method is both simple to design and implement

it can only occur along the edges of the optical chip and can therefore limit on-chip optical device locations and densities.

To address the optical device placement issues of end-fire coupling, light coupling using optical gratings has been developed [44, 45, 46, 47, 48, 49]. Using diffraction, light is channeled at a nearly  $90^\circ$  angle from free space into the waveguide, and as a result it removes the need for alignment to occur at the chip edge. This is important for large scale device integration as the density of addressable coupling locations is no longer dependent on the chip's perimeter length. The optical gratings are created using a series of alternating high and low index of refraction regions. The periodic index change is usually fabricated by etching trenches in the silicon to create regions of high index silicon next to low index air [44, 45, 46]. This is a popular method of coupling as it can couple to a device anywhere on the chip, and it does this with both a high efficiency and a large operational bandwidth.

Similarly to end-fire coupling, coupling using optical gratings must also use an adiabatic taper to match the optical mode of the fiber with the standard 500 nm wide waveguide. This will hurt the maximum device density on the chip as a large region will be required to form the taper from a typically 10  $\mu\text{m}$  wide grating coupler to a 500 nm waveguide. To eliminate this taper, focused grating couplers can be used which decrease the device footprint and therefore increase device density across the entire chip [50]. To address the devices at arbitrary chip locations multi-axis fiber positioners are often used. They allow the input light to be aligned to the grating in both position and angle to maximize coupling efficiency [46]. Grating couplers are one of the more commonly used methods to couple light onto a chip due its effectiveness at addressing high density optical structures.

It is much easier to detect nanomechanical motion when the device is operating under vacuum. This eliminates air damping on the beam and the signals are consequently much stronger. Light coupling, however, becomes more difficult when introducing the sample into vacuum. One option is to place all the alignment positioning systems in vacuum along with the sample. This creates

a more complicated experimental setup as a larger vacuum chamber will be required along with vacuum compatible positioning systems (both positional and angular). A second option is to fix the alignment prior to pump down which removes the need for vacuum safe positioners but at the expense of a loss of flexibility to tune the alignment for maximum coupling efficiency after pump down [37]. A third option has been developed which allows the grating coupler alignment to take place outside of vacuum. A confocal scanning coupler setup gives the flexibility of alignment in vacuum with minimal experimental setup complications. Using a free space laser setup the input angle and incident location of the light on the photonic chip is adjusted and focused through a vacuum chamber window. This is the method of light coupling used in this work and it is described in more detail in chapter 4.

### 3.3 On-chip light propagation

Once coupled onto the chip light must then be directed towards the various integrated optical structures. This is accomplished using integrated optical waveguides. As the most basic integrated optics component it controls the direction of propagation of light along the chip. Different types of on-chip waveguides exist, but the focus will be on dielectric waveguides which are most relevant to this work.

Dielectric waveguides rely on total internal reflection to confine and guide light. Two basic types include planar waveguides which confine light in one dimension, and channel waveguides which confine light in two dimensions [39, 51]. Planar, or slab, waveguides are formed when a slab of higher refractive index known as the core is sandwiched between lower index claddings both above and below it. A symmetric slab waveguide has upper and lower claddings of the same refractive index, whereas an asymmetric waveguide has claddings of different indices (both of which are lower than the core). Light travels within the core and is reflected at each interface due to total internal reflection. This total internal reflection follows from the boundary equations of Maxwell's equations

and cause the requirement of a higher index core. The solutions to these equations will create independent solutions based on the light's polarization so it is important to know whether the light has a transverse electric (TE) or transverse magnetic (TM) polarization. Full analysis of light propagation in a slab waveguide can be found in general photonics textbooks such as references [39, 51, 52, 53].

With nanophotonic circuits two dimension confinement using a channel waveguide is much more useful. It allows light to be directed toward various integrated photonic structures at arbitrary locations on the chip. Similarly to a slab waveguide, an upper and lower cladding confine light perpendicular to the sample surface. To confine light in the plane of the photonic chip there is also an index change parallel to the chip surface. The parallel confinement allows the light to be guided to separate structures on the sample surface.

To form a channel waveguide the index change along the chip surface can be achieved in several different ways. Schematics of various channel waveguide types [51] can be seen in figure 3.1. A common method, and the method used to create channel waveguides in this thesis, is to use an SOI substrate to create a strip waveguide with the device silicon layer as the core, the silicon dioxide BOx layer as the lower cladding, and air/vacuum as the upper and side claddings. These devices are easy to fabricate and only require a single etching step. The use of the SOI substrate also facilitates easy integration with nanomechanical structures which can be easily fabricated with SOI substrates themselves.

The size of the core of a channel waveguide is generally on the same order as the wavelength of the light in the propagation material. As a result, the angle in which total internal reflection can occur and light can propagate along the core becomes discretized. These discretized angles define the propagation modes of the waveguide. They are dependent on the light polarization and in photonic channel waveguides TE-like mode propagation is defined as the electric field parallel to the substrate surface while TM-like mode propagation has the magnetic field parallel to the substrate surface. The number of supported

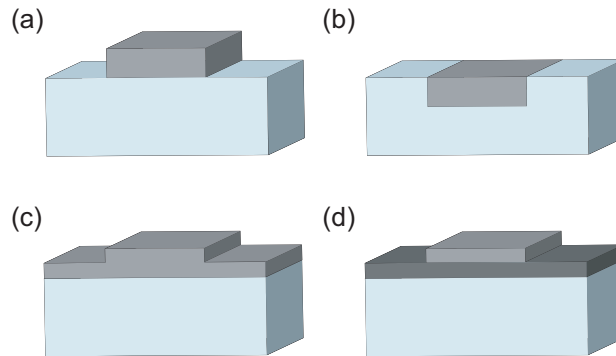


Figure 3.1: Various types of channel waveguides. (a) strip waveguide (b) embedded strip waveguide (c) rib waveguide (d) loaded rib waveguide. The darker the shading indicates a higher refractive index.

modes depend on the waveguide dimensions along with the index contrast between the cladding and core. Single mode waveguides are generally preferred since multi mode waveguides see the power distributed among all the different modes. The modes will travel with different reflection angles, and therefore different speeds along the waveguide, and mode dispersion will occur. Mode dispersion will cause signal distortion as the different modes will arrive at the measurement points with different phases.

Cut-off occurs when a traveling mode is no longer supported in the waveguide's dimensions and materials. In a symmetric waveguide no cut-off exists for the lowest order mode, but this is not the case for an asymmetric waveguide. To avoid reaching the cut-off condition for all modes in a typical silicon strip waveguide, standardized SOI wafers are used in the integrated photonics industry. This makes it very difficult to create waveguides with a core region too small to carry a propagating mode [39, 52]. This makes silicon channel waveguides using SOI substrates a robust device for both design and fabrication and an excellent option for integrating with nanomechanical systems.

## 3.4 Integrated optical devices for nanomechanical beam interaction

The final type of structure NOMS devices utilize are optical devices which interact with nanomechanical beams to transduce the beam motion. The devices can either be waveguide based such as directional couplers or Mach-Zehnder interferometers (MZI), or they can take advantage of an optical cavity such as an optical disk or ring resonator or else a photonic crystal cavity. The optical device can function directly as the nanomechanical resonator itself (such as a freely oscillating waveguide) or it can be placed in close proximity to the nanomechanical resonator so the resonator can interact with its evanescent fields. Both types of systems rely on a form of mechanical motion modulating the optical properties of a photonic device.

### 3.4.1 Effective index of refraction

The essential principle for most types of nanophotonic detection relies on the manipulation of the optical path length of a waveguide due to the motion of a nanomechanical beam. This usually occurs with a changing air gap between the waveguide and an adjacent structure which causes a change in the effective refractive index of the propagating mode of light. A simplistic way to envision the effective index effect is to first imagine the mode propagating along the waveguide. If the traveling mode's field penetrates deep into the cladding it will see more of the cladding's refractive index and will tend toward that value. If, however, the mode is confined only to the core then the mode will mostly see the core refractive index. In general for guided modes, the modal effective index will be between the refractive index values of the core and the cladding depending on the amount of field present in each medium. As an example, a nanomechanical beam oscillating in and out of a waveguide's evanescent tail will increase and decrease the effective index of the mode, respectively.

The rate of change of the effective index due to the changing gap spacing is important in quantitative NOMS analysis. Given accurate device dimensions, finite element [54, 55] or finite difference [56, 57, 58, 59, 60] methods may be used to numerically solve these values. It is also possible, however, to approximate the solutions for the effective index analytically using the effective index method.

The effective index method approximates waveguide propagation modes by reducing two dimensional waveguide analyses to a series of slab waveguide calculations [39, 53, 61]. Despite its simplicity, the effective index method is fairly accurate for low-order modes which are far from the optical cut-off frequency of the waveguide.

The method first involves taking the cross section of the waveguide and breaking it into a series of slab waveguide sections. The sections are treated independently and the index is solved for each slab section for either the transverse electric-like (TE) or transverse magnetic-like (TM) mode. The method for solving for the propagation constants in a slab waveguide can be found in general photonics textbooks [39, 53]. The solved sections are then combined to form a new slab waveguide in the perpendicular direction. The index calculated for each section forms the layer index for each layer of the new slab waveguide, as seen in figure 3.2. This is solved as before but for the opposite mode polarity. This gives the effective index for the calculated mode of the waveguide.

In the concept example shown in figure 3.2, a silicon waveguide is suspended over a silicon dioxide substrate with a gap,  $g$ . The device is then split into three vertical sections where sections I and III can be taken as air, and section II is the slab waveguide of air/Si/air-gap/ $SiO_2$ . If solving for the TE-like mode for the waveguide, the TE mode solution for the slab is calculated and the index is taken as  $n_{II}$ . The index of air can be used for both  $n_I$  and  $n_{III}$ . The TM mode solution is then found for the horizontal slab waveguide composed of sections I, II and III as in figure 3.2 (b), and this gives the TE-like mode effective index of the waveguide. If the waveguide is in motion as a mechanical beam, the air

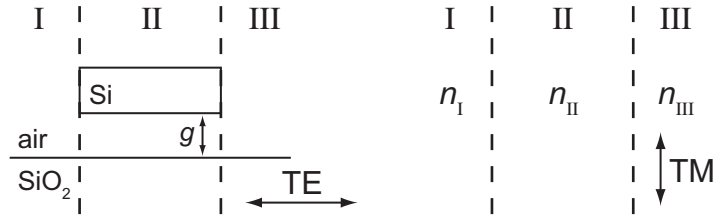


Figure 3.2: A schematic for solving the TE-like mode index using the effective index method for a suspended Si waveguide. (a) The suspended Si waveguide with an air gap,  $g$ , is first separated into three sections: I, II and III. The slab waveguide mode indexes are calculated individually for each of these sections. (b) The mode indexes found in (a) are used to create a new slab waveguide. The index of this slab, and hence the waveguide, is calculated for the opposite polarity mode of part (a).

gap,  $g$ , will change. To find the rate of change of the effective index due to the moving waveguide this process is repeated for different  $g$  values.

### 3.4.2 Waveguide based transduction schemes

Directional couplers were one of the first ways to detect nanomechanical beam motion using optical waveguides [62]. To understand the transduction mechanism it is first important to understand how a standard directional coupler works. A directional coupler consists of two parallel waveguides spaced sufficiently close together so they are within the range of the other guided mode's evanescent tail. This enables power to transfer between the waveguides as photons can tunnel between them. To better understand the coupling of power from one waveguide to the other, one can also look at coupled mode theory. The coupling can be regarded as a scattering effect of the waveguide's mode by the adjacent waveguide. The scattering can be interpreted as a second source present in the adjacent waveguide, so therefore the amplitude will change in the second waveguide [51]. This occurs from the perspective of each individual waveguide so light is periodically transferred between them. The amount of light transferred between two given waveguides will depend on the coupling

length (the length in which the waveguides are parallel to each other) and the spacing between them [63]. De Vlaminck et al. detected nanomechanical beam motion by making one of the parallel waveguides a freely oscillating nanomechanical beam [62]. With a constant coupling length the spacing between the waveguides modulates with the nanomechanical beam motion, therefore modulating the power transferred between the two waveguides. Detecting the power modulation transduces the nanomechanical beam/waveguide's motion.

A slot waveguide can also be produced between two adjacent waveguides. In a slot waveguide the optical power travels in the gap between the two waveguides and not in the high index region [64]. This will occur when the slot width is narrower than the field decay length within the slot. In the region the field will remain high and proceed to travel along it. Suspending the high index regions surrounding the slot will create two parallel nanomechanical beams. The oscillating beams will modulate the gap between them, and this changing gap will modulate the optical property of traveling mode's index of refraction. This modulating index change has been detected in an optical ring resonator [65] to transduce nanomechanical beam motion.

Finally, a waveguide device such as a Mach-Zehnder interferometer (MZI) can be used to detect nanomechanical motion. A phase shift is created in one of the interferometer arms due to an index change caused by nanomechanical beam motion. The spacing between the waveguide and an adjacent object is modulated with the nanomechanical beam motion. This causes the index of the arm next to the nanomechanical resonator to modulate and therefore the overall optical path length of the arm also modulates. The power output due to the path interference in turn modulates with very good nanomechanical transduction sensitivity [5, 66, 67]. This method is discussed in detail in chapter 5.

### 3.4.3 Optical cavity based transduction schemes

Nanomechanical transduction benefits greatly with the use of optical cavities. In the case of an optical disk or ring resonator, light tunnels into an optical cavity and becomes trapped inside oscillating within the structure with low losses. The wavelength of light that can enter the cavity is determined by the physical cavity characteristics such as its size and index of refraction [68, 69, 70]. The optical frequency of the cavity can be changed with nanomechanical interaction and monitoring the change can transduce the nanomechanical motion. The nanomechanical device can be either physically integrated into the cavity or it can be adjacent to it as long as it interacts with the cavity's evanescent fields. The detection has exhibited very high accuracy [6, 65, 71, 72]. Chapter 6 of this thesis thoroughly analyzes nanomechanical interaction with a racetrack resonator optical cavity.

Photonic crystal optical cavity structures are also being used with great success in nanomechanical transduction. The general principle is similar to ring cavities with a nanomechanical device modulating the optical mode of the cavity [8, 73]. The advantage of using photonic crystal cavities is that stronger field gradients can be confined in smaller modal volumes compared with total internal reflection based cavities such as disk or ring resonators [74].

The reason photonic crystals can achieve smaller mode volumes is because there is little dependence on the  $k$ -vector of the light trapped within the cavity. This differs from the total internal reflection mechanism of a channel waveguide where the light must reach a critical angle to avoid the cut-off region. The independence on the  $k$ -vector results from the dependence on Bragg reflection to trap light within the cavity [75]. A photonic band gap can be created in the photonic crystal by engineering a defect, and this band gap will allow light to enter the crystal at a specific frequency based on the crystal characteristics. These cavities are very sensitive to perturbations caused by nanomechanical motion and are becoming very popular for investigating nanomechanical systems [73, 76, 77].

### 3.5 Integrated optical actuation

Light can generate two types of optical forces on external objects: scattering forces and gradient optical forces. Scattering forces are caused by momentum transfer from the radiating light and act along the  $k$ -vector of the light. For integrated nano-optomechanical systems this type of optical force is not as important since the mechanical devices in the system are generally parallel to the light  $k$ -vector, as directed by the waveguide, and not perpendicular where the scattering force would be directed. Gradient optical forces, however, act in the direction of the strongest optical field. This force would then pull objects toward an integrated optical waveguide which has significant evanescent fields radiating from it [78]. In device descriptions discussed above it would mean one of two things. The free standing waveguide would pull itself toward the adjacent stationary surface in the case where the nanomechanical beam and optical waveguide are the same object, or otherwise the stationary waveguide would pull the adjacent nanomechanical beam toward it.

The optical gradient force can be explained when considering a polarizable microscopic particle. If this particle is placed in a laterally varying optical field a dipole will be induced. Once induced, this dipole will experience a force toward the region of the strongest field. A macroscopic object can be regarded as a composition of these microscopic dipolar microparticles and the same principles hold [79]. In the case of the nanophotonic waveguide the strongest field gradient is at the center of the waveguide, and the attractive force is centered here.

For physical insight into this optical force, it can be derived from the change in the eigenmode optical frequency,  $\omega_{\text{opt}}$ , between two parallel slab waveguides separated by a gap spacing of  $g$ . The work done displacing the beams a distance  $\Delta g$  will be equal to the total change in energy due to the shifting optical mode [80] so that the force can be derived as

$$F = - \frac{1}{\omega_{\text{opt}}} \left. \frac{d\omega_{\text{opt}}}{dg} \right|_k U = - \frac{1}{\omega_{\text{opt}}} g_{\text{om}} U \quad (3.1)$$

where the negative sign is indicative of an attractive force,  $U$  is the total system energy,  $k$  is the wave vector and  $g_{\text{om}}$  is the optomechanical coupling constant.

The optomechanical coupling constant can be understood by looking at the coupling between the optical modes of the separate waveguides, such as is described with directional couplers in subsection 3.4.2. A combined coupled eigenmode will be formed which will change based on the gap spacing between them. If a symmetric mode is formed the mode index will increase which leads to a lower frequency and hence a lower energy. This leads to an attractive force. With the same argument a repulsive force is created in the presence of an antisymmetric mode. The optomechanical coupling constant will be dependent on the separation, the refractive index and the waveguide dimensions (which also determine the coupling between the modes).

This optical gradient force was first demonstrated with a suspended nanomechanical waveguide [5]. In this case the coupling was not between two beams, but the waveguide and the silicon dioxide substrate it was suspended above. In this case the decreasing gap spacing increases the effective index of the mode thus only attractive forces are demonstrated. To drive a nanomechanical beam this attractive optical gradient force is modulated on the beam at the beam's mechanical frequency. This is achieved by varying the amplitude of a pumping laser as this changing laser energy will then modulate the force as in equation 3.1. The pump laser is independent of the probing laser and is filtered out of the system before detection at the photodiode.

## 3.6 Conclusion

Nanophotonics has proven to be an excellent technology for studying nanomechanical motion. Compatible materials allow for easy integration between

the two fields, and the maturity of the technology creates a low barrier of entry. Compared to existing technologies it retains the measurement bandwidth and displacement sensitivity of traditional optical mechanics, but it also takes advantage of the optical near-field mechanisms of nanophotonics to avoid common size restrictions due to diffraction effects. The large operational bandwidth for both detecting and driving nanomechanical devices also offer advantages over nanoelectromechanical systems which are limited at higher frequencies due to the RLC roll-off effects. With the advances in on-chip light sources and detectors, and the sensitivity of nanomechanical transduction using nanophotonics, it is a promising technology for developing portable nanomechanical sensing systems.

---

---

## CHAPTER 4

---

### Experimental Setup

Nanomechanical beam motion is most often studied while operating under vacuum. This removes air damping on the beam and increases the amplitude of oscillation making the beam signals easier to detect. With nano-optomechanical system devices light must be coupled onto the photonic chip and this can cause complications if the chip is placed inside a vacuum chamber. To eliminate the complications of using positioning systems inside a vacuum chamber or fixing the alignment of the optical source to the photonic chip prior to chamber pump down, a free-space confocal laser scanning system can be used [81]. This type of system allows flexibility in aligning light into and out of the photonic chip while the chip is under vacuum, and was used to detect the nano-optomechanical system devices in this work.

#### **4.1 Confocal laser scanning system for nanophotonic chip coupling**

A free-space confocal laser scanner system allows the positioning and alignment components of a nanophotonic grating coupler system to be placed outside of vacuum while only the nanophotonic chip is placed inside the vacuum chamber

[81]. This makes the system similar in complexity to a standard free-space interferometric setup [82, 3, 83]. The differences arise in the confocal system having the ability to freely adjust both the position and input angle (k-vector) of the input laser onto the entrance pupil of the focusing microscope objective.

A set of Fourier transform planes exist between the objective's entrance pupil and its focal plane. Changing the position on the entrance pupil will adjust the k-vector at the focus plane, and changing the k-vector on the pupil will adjust the position at the focus plane. This is shown in figure 4.1 (a). This results in the k-vector and position of the input light onto the nanophotonic chip's grating couplers to be controlled independently allowing for maximum coupling efficiency to be easily attained.

The microscope objective captures light from the output grating coupler back into the free-space confocal system. Typically nanophotonic light sources (about 1500 nm to 1630 nm) output their light to a fiber optic cable so a fiber collimator is used to transfer light from the fiber system to the free space system and vice versa. The system schematic is shown in figure 4.1 (b). The system is illuminated using a halogen light source which is input from the backside of the system. A CCD camera which operates in near-infrared spectrum is used to view the illuminated area on the sample. Since the sensor does not detect light at the visible wavelength a phosphor coating is used on the lens. The phosphor fluoresces upon interaction with visible light to be detected by the CCD camera.

This type of probe system relies on non-optical methods for nanomechanical beam actuation. Typically this includes mounting the optical sample to a piezo-electric disk to shake the entire sample to provide the driving energy. The device is typically both driven and detected using the same piece of equipment such as a lock-in amplifier or network analyzer. Thermomechanical noise signals can also be detected if no driving signal is applied to the nanomechanical device. In this case the TM noise signal can be measured with either a lock-in amplifier or a spectrum analyzer.

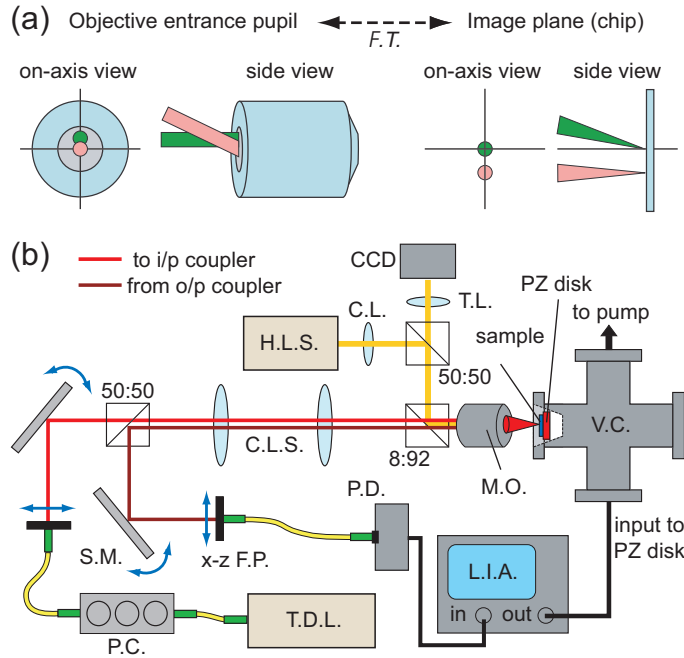


Figure 4.1: (a) Fourier transform planes in a microscope objective. (b) Schematic showing the confocal laser scanner-based NOMS measurement setup. C.L.: collector lens, C.L.S.: confocal lens system, H.L.S.: halogen light source, L.I.A.: lock-in amplifier, M.O.: microscope objective, P.C.: polarization controller, P.D.: photodetector, S.M.: steering mirror, T.D.L.: tunable diode laser, T.L.: tube lens, V.C.: vacuum chamber, and xz F.P.: xz fiber positioner. From reference [81]. Copyright 2013 The Japan Society of Applied Physics.

## 4.2 Pump probe optical setup

To fully take advantage of the frequency bandwidth advantages that a nanophotonic system offers over traditional nanoelectronic systems, the device must not only be detected using optical methods but driven as well. Nanophotonic systems offer a simple way to achieve this through the use of optical gradient forces caused by the waveguides' evanescent fields. The strength of these gradient forces is modulated using a time-varying optical power on a separate pump laser which is added to the system [5]. The schematic with the added

pumping laser is shown in figure 4.2.

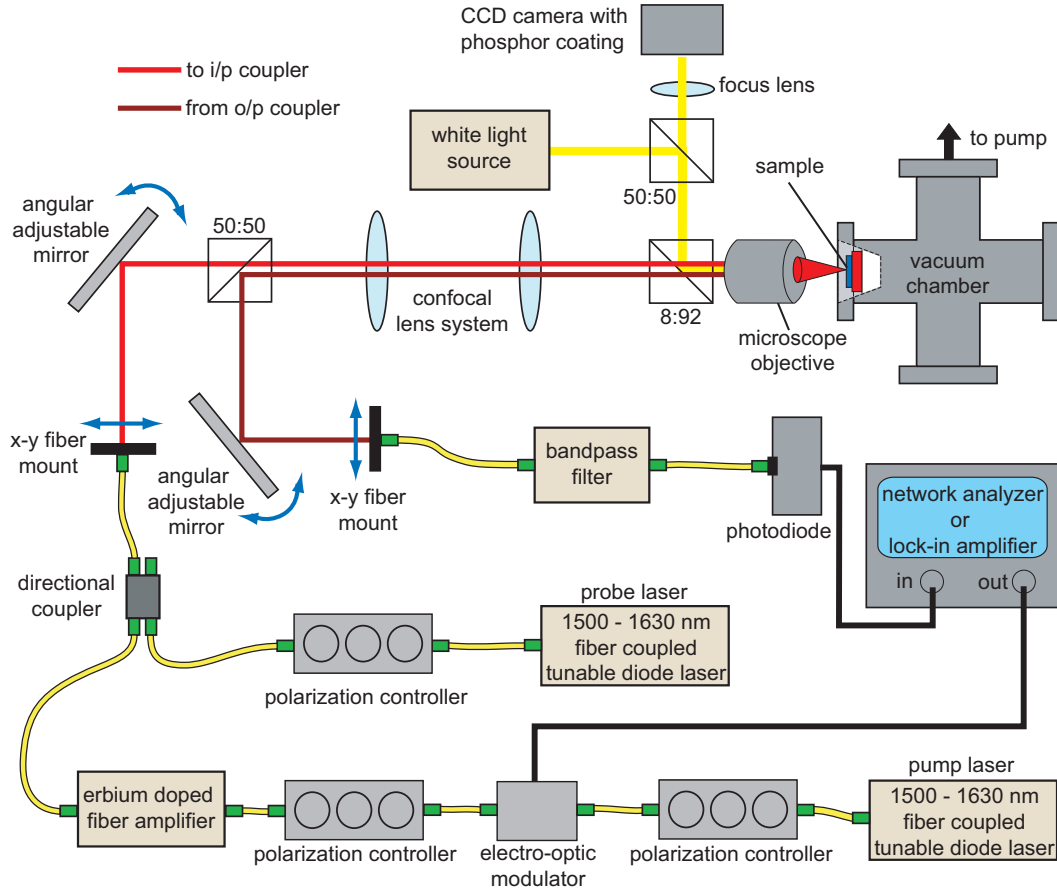


Figure 4.2: Schematic of the optical pumping and probing measurement system. Two tunable diode sources are used: one for driving the nanomechanical device and one for detecting it. The two lasers are co-aligned using a directional coupler and the incident location and angle of the input light is controlled using a free space confocal setup.

The pump and probe lasers used in the system are both tunable diode lasers in the telecommunications wavelength range of about 1500 nm to 1630 nm. The tunability allows for more design flexibility since both the pump and probe lasers can be individually tuned for maximum effect for each individual device. The pump laser is added to the same laser path as the probe laser using a directional coupler so no additional alignment is required. The pump

laser is filtered out of the system prior to detection at the photodiode. If it is not filtered the mechanical signal would be swamped by signal noise caused by the pumping laser since the pump laser carries an optical signal at the same frequency as the mechanical beam, but with a much higher amplitude.

To create modulation on the output power of the pumping laser it is passed through an electro-optic modulator (EOM). An AC signal is applied to the EOM which uses interference within it to modulate the output power at the AC signal frequency. The time varying signal is then passed through an erbium doped fiber amplifier (EDFA) to increase the optical power in the system and hence the optical forces on the nanomechanical beam. The EOM, EDFA and input grating couplers are all polarization dependent so polarization controllers are used to maximize throughput of these devices. As with the piezo driven devices a network analyzer or lock-in amplifier is used to both drive and detect the NOMS structures. A signal is swept across the mechanical frequency range of the device while it is simultaneously detected. The nanophotonic measurement system offers very good flexibility when working with nanomechanical samples. The flexibility of aligning to the devices while in vacuum allows for an easy way to maximize the signals from the nanomechanical beams.

---

---

## CHAPTER 5

---

# Mach-Zehnder interferometer detection of a side coupled cantilever

### 5.1 Introduction

Many early nano-optomechanical system devices required that the nanomechanical component function also as a nanophotonic waveguide. In these systems material beneath the waveguide was etched away to create a freestanding nanomechanical doubly clamped beam [62, 5, 84, 85]. This method is very easy to implement but there are some drawbacks to it. The first is the inherent size limitation on the nanomechanical device. As the device is generally created from a strip waveguide, which has asymmetric cladding, the waveguide must be large enough to avoid cut-off and hence support a traveling optical mode. This places a lower limit on the nanomechanical beam size if the beam must function as a waveguide itself.

Since a released nanomechanical beam/waveguide becomes a symmetric waveguide (with air cladding on all sides) it theoretically has no size limitations to meet mode cut-off conditions (see chapter 3). The design of such devices would, however, require a carefully designed transfer of the mode to and from the propagating asymmetric waveguide. Fabrication would no longer be as

simple as undercutting the waveguide. Another issue with this type of device is that optical mode propagation losses will increase as the waveguides become smaller. This is caused by scattering due to the waveguide's sidewall roughness. This occurs in greater amounts as the optical mode energy present in the evanescent tail increases with decreasing waveguide size. Energy in the evanescent field is more greatly affected by the roughness and sidewall scattering [86]. Fortunately nanomechanical beam size limitations are fairly simple to circumvent.

An effective option for removing the size limitation is to separate the mechanical and photonic elements in a NOMS device. Instead of a mechanical beam/waveguide interacting with a stationary object adjacent to it, such as the substrate, an external nanomechanical beam can interact with a standard stationary waveguide. The waveguide and external nanomechanical beam must be in close proximity to each other so the mechanical beam motion interacts with the optical mode's evanescent field. The mechanical element can interact with a regular strip waveguide [66, 67] or with an optical cavity structure for higher sensitivities [6, 71, 87].

This chapter will look more closely at NOMS devices with the nanomechanical element fabricated externally to a nanophotonic waveguide. Specifically, the motion of cantilever devices oscillating in plane of the substrate are detected using a nanophotonic Mach-Zehnder interferometer system. The detection of cantilever devices without mode carrying size limitations demonstrate that nanophotonic detection can effectively transduce these types of nanomechanical structures. This gives more options for pursuing the goal toward effective nanomechanical mass sensors with sub-proton sensitivity. This chapter is based on the work in reference [67].

## 5.2 Device design and fabrication

A Mach-Zehnder interferometer (MZI) is used to detect nanomechanical beam motion. An MZI is a nanophotonic device where light is split equally among

two optical paths: the detection arm and the reference arm. The detection arm experiences a change to its optical path length while the reference arm's optical path length remains constant. The two paths then recombine and the interference between them determines the optical power at the output. At a phase difference of  $180^\circ$ , determined by the optical path length difference between the two arms, the output will be zero due to complete destructive interference. For maximum sensitivity the MZI arms should be  $90^\circ$  out of phase. This will give the greatest amount of power output change for the smallest change in phase between the two paths.

In the experiment a cantilever is patterned externally to and in close proximity with the MZI detection arm. As the cantilever oscillates toward the waveguide it locally increases the effective index of refraction. This increases the optical path length of the reference arm and changes the interference output when the paths recombine. The mechanically oscillating cantilever will therefore cause a modulating power output of the MZI. This is detected to transduce the beam motion.

The devices were fabricated on a 220 nm silicon device layer, 2  $\mu\text{m}$  BOx SOI wafer. CMC Microsystems facilitated the design run using 193 nm line stepper lithography through a standardized integrated photonics run at the IMEC foundry. The waveguides were patterned 550 nm wide while the cantilever devices were patterned approximately 200 nm wide with lengths from 2  $\mu\text{m}$  to 5  $\mu\text{m}$ . The spacing between the cantilever and the MZI arm was about 140 nm as measured by SEM. A simple y-splitter was used in the MZI device with an arm path length difference of 58.31  $\mu\text{m}$ . An SEM of an MZI and cantilever is shown in figure 5.1.

To release the nanomechanical cantilevers the sample undergoes a mask-less timed buffered oxide etch (BOE). This is possible by designing the cantilevers to be much narrower than the nanophotonic waveguides. The BOx layer can be completely etched beneath the cantilevers while still anchoring and supporting the waveguides with no extra fabrication steps. A critical point dry is completed on the sample after the etch to prevent cantilever stiction. A cross

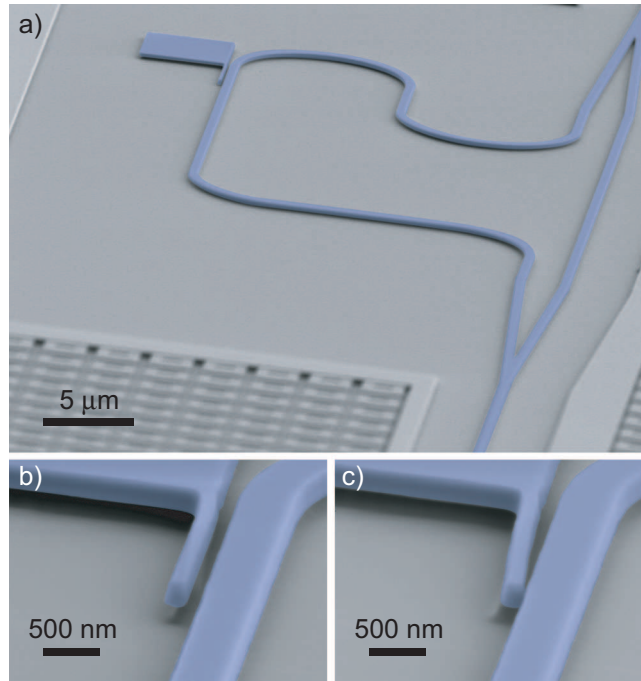


Figure 5.1: (a) Colorized SEM of Mach-Zehnder interferometer nanomechanical cantilever detection device taken at  $75^\circ$  tilt. (b) Colorized SEM of a cantilever adjacent to the MZI taken at  $75^\circ$  tilt. (c) SEM of similar cantilever to (b) but drawn toward the MZI arm due to electrostatic forces caused by the SEM charging. The optical path length of the MZI arm will change adjacent to the cantilever. Adapted from [67].

sectional view of this mask-less etch is shown in the schematic in figure 5.2 (a).

To ensure that the cantilever devices do not carry traveling optical modes the devices were simulated with a 3D model using Lumerical FDTD software. The fundamental mode of the cross section of the waveguide adjacent to the cantilever is calculated. Although the presence of the cantilever slightly breaks the symmetry of the traveling mode and pulls the energy slightly into the gap region no energy is guided in the cantilever core. This is important to verify the device does not have a minimum size. The simulation also provides information on the effective index of the propagating mode and how the effective index will

change based on the changing gap between the cantilever and the waveguide. The simulated mode is shown in figure 5.2.

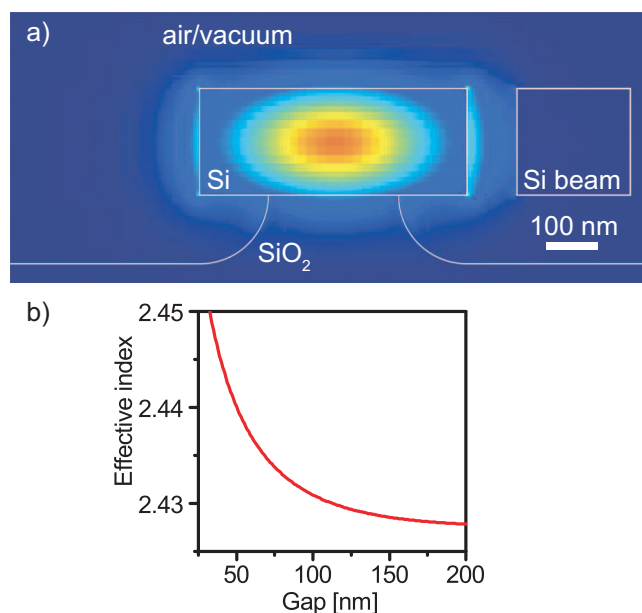


Figure 5.2: (a) The simulated optical mode of the waveguide adjacent to a resonator released using a mask-less BOE step. The optical mode does not travel in the silicon beam, and the etch step only partially etches underneath the silicon waveguide. (b) The simulated effective index of the mode versus the gap spacing between the waveguide and the cantilever.

The motion of the cantilever is transduced through the modulating optical path length caused by the cantilever's oscillations. For the strongest change in the optical path length the cantilever oscillates in the wafer plane toward and away from the waveguide. To actuate the device it is mounted on a shear mode piezoelectric crystal using double sided tape. The cantilevers are oriented perpendicular to the piezo's direction of motion and the entire sample is shaken as a frequency swept signal is applied. The power modulation caused after the MZI arms recombine and interfere (with a modulating optical path length on the detection arm) is detected using a New Focus 1811 IR DC-125 MHz photoreceiver and an HP 8752C network analyzer. The network analyzer

is also used to drive the piezo disk.

### 5.3 MZI device detection

To detect the device light is first coupled into the system using a confocal free space nanophotonic setup similar to that in figure 4.1. The detection laser is a Santec TSL-510 fiber coupled tunable diode laser, and grating couplers are used to couple the laser light into the device. To eliminate air damping the sample is placed in a vacuum chamber with pressure lower than  $1 \times 10^{-5}$  Torr [81].

To find the  $90^\circ$  MZI arm phase difference and maximum transduction point the diode laser wavelength is scanned and the DC optical power measured. A sample scan is show in figure 5.3 for an MZI device before and after the mask-less BOE. The maximum transduction will occur when the probe laser is at the point of greatest slope. This is due to the fringes shifting to the left and right as the cantilever changes the optical path length of the reference arm. This shift will be detected with the greatest power change as the probe laser is sitting at the constant wavelength with the greatest slope. The large fringes correspond to constructive and destructive interference of the two MZI paths. The overall envelope is caused by the limited bandwidth of the grating couplers while the small fringes on the signal are caused by the weak Fabry-Perot cavity created between the input and output grating couplers. The extinction ratio for the MZI device is greater than 20 dB.

The mask-less BOE etch does not have a significant affect on the operation of the MZI device. This is apparent as the slope of the DC optical wavelength scan remains approximately equal before and after the etch. The effective refractive index can also be extracted from the scan and changes from 2.49 to 2.42 at 1550nm due to the etch. This agrees with FDTD simulations. The decrease in refractive index corresponds to the optical mode interacting more with air than with  $\text{SiO}_2$ . The coupler envelope also shifts, but no data can be

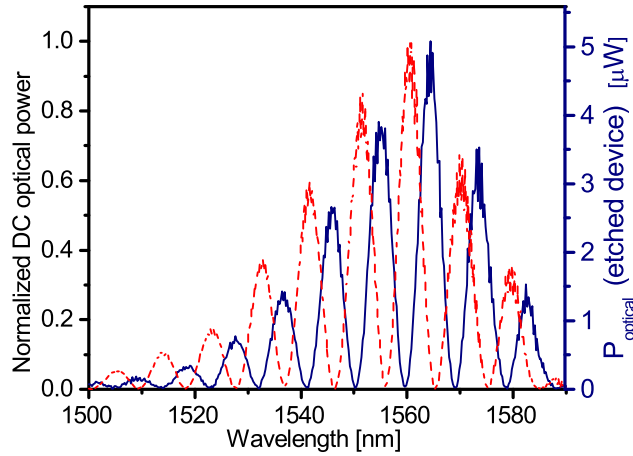


Figure 5.3: DC optical wavelength scan of an unetched (dashed) and mask-less buffered oxide etched (solid) MZI structure. Adapted from [67].

derived from this as the envelope is dependent partially on the angle of incident light into the coupler which is not measured in the experimental setup.

The NOMS MZI readout mechanism is tested by looking at the mechanical resonance frequencies and mechanical quality factors of different cantilevers. The optical probe power at each cantilever is set to about  $70 \mu\text{W}$ . A typical frequency response is shown in figure 5.4 with a 300 Hz measurement bandwidth and 16 times averaging. The device measured is  $4.5 \mu\text{m}$  long and  $234 \text{ nm}$  thick in the oscillating direction as measured by SEM. The device is  $220 \text{ nm}$  wide and this is defined by the device layer thickness of the integrated photonic SOI wafer. Devices with mechanical frequencies from 10 MHz to 60 MHz are measured and all have mechanical Q-factors around 20000 as listed in table 5.1. Even though the cantilever only interacts with a small portion of the MZI arm, the detection method is still effective at transducing the cantilever signal.

The mass sensitivity of a single cantilever is estimated by measuring its frequency stability while implemented into a phase-locked loop (PLL). The frequency stability is measured experimentally using the Allan deviation [38].

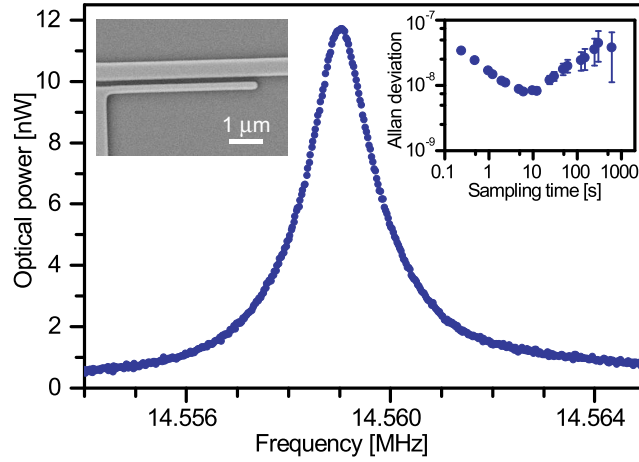


Figure 5.4: Frequency response curve of a typical cantilever (left inset) detected using an MZI device. The Allan deviation of this device is plotted in the right inset for various sampling time constants, with the error bars significantly smaller than the size of the data points. Adapted from [67].

The PLL actuates the device at its mechanical resonance and tracks the change in the phase response, applying feedback to keep the frequency as stable as possible. The inset in figure 5.4 shows the Allan deviation for various sampling time constants. The negative and positive slope values are consistent with white noise and random walk noise sources, respectively. Estimating the mass sensitivity using equation 2.28,  $\delta m = -2 \frac{m_{\text{eff}}}{\omega} \delta \omega$ , with a 5 second sampling time and an Allan deviation of  $8 \times 10^{-9}$  gives an estimated mass sensitivity of approximately 2 zg for a cantilever with a mass of 54 fg. This initial measurement beats the reported state-of-the-art sensitivity for top-down fabricated devices, which is impressive as the measurement was taken with a 5 times higher mass resonator and at room temperature as opposed to 4 K [88].

Verifying the interferometric detection scheme is important as a mechanism based on a changing phase is much more conducive for use in a multiplexed system. If the detection mechanism is dependent on scattering losses caused by the cantilever/waveguide proximity, successively more and more power will be lost for each added device causing signal degradation. With a phase de-

Table 5.1: List of cantilever dimensions, resonant frequencies, and mechanical quality factors

Length ( $\mu\text{m}$ )	Thickness (nm)	Gap (nm)	Frequency (MHz)	$Q_{\text{mechanical}}$
2.0	190	149	60.43	41300
2.5	203	109	43.21	19500
2.5	193	155	38.53	16100
3.0	194	140	26.25	25300
3.0	237	136	32.45	18600
3.5	192	135	20.90	16200
3.5	238	129	23.99	22900
3.5	185	151	19.22	35500
4.0	198	120	16.02	21200
4.0	186	146	14.69	20700
4.0	245	141	18.40	26200
4.5	234	145	14.62	26700
4.5	234	140	14.56	17800

tected system each individual device could be tuned to respond at a specific wavelength, therefore avoiding higher and higher losses with a larger number of multiplexed devices. In a phase system a single wavelength could also be used for detection if the devices could be differentiated based on their mechanical frequency. Multiplexing offers a solution to the issue of low capture efficiency for small nanomechanical structures. A large array could be implemented to offset the small individual size, and efficient multiplexing would reduce the overall complexity of the readout system.

The mechanism of the nanomechanical cantilever changing the optical path length in one MZI arm (and therefore the phase of the signal) is verified by looking at the strength of the detected mechanical signal as a function of the probe laser wavelength. The mechanical signal strength should follow the magnitude of the DC transmission slope which corresponds to the constructive and destructive interference fringes of the MZI. If scattering losses were the primary mechanism the signal would be dependent on the magnitude. As figure 5.5 shows the signal magnitude does scale with the optical transmission

slope. The signal magnitude is measured by the amplitude of the signal, with the error calculated from the fitting error in the peak height. The trends match very well, with the maximum and minimum signals corresponding to the maximum and minimum MZI slope. Positive and negative values for the normalized signal are dictated by the relative phase difference of the signals. The positive and negative signals are separated by a phase of  $180^\circ$  which corresponds to half of an MZI fringe.

## 5.4 MZI device optomechanical calculations

Lastly, the displacement detection responsivity and the optomechanical coupling constant can be estimated for the  $4.5\ \mu\text{m}$  long,  $234\ \text{nm}$  thick and  $220\ \text{nm}$  wide device in figure 5.4 . In the estimation the simulated effective index versus gap spacing curve found in figure 5.2 (b) is used to find the index change per gap spacing of  $-2.8 \times 10^{-5}\ \text{nm}^{-1}$  at the fabricated gap spacing of  $145\ \text{nm}$ . The phase change due to the cantilever moving toward a waveguide will equal [37]

$$\Delta\phi = \Delta n_{\text{eff}} \frac{2\pi}{\lambda} l = \Delta g \frac{\partial n_{\text{eff}}}{\partial g} \frac{2\pi}{\lambda} l \quad (5.1)$$

where  $\phi$  is the phase,  $n_{\text{eff}}$  is the effective index of refraction of the mode,  $\lambda$  is the free space wavelength of the probe,  $l$  is the length of the resonator, and  $g$  is the gap spacing between the cantilever and the waveguide.  $\frac{\partial n_{\text{eff}}}{\partial g}$  is the change in the effective index due to the changing gap spacing and is taken from simulation. Ultimately this will cause a change in the output power of the MZI and the transduction coefficient, the change in transmission power due to the changing waveguide-cantilever gap, is defined as

$$\frac{\partial T(\phi)}{\partial g} = \frac{\partial T(\phi)}{\partial \phi} \frac{\partial \phi}{\partial g} \quad (5.2)$$

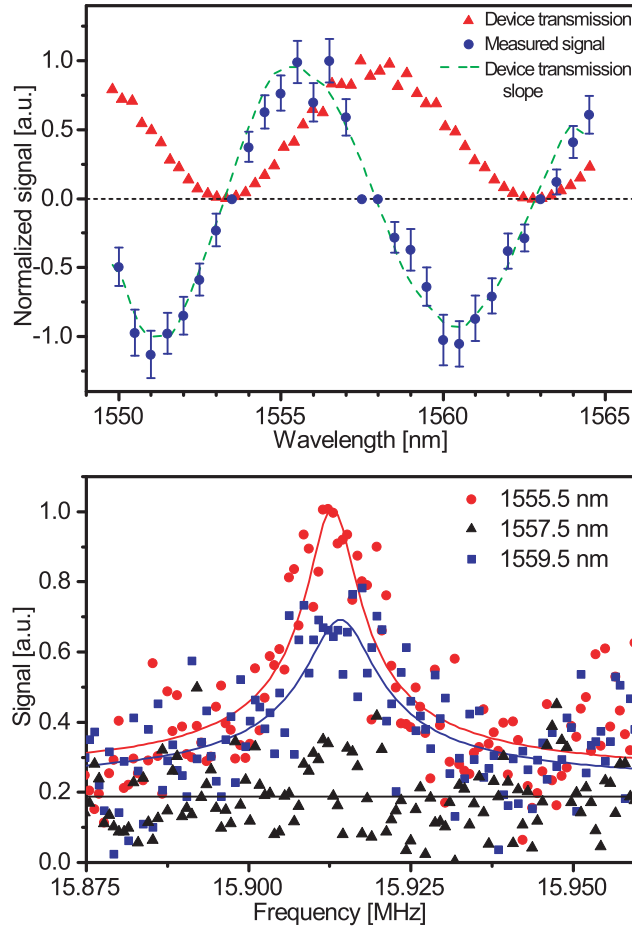


Figure 5.5: (a) Normalized DC optical power as a function of probe wavelength (triangles) over more than a complete MZI fringe in arbitrary units. The numerical slope of the smoothed power transmission curve is shown with the dashed line. The measured mechanical signal is plotted with circles, with the error bars representing the error in the fitted peak height. Adapted from [67] (b) The mechanical signal peak heights corresponding to different peak values with solid lines representing their Lorentzian fit. The high noise level in the mechanical response is caused by a low driving signal.

Here  $\frac{\partial T(\phi)}{\partial \phi}$  equal to the phase sensitivity, and  $\frac{\partial \phi}{\partial g}$  derived from equation 5.1. To take into account the mode shape of the cantilever and the fact that there will be a varying gap along the length of the cantilever the factor  $\beta$  is introduced.

$\beta$  is the average displacement factor of the resonator and is derived from the average value of its mode shape in reference to the tip displacement. This is 0.394 for the first cantilever mode. As such equation 5.1 reduces to

$$\frac{\partial \phi}{\partial g} \approx \frac{2\pi}{\lambda} \frac{\partial n_{\text{eff}}}{\partial g} \beta l \quad (5.3)$$

Finally, phase sensitivity can be calculated from the DC optical wavelength scan of the device. This is done by converting the power change caused by a changing wavelength to a power change caused by a changing phase. To convert the relation that the free spectral range,  $FSR$  is equal to a  $2\pi$  phase shift is used.  $\partial T/\partial \lambda$  is simply the slope of the optical DC transmission curve at the probe wavelength.

$$\frac{\partial T(\phi)}{\partial \phi} = \frac{\partial T}{\partial \lambda} \frac{\partial \lambda}{\partial \phi} = \frac{\partial T}{\partial \lambda} \left( \frac{FSR}{2\pi} \right) \quad (5.4)$$

Using these equations the device in figure 5.4 is probed at 1562.6 nm with a  $\partial T/\partial \lambda$  of  $1.6 \mu\text{W nm}^{-1}$  and a  $FSR$  of 9.24 nm. This gives a phase sensitivity of  $2.0 \times 10^{-4} \text{ rad nm}^{-1}$  and a transduction coefficient value of  $468 \text{ pW nm}^{-1}$ . This transduction coefficient estimates a cantilever tip peak displacement of about 25 nm for this device.

The displacement sensitivity of the MZI device can also be calculated using the transduction coefficient value. The sensitivity is determined by the minimum displacement amount that will give a signal larger than the measurement noise floor. The measurement noise floor is  $8.6 \times 10^{-12} \text{ W Hz}^{-1/2}$ , which gives a displacement sensitivity equal to  $18 \text{ pm Hz}^{-1/2}$ .

## 5.5 MZI NOMS pump probe

To fully take advantage of the high frequency and operational bandwidth benefits NOMS devices have over traditional nanomechanical actuation and transduction methods, it is important to be able to drive the nanomechanical device

optically as well. This is accomplished by modulating an optical gradient force on the beam caused by a guided pumping beam's evanescent fields. The power of the pump is modulated which modulates the strength the beam is pulled toward the waveguide. A schematic of the system is shown in figure 4.2.

A  $4.5\ \mu\text{m}$  long cantilever device with a mechanical Q-factor of 13500 is implemented into the optical pump/probe system. The probe laser is situated at the area of largest optical DC transmission slope for greatest transduction, while the pump laser is tuned about 10 nm away to be heavily attenuated by the band-pass filter that only allows the probe laser to reach the photo diode. The wavelength of the pump beam is not critical as a broadband y-splitter is used to separate the paths in the MZI, and it interacts with the nanomechanical beam before the paths recombine. The DC power of the probe laser at the cantilever is  $180\ \mu\text{W}$ ,  $270\ \mu\text{W}$ ,  $360\ \mu\text{W}$ , and  $450\ \mu\text{W}$  corresponding to an AC modulation on that power of  $24\ \mu\text{W}$ ,  $36\ \mu\text{W}$ ,  $48\ \mu\text{W}$  and  $60\ \mu\text{W}$ , respectively, for the responses shown in figure 5.6. The measurements were taken at a measurement bandwidth of 10 Hz and no averaging.

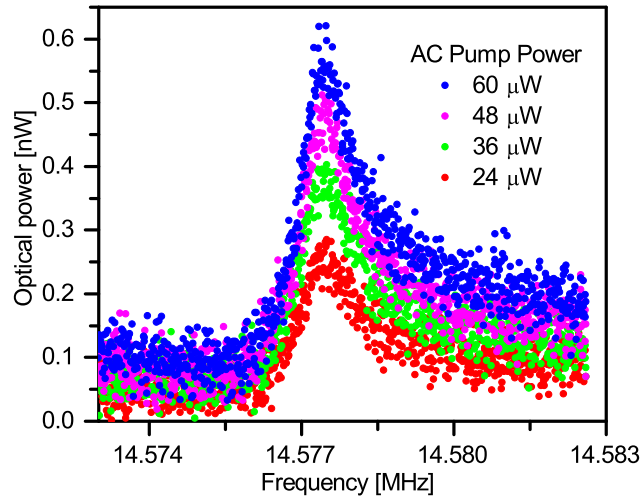


Figure 5.6: Mechanical response of a cantilever both driven and detected using an all optical nano-optomechanical system setup.

The asymmetry seen in the peak could be caused by the mixing of the modulating pump laser with the signal from the nanomechanical response. The two

signals will add with varying phase across the frequency scan to first cause a reduction in the noise floor before reaching the signal peak. This is also supported by the fact that the noise floor increases off resonance with higher AC pumping powers. This indicates that some of the pump laser's signal is passing through the filter and reaching the detector. The erbium doped fiber amplifier used to increase the pump laser power also broadens the laser's line-width so it is plausible that some of the signal passes through the filter. This asymmetry should be decreased with either a wider separation between the wavelength of the probe and pump lasers or also by tuning the pump laser to an optical wavelength where there is complete destructive interference upon recombination in the MZI. Both of these actions should reduce the total amount of pump laser signal at the detector and hence the amount of nonlinearity in the signal.

## 5.6 MZI readout discussion

A maximum mass sensitivity for a device can be achieved while it is operating just below the onset of non-linearity at its critical amplitude. This follows from the relation of mass sensitivity to the dynamic range of the device,  $\delta m = 2(m_{\text{eff}}/Q)10^{-\text{DR}/20}$  [1], where the dynamic range, DR, will be maximized if the device is driven just below its critical amplitude. For a cantilever this critical amplitude is given by  $y_{\text{max,canti}} = 5.46 (l/\sqrt{Q})$  [89]. For an optimal design the gap should be close to this critical amplitude. The device in figure 5.4 has a critical amplitude of about 184 nm and this is fairly well matched to the 140 nm gap spacing.

A special characteristic of the NOMS readout mechanism is the ability to increase or maintain the dynamic range of the device as it is scaled smaller. As a nanomechanical beam decreases in length the critical amplitude becomes smaller. This enables the device to be placed closer to the nanomechanical waveguide which increases the value of  $\partial n_{\text{eff}}/\partial g$ . The exponential  $\partial n_{\text{eff}}/\partial g$  dependence will lead to gains over the linear dependence on length for both the critical amplitude [90] and the transduction coefficient as the device becomes

smaller.

A shorter beam length can also be dealt with by switching to NOMS detection with an optical cavity. An optical cavity with high finesse increases the slope of the transmission versus phase curve which therefore leads to gains in the transduction sensitivity. All these gains lead to better detection at the lower end of the dynamic range so the full dynamic range can be realized. A high DR equates to good frequency stability which could lead to maintaining part per billion frequency fluctuations while scaling top-down fabricated nanomechanical resonators below femtogram masses. With these characteristics the sub-dalton mass sensitivity regime should be accessible to NOMS devices.

## 5.7 Conclusion

Mach-Zehnder interferometer integrated photonic devices are used to detect size independent nanomechanical cantilevers. This is achieved by fabricating the nanomechanical devices adjacent and external to the photonic waveguide structure to remove the size dependent properties for carrying a traveling optical mode. The cantilevers oscillate within the evanescent field of the detection arm of an MZI and this causes a modulating phase change in the arm. This is detected through the modulating output power after the two MZI arms recombine and interfere. A simple y-splitter is used to create the two MZI paths which allows for broadband operation. The devices are driven in the plane of the wafer by mounting the photonic chip to a frequency swept shear mode piezoelectric crystal.

The traveling optical mode of the waveguide and adjacent cantilever is simulated verify the geometry does not support traveling optical modes in the cantilever. The external cantilever would also allow analyte particles to deposit on the mechanical sensor without disrupting any optical modes. This disruption could cause signal loss and degradation. The device's frequency stability is measured while being driven in a phase-locked loop and an approximate mass sensitivity of 2 zg is measured. This level is state of the art for

top-down fabricated mechanical resonators. The displacement sensitivity of the device is also found and is equal to  $18 \text{ pm Hz}^{-1/2}$ .

The phase interaction mechanism of the MZI cantilever detection is verified. If using a nanomechanical beam as a mass sensor one drawback would be the beam's low capture efficiency. This can be mitigated by making a large array of nanomechanical sensors and multiplexing them for measurement in parallel. Phase based detection, as opposed to scattering based, should allow signals to remain high with each additional multiplexed beam.

Finally, the cantilever devices are driven using an optical pump to demonstrate all optical operation. This takes full advantage of optical signal properties for a large operational bandwidth. This could prove advantageous for nanomechanical sensors as they tend to increase in frequency as they become smaller in pursuit of higher mass sensitivity. Optical operation does not suffer the disadvantage of frequency roll-off which electronic systems are susceptible to. The NOMS actuation and detection method is also well suited for decreasing device sizes as their transduction ability can actually increase as the system is scaled down. These properties demonstrate the potential of NOMS actuation and transduction in state-of-the-art nanomechanical mass sensors.

---

---

## CHAPTER 6

---

# Racetrack resonator transduction of nanomechanical cantilevers

### 6.1 Introduction

To improve the detection capability of a NOMS system it is important to take advantage of optical cavity structures. An optical cavity will trap light within it which allows the light to interact many times with a nanomechanical structure instead of just once. How well an optical cavity traps light is defined by its finesse,  $\mathfrak{F}$ , which describes how many times light will circulate within the cavity before it dissipates. Compared to a Mach-Zehnder interferometer structure, as described in chapter 5, an equivalent optical cavity system with a finesse greater than 2.5 will yield superior transduction capabilities [37].

This chapter describes the nanophotonic detection of nanomechanical cantilevers using an integrated racetrack resonator optical cavity. The optomechanical coupling strength is investigated in relation to both nanomechanical beam and gap characteristics. It is verified using thermomechanical (TM) noise measurements of cantilevers with various lengths next to racetrack resonators at various gap spacings. The results compare favorably to derived expressions relating these parameters. The optomechanical coupling constant

is also derived from the TM noise of devices along with their DC optical power transmission responses. The racetrack resonators and external cantilevers can be both driven and detected optically, and the transduction is shown to be sensitive enough to detect the thermomechanical motion of an 80 fg modal mass cantilever operating at atmospheric pressure and room temperature. This chapter is based on the work found in reference [87].

## 6.2 Nano-optomechanical system geometry

Following from the design principles of the MZI device in chapter 5 a nanomechanical cantilever is fabricated adjacent to the nanophotonic structure to remove the size restriction from the optical mode condition. This is a natural evolution from earlier devices which utilized a waveguide directly as the nanomechanical beam [62, 91] but have more recently moved toward separate mechanical beams and photonic waveguides [66, 71, 67, 92, 93]. The mechanically independent structures not only remove the requirement of the mechanical beam supporting a guided optical mode, but any analyte masses added to the mechanical sensor will not disrupt the optical modes of the nanophotonic device.

Like the MZI device the racetrack resonator detection method relies on the external cantilever oscillating toward and away from the optical structure. As the gap spacing between the cantilever and the optical structure changes so does the effective index of refraction of the area adjacent to the cantilever. In the racetrack resonator case the optical path length in the cavity will then be modulated and hence so will the optical resonant frequency of the cavity. Figure 6.1 shows the DC optical transmission spectrum of a racetrack resonator as the probe wavelength is swept across it. The inset demonstrates a hypothetical optical resonance shift as the path length is changed due to the deflection of a nanomechanical beam. The racetracks are implemented into an all pass configuration in which a single bus is adjacent to the optical cavity. At resonance, optical power couples into the cavity causing a dip in the transmission.

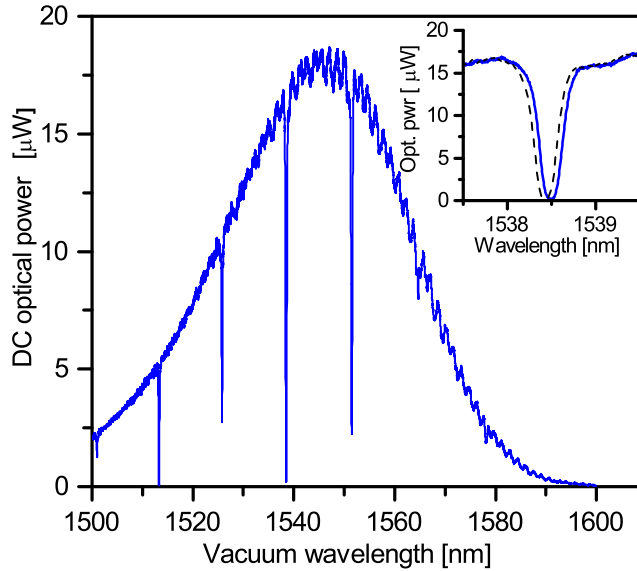


Figure 6.1: DC optical power transmission spectrum of a racetrack resonator optical cavity in an all pass configuration. The overall envelope is due to the limited bandwidth of the optical gratings used to couple light onto the chip. The inset illustrates the detection mechanism in which the deflection of a nanomechanical beam causes a shift (represented by the dashed line) in the optical resonance of the racetrack resonator. Adapted from [87]. Copyright 2014 IOP Publishing Ltd.

### 6.3 Derivation of the nanophotonic transduction responsivity

As with the MZI device the nanomechanical resonator peak displacement can be estimated using the transduction coefficient [37, 67]

$$\frac{\partial T(\phi)}{\partial g} = \frac{\partial T(\phi)}{\partial \phi} \frac{\partial \phi}{\partial g} \quad (5.2)$$

where the first term on the right hand side of the equation relates to the optical cavity properties while the second term on the right hand side is dependent on the device's optomechanical coupling constant. This is expanded using

experimentally accessible parameters by substituting equations 5.3 and 5.4 into equation 5.2 which results in

$$\frac{\partial T(\phi)}{\partial g} = \left( \frac{\partial T}{\partial \lambda} \frac{FSR}{2\pi} \right) \left( \frac{2\pi}{\lambda} \frac{\partial n_{\text{eff}}}{\partial g} \beta \chi l_c \right) \quad (6.1)$$

Here,  $l = \chi l_c$  in which  $l_c$  is the optical cavity length and  $\chi$  is the proportional length of the mechanical resonator to the length of the optical cavity.

More generally, equation 6.1 can be expressed in terms of the optical cavity properties. To start, the normalized transmission (hat notation) of an all pass ring resonator is defined as [94]

$$\hat{T}(\phi) = \left( \frac{\hat{T}_{x,\min} + (2\mathfrak{F}/\pi)^2 \sin(\phi/2)^2}{1 + (2\mathfrak{F}/\pi)^2 \sin(\phi/2)^2} \right) \quad (6.2)$$

where  $\hat{T}_{x,\min}$  is the minimum of the normalized transmission at the bottom of the optical dip and  $\mathfrak{F}$  is the finesse of the cavity. The phase sensitivity at the maximum slope can then estimated as [37]

$$\left( \frac{\partial \hat{T}(\phi)}{\partial \phi} \right)_{\max} = \frac{3\sqrt{3}}{8\pi} (1 - \hat{T}_{x,\min}) \mathfrak{F} \quad (6.3)$$

which leads to a maximum transduction coefficient for normalized transmission as:

$$\left( \frac{\partial \hat{T}(\phi)}{\partial g} \right)_{\max} = \left( \frac{3\sqrt{3}}{8\pi} (1 - \hat{T}_{x,\min}) \mathfrak{F} \right) \left( \frac{2\pi}{\lambda} \frac{\partial n_{\text{eff}}}{\partial g} \beta \chi l_c \right) \quad (6.4)$$

For a non-normalized transmission, if  $T_0$  is equal to the power entering the ring, and  $\alpha$  is the extinction ratio of the dip measured in dB, the transduction coefficient becomes:

$$\left( \frac{\partial T(\phi)}{\partial g} \right)_{\max} = \frac{3\sqrt{3}}{8\pi} T_0 (1 - 10^{-\alpha/10}) \mathfrak{F} \left( \frac{2\pi}{\lambda} \frac{\partial n_{\text{eff}}}{\partial g} \beta \chi l_c \right) \quad (6.5)$$

To now derive the transduction coefficient dependence on the optomechanical coupling constant,  $g_{\text{om}} = 2\pi(\partial\nu/\partial g)$  with  $\nu = c/\lambda$ , the following relation is used which is derived from the chain rule (note that  $g_{\text{om}}$  should not be confused with the gap spacing,  $g$ )

$$\frac{g_{\text{om}}}{2\pi} = \frac{\partial n_{\text{eff}}}{\partial g} \frac{c}{\lambda n_{\text{eff}}} \quad (6.6)$$

The transduction coefficient in terms of general optical cavity metrics then becomes:

$$\left(\frac{\partial T(\phi)}{\partial g}\right)_{\text{max}} = \frac{3\sqrt{3}}{4} T_0 (1 - 10^{-\alpha/10}) \mathfrak{F} \left(\frac{g_{\text{om}}}{2\pi}\right) \frac{n_{\text{eff}}}{c} \beta \chi l_c \quad (6.7)$$

Here, the system responsivity is shown to be proportional to the input power,  $T_0$ , the cavity finesse,  $\mathfrak{F}$ , the optomechanical coupling constant,  $g_{\text{om}}$  and the cavity length undergoing interaction,  $\chi l_c$ . Its implications are further discussed in section 6.9.

## 6.4 Extraction of absolute displacement and the $g_{\text{om}}$

If the device is resonating due to thermomechanical fluctuations equation 6.7 can be manipulated to equate the total signal power integrated over the frequency response,  $P_{\text{total}}$ , with the tip displacement due to the TM noise  $z_{\text{peak}}$ :

$$P_{\text{total}} \approx z_{\text{peak}} \frac{3\sqrt{3}}{4} T_0 (1 - 10^{-\alpha/10}) \mathfrak{F} \left(\frac{g_{\text{om}}}{2\pi}\right) \frac{n_{\text{eff}}}{c} \beta \chi l_c \quad (6.8)$$

With knowledge of the cavity properties and the noise spectrum power the TM displacement can be measured at cantilever resonance. Exact cavity properties do not even need to be directly calculated if  $\partial T(\phi)/\partial\phi$  is measured from the

DC optical transmission curve and equation 5.4. Equation 6.8 can then be expressed back in its original form

$$\frac{P_{\text{total}}}{\partial T(\phi)/\partial \phi} \approx z_{\text{peak}} \left[ \left( \frac{2\pi}{\lambda} \right) \left( \frac{\partial n_{\text{eff}}}{\partial g} \right) \beta \chi l_c \right] \quad (6.9)$$

where the device dimensions can be used in conjunction with finite difference time domain modeling to estimate the square bracketed  $\partial\phi/\partial g$  term. From these measurements the absolute value of the displacement caused by the TM noise can be estimated, and this is shown in figure 6.7.

It is also possible to estimate the  $g_{\text{om}}$  from a series of TM noise measurements. First, equation 6.9 can once again be rewritten to include the  $g_{\text{om}}$  term:

$$\frac{P_{\text{total}}}{\partial T(\phi)/\partial \phi} \approx z_{\text{peak}} \left[ \left( \frac{g_{\text{om}}}{2\pi} \right) \frac{2\pi n_{\text{eff}}}{c} \beta \chi l_c \right] \quad (6.10)$$

With this form of the equation the theoretical calculations of the TM noise displacements can then be used in conjunction with a series of the TM noise curves to experimentally determine the  $g_{\text{om}}$  for different gap spacings. The optomechanical coupling constant is extracted from the slope of the  $P_{\text{total}}/(\partial T(\phi)/\partial \phi)$  versus  $z_{\text{peak}} \chi l_c$  curve at each gap value. This is a distinct method of directly measuring the  $g_{\text{om}}$  [95, 96] in any case where the DC optical transmission spectrum can be measured and the effective index simulated. It is important to note that this method of measuring the  $g_{\text{om}}$  does not require the devices to be optically driven, nor does it require a measurement of the optical force on the device [80, 97, 98, 91]. It can also be implemented without an AC calibration signal [95].

## 6.5 Device fabrication

A racetrack resonator optical cavity structure is chosen to detect the nanomechanical cantilever. A racetrack is chosen instead of a more conventional ring

resonator so the cavity has a flat region to run parallel to the cantilever and the cavity-beam interaction can occur in a straightforward manner. An all pass cavity configuration is used where the oval racetrack is adjacent to the waveguide bus on one side with the nanomechanical cantilever on the other as shown in figure 6.2. The optical cavity length around the racetrack determines the characteristic wavelengths in which light can couple from the waveguide bus into the optical cavity structure. The light becomes trapped within the cavity and completes a certain number of oscillations before dissipating and this number describes the optical finesse,  $\mathfrak{F}$ , of the cavity. The structures fabricated have finesse values around 50 to 70. The devices were not optimized for maximum finesse and this explains their relatively low values compared to typical integrated photonic optical cavities. Even with these lower finesse values the nanomechanical transduction characteristics for the system are still very good.

The devices are fabricated on standard integrated photonics SOI wafers with a 220 nm silicon device layer and 2  $\mu\text{m}$  buried oxide layer. They are also fabricated using standard integrated photonics methods with I-line lithography at the IMEC foundry. The fabrication was facilitated through a CMC Microsystems design competition. Cantilevers 1.5  $\mu\text{m}$  to 5  $\mu\text{m}$  long and about 160 nm wide were fabricated with gap spacings from the racetrack resonator of 70 nm to 160 nm. The fabricated width of the cantilevers has a  $\pm 10$  nm variation due to proximity effects during the lithography patterning, with the thicker beams fabricated with smaller gaps. The waveguides are 430 nm wide and the racetracks have a 5  $\mu\text{m}$  bend radius and 3  $\mu\text{m}$  long straight portion. The cantilever base is aligned to the beginning of the straight portion of the racetrack if the cantilever is shorter than 3  $\mu\text{m}$ , and if longer than 3  $\mu\text{m}$  the cantilever tip is aligned to the end of the straight portion of the racetrack. This is to ensure that the maximum deflecting portions of the cantilever are interacting with the straight portion of the racetrack, and also that the anchor pad of the cantilever is as far away from the waveguide as possible.

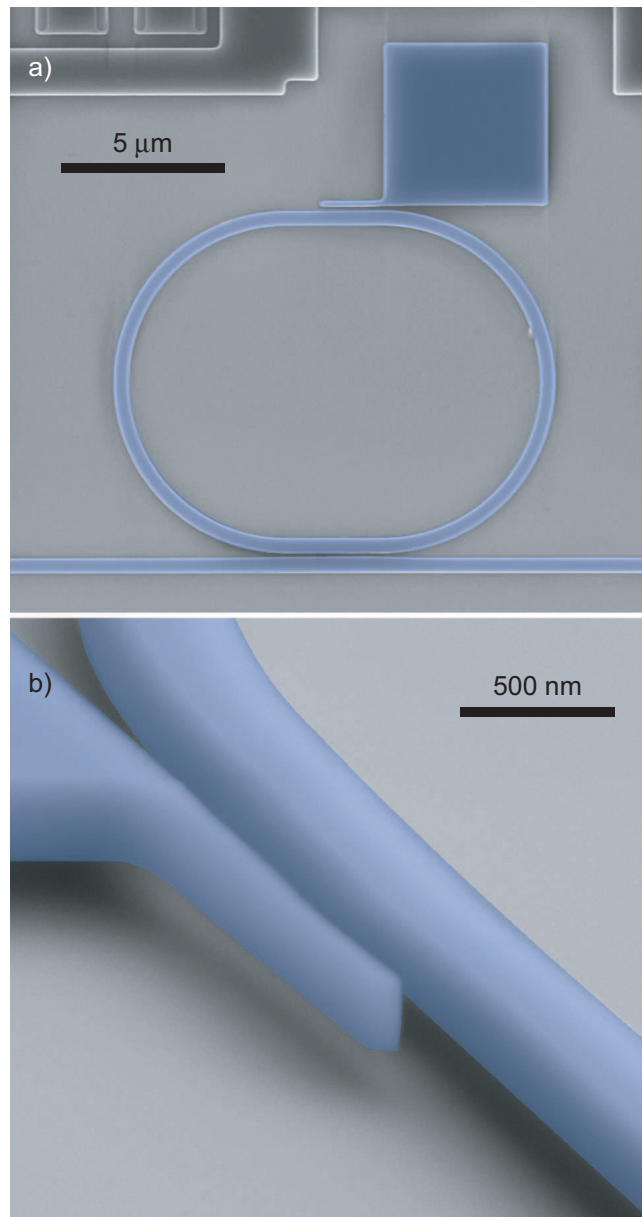


Figure 6.2: Colorized SEM of (a) a top down view of a typical racetrack resonator used to detect the nanomechanical cantilever (top) and (b) a close up view taken at  $70^\circ$  tilt of a released cantilever adjacent to the straight portion of the racetrack resonator. The oscillating mode of the cantilever moves toward and away from the waveguide. Adapted from [87]. Copyright 2014 IOP Publishing Ltd.

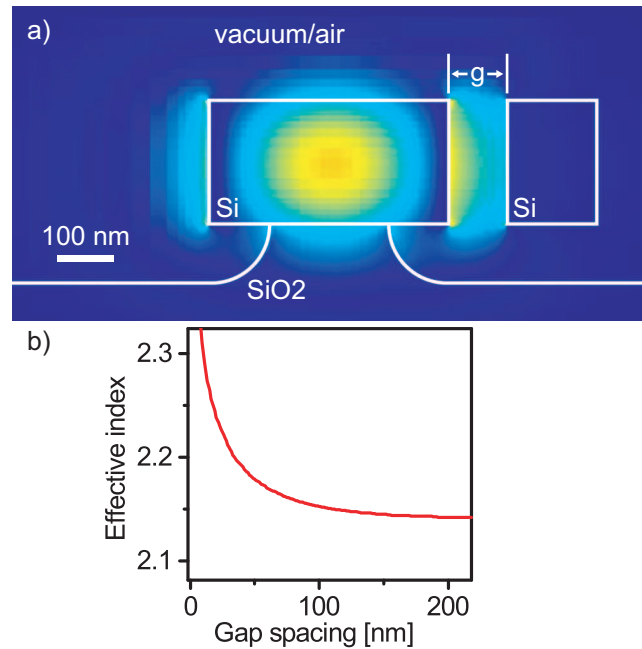


Figure 6.3: (a) Cross sectional view of the traveling optical mode simulation of a waveguide (center) with a smaller released mechanical resonator adjacent to it (right). The simulations were performed using finite difference time domain software. The mode is mostly confined to the waveguide, but it is also pulled slightly into the waveguide-resonator gap. The waveguide is partially under-etched while the mechanical resonator is being released using an isotropic wet etch. Adapted from [87]. Copyright 2014 IOP Publishing Ltd. (b) The simulated effective index of the mode versus the gap spacing between the waveguide and the cantilever.

To facilitate a mask-less BOE release step the cantilevers are fabricated much narrower than the waveguides. This enables a timed undercut to remove the silicon dioxide from underneath the cantilever while the waveguides remain supported. This etch step is not expected to significantly affect the losses in the waveguide as sidewall roughness is the main contributor [86]. The narrow size of the nanomechanical cantilevers also prevent the beams from carrying an independent traveling optical mode. This can be seen in the finite difference time domain (FDTD) simulations of the mode which are completed using

commercially available Lumerical FDTD software and shown in figure 6.3. The simulations are also used to plot the effective index change versus gap spacing for the cantilever next to the waveguide.

### 6.5.1 Measurement system

The devices are detected using a free-space confocal lens system coupling scheme [81]. A tunable diode laser is coupled onto the nanophotonic chip using focus grating couplers. The free-space confocal system allows the position and k-vector of the laser light on the grating couplers to be easily manipulated while the sample is in vacuum so maximum coupling efficiency may be achieved. The system is modified slightly with the addition of a second pumping laser. The second laser passes through an electro-optic modulator to varying the pump beam power and the optical gradient forces caused by it. The two lasers are combined along the same path using a directional coupler. A band pass filter is used to block the pumping beam prior to the photodiode detecting it. The complete setup is described in chapter 4.

TE-mode light is coupled into the chips through the grating couplers. For out of plane motion TM-mode light has a better phase sensitivity for waveguide-mechanical beam gaps below 100 nm, so with in plane motion TE-mode light should perform better. The difference between the modes becomes negligible with gaps above 100 nm [37], however, and this is how most of devices are fabricated. Unless otherwise stated the device measurements are taken at room temperature and at pressures below  $1 \times 10^{-5}$  Torr to eliminate air damping on the nanomechanical devices.

## 6.6 Thermomechanical noise measurements, analysis and $g_{\text{om}}$ extraction

A large array of devices with varying nanomechanical beam lengths and optical cavity gap spacings are used to verify the transduction coefficient's dependence on the cavity properties and optomechanical coupling constant. Although the racetrack resonator optical cavities are designed to be identical variations arise in their optical properties due to slight non-uniformities in the fabrication. The optomechanical coupling constant is varied in a more controlled manner by changing the gap spacing between the cantilever and the racetrack.

A DC transmission scan, such as in figure 6.1, is performed prior to each measurement to ensure the maximum signal is achieved. In an all pass configuration the optical resonances correspond to the transmission dips. The maximum signal is achieved by setting the probe wavelength to the empirically determined location of highest DC optical scan slope which sets the probe to the largest possible  $\partial T(\phi)/\partial\phi$ . Typically this is found on the largest, center dip. The steepness of the slope on the sides of the optical resonance are determined by the optical properties of the racetrack resonator such that with two racetracks near critical coupling the device with a higher optical finesse will have a larger slope. The shifting optical resonance due to the modulating effective index caused by the nanomechanical beam motion causes an AC power modulation at the constant probe wavelength which is detected at the output photodiode.

The TM noise measurements are taken using an Agilent 8593e Spectrum Analyzer with a 1 kHz bandwidth and 16 times averaging. A typical response is shown in figure 6.4. The response shown is for a 4.86  $\mu\text{m}$  long cantilever with a 110 nm gap between it and the racetrack resonator. The signal is fit to a Lorentzian-like peak at  $y = y_0 + A[(f^2 - f_0^2)^2 + (f_0^2/Q)^2]^{-1/2}$  where  $f_0$  is the frequency of the mechanical resonator and  $Q$  is the mechanical quality factor. For the analysis the main point of interest is the measured signal's frequency

integrated total power.

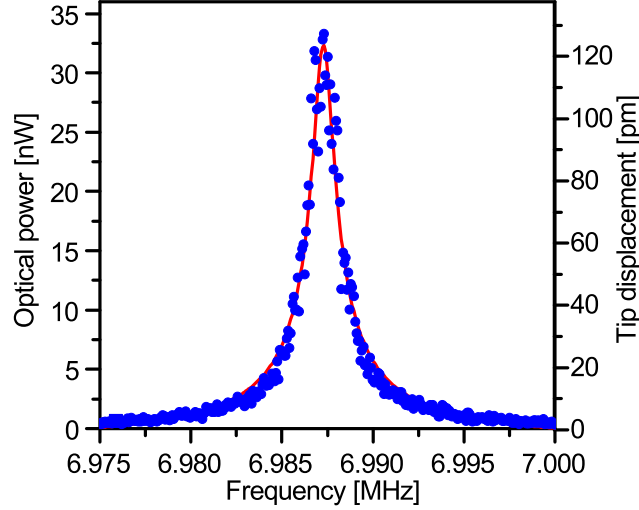


Figure 6.4: Thermomechanical noise response of a  $4.86 \mu\text{m}$  long cantilever with a  $110 \text{ nm}$  gap spacing taken at  $1 \text{ kHz}$  bandwidth and 16 times averaging.

The TM noise signal was measured for each of the cantilever devices of various length and gap spacing. Figure 6.5 plots the strength of the signal as a function of the cantilever length and the varying gap spacing between the cantilever and racetrack resonator optical cavity. As expected from equation 6.10 and figure 6.3 (b) the signal strength increases with longer devices as there is a larger area of phase change in the cavity. The signal also increases with smaller gaps which increase the  $g_{\text{om}}$ . To more readily compare the devices, which are each measured with their own optical cavities, the signals are normalized by each device's individual  $\partial T(\phi)/\partial \phi$  value. This removes the dependence of the signal on the optical cavity properties.

To extract the  $g_{\text{om}}/2\pi$  value the linear slope of the  $P_{\text{total}}/(\partial T(\phi)/\partial \phi)$  verses  $\chi l_c z_{\text{peak}}$  is extracted from device sets having the same gap spacing. The  $z_{\text{peak}}$  in the independent variable is theoretically calculated according to  $1/2k_{\text{eff}}\langle z \rangle^2 = 1/2k_{\text{B}}T_{\text{K}}$ . Here  $\langle z \rangle$  is the RMS displacement of the cantilever tip ( $z_{\text{peak}} = \sqrt{2}\langle z \rangle$ ),  $k_{\text{B}}$  is the Boltzman constant and  $T_{\text{K}}$  is the temperature in Kelvin. Illustrated in figure 6.6 the  $g_{\text{om}}/2\pi$  values of about  $6.5 \text{ GHz nm}^{-1}$  to  $24 \text{ GHz nm}^{-1}$

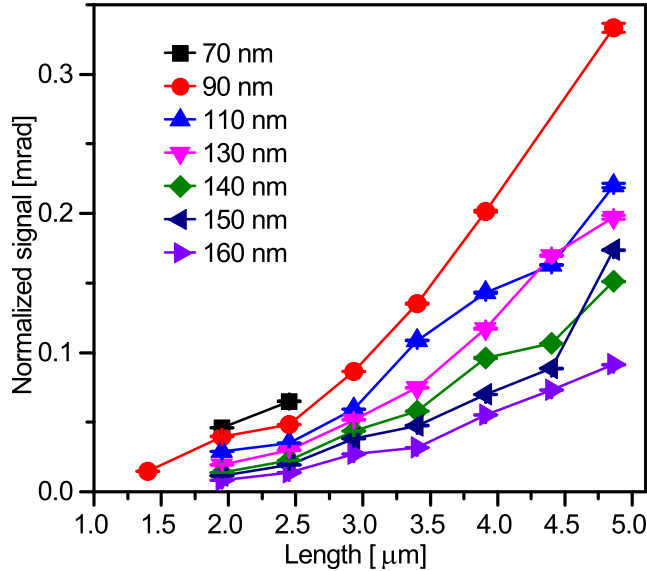


Figure 6.5: The TM noise signal power of cantilever devices of varying length and gap spacing between itself and the racetrack resonator. The signal is normalized by  $\partial T(\phi)/\partial\phi$  to account for the varying optical cavity properties. Adapted from [87]. Copyright 2014 IOP Publishing Ltd.

for gap spacings of 160 nm to 90 nm extracted from these slopes match well with the values calculated from the simulated  $\partial n_{\text{eff}}/\partial g$  values in figure 6.3 (b). This confirms the optomechanical coupling constant's effect on the transduction coefficient.

Lastly, to verify the total relation between the transduction coefficient, the optical cavity properties and optomechanical coupling constant, the cantilever tip displacement is calculated for each individual device. This displacement is compared to the theoretical displacement calculated from the nanomechanical cantilever's thermal energy. This is shown in figure 6.7.

The displacement sensitivity of each device can be calculated in a manner similar to that of the tip displacement. For these calculations the noise floor is divided by the transduction coefficient instead of the total power. With an input optical power of approximately 250  $\mu\text{W}$  the noise floor of the measurements

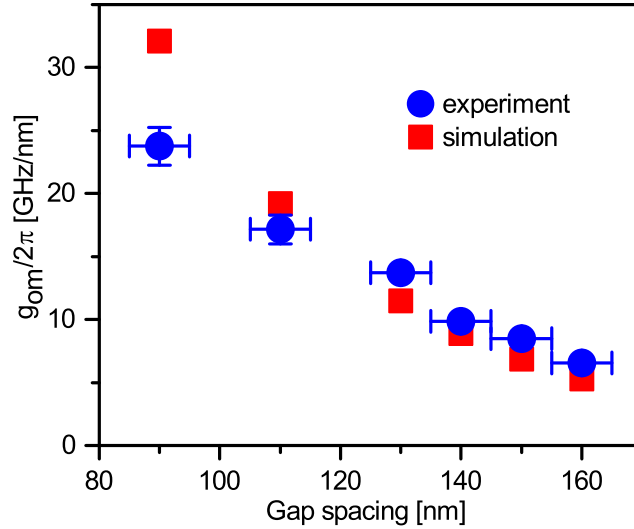


Figure 6.6: The optomechanical coupling constants calculated from normalized TM noise signal powers of cantilevers of various lengths for different gap spacings. Simulated  $g_{om}/2\pi$  values are extracted using Lumerical FDTD software. Adapted from [87]. Copyright 2014 IOP Publishing Ltd.

is about  $8.5 \text{ pW Hz}^{-1/2}$ . Depending on the transduction coefficient of each device this leads to a displacement sensitivity of approximately  $16 \text{ fm Hz}^{-1/2}$  to  $230 \text{ fm Hz}^{-1/2}$  with the majority of the devices lower than  $100 \text{ fm Hz}^{-1/2}$ . The  $\partial T(\phi)/\partial z$  values are in the range of  $47 \text{ nW nm}^{-1}$  to  $537 \text{ nW nm}^{-1}$ .

## 6.7 Optical pump and probe measurements

To increase the signals of the devices an external driving force is required. For the greatest mass sensitivity the devices should be driven until just below the onset of non-linearity to operate at the maximum dynamic range of the device [18]. With the Mach-Zehnder interferometer structures in the previous chapter the devices were driven using a shear mode piezoelectric crystal, but for greatest versatility a driving method with less frequency limitations is desirable. Piezoelectric crystals usually have limited frequency ranges (typically below

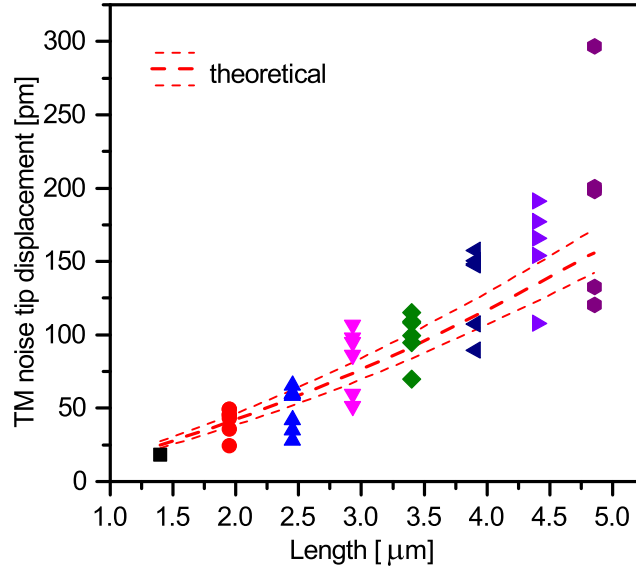


Figure 6.7: Cantilever tip displacements measured by racetrack resonator optical cavities. The different data points at each length correspond to devices with varying gap spacings. The spread in the data for each length is due to the slight variation in the cantilever thicknesses caused by proximity effects while fabricating the devices with different gap spacings. The smaller gaps pair with slightly thicker and therefore stiffer beams. The theoretical values are for average beam thicknesses of  $160 \pm 10$  nm. Adapted from [87]. Copyright 2014 IOP Publishing Ltd.

20 MHz) and are limited by RLC time constants which make high frequency operation difficult. As an alternative, it is easy to implement an optical pumping mechanism into a nanophotonic detection setup which does not suffer from these frequency limitations. An optical gradient force is created between the waveguide and adjacent cantilever due to the evanescent fields extending from the waveguide [80, 99, 78]. The pump laser is introduced into the system path with the probe laser prior to the confocal system using a directional coupler. This co-aligns the lasers and hence only a single positional alignment of the laser path is required onto the photonic chip. The pump laser is filtered out of the system using a band pass filter prior to the photo detector.

To ensure the band pass filter does not allow any of the pump laser through, the pump and probe laser are set at different optical resonance modes of the racetrack resonator. This allows for sufficient wavelength separation between the two sources. The pump laser is set to the peak optical resonance while the probe laser is still set to the area of greatest slope. Setting the pump laser at an optical peak with a high extinction ratio also ensures minimal pump power reaches the photodiode. The inset of figure 6.8 shows the DC transmission spectrum of the device. The pump laser is set to the peak of the center left resonance at 1538.75 nm while the probe is at the center resonance at 1551.87 nm.

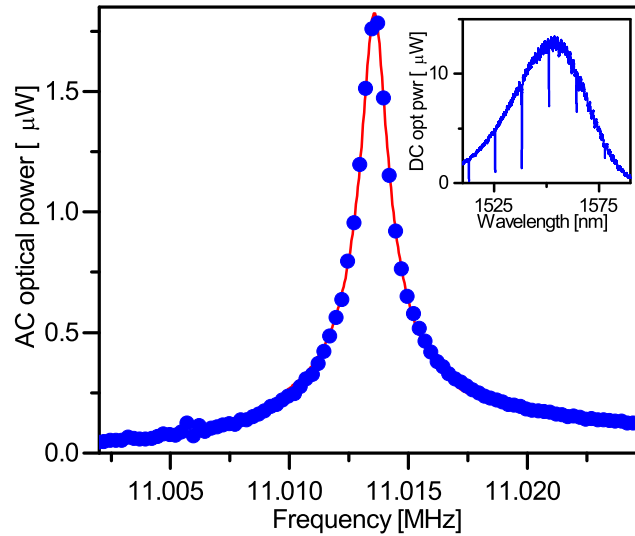


Figure 6.8: Optical pump and probe response of a 3.91  $\mu\text{m}$  long cantilever with a 110 nm wide gap spacing from the racetrack resonator. A modulated drive signal of 145  $\mu\text{W}$  enters the ring. The inset shows the DC optical transmission spectrum of the device. The pump laser is set at 1538.75 nm and the probe is set at 1551.87 nm. The signal is taken with a 300 Hz bandwidth and 16 times averaging. Adapted from [87]. Copyright 2014 IOP Publishing Ltd.

To modulate the pump laser, and hence the optical force on the cantilever, an electro-optic modulator (EOM) is used. The  $V_\pi$  for the EOM, the voltage required to change from maximum to minimum output, is 3 V. The pump laser

is passed through the EOM which is fed into an erbium doped fiber amplifier (EDFA). The output of the EDFA is set at 8.37 mW with a 0 V<sub>AC</sub> input to the EOM. A HP 8752C network analyzer (NA) is used for both driving and detecting the device. For driving the device a 0.707 V<sub>peak</sub> signal from the NA is used to modulate the pump power between 2.70 mW to 14.04 mW exiting the EDFA. Due to losses in the system from the directional coupler (0.5), beam splitters, microscope objective (about 0.5) and fiber grating coupler (about 0.85 at peak), the pump laser power entering the ring is modulated between 35  $\mu$ W to 180  $\mu$ W. Figure 6.8 shows the mechanical response for the optically pumped and probed 3.91  $\mu$ m long cantilever with a 110 nm wide gap spacing. The signal is 200 times larger than the TM noise signal measured in vacuum for the device (not shown). To reach maximum dynamic range a higher laser pumping power could be used to further drive the device until just below the onset of non-linearity.

## 6.8 Atmospheric pressure thermomechanical noise measurement

If operating a nanomechanical beam as a gas sensor it is not always practical to take the measurements in vacuum to eliminate air damping and increase the mechanical signal. Ideally the sensor would operate at atmospheric pressure, or the pressure of the analyte gas medium, so pumps, valves and flow controllers would not be required. At higher gas pressures the mechanical beam operates in the viscous flow regime and the damping decreases the amplitude of the mechanical oscillations under a constant driving force, which is the cause of the decreasing signal.

Using an optical cavity is an effective method for detecting these smaller amplitudes, and the 3.91  $\mu$ m cantilever measured above demonstrates this with the measurement of its TM noise response at atmospheric pressure. The peak broadens due to damping caused by gas molecules and the signal decreases

due to smaller deflection as shown in figure 6.9. The quality factor, a measure of the damping, drops three orders of magnitude from 10000 to 30, and there is also a slight red shift of the TM frequency compared to the optically pumped device. The frequency shift is caused by the optical spring effect on the pumped device which is caused by the DC portion of the pump beam. The quality factor value of 30 fits the expected value from the gas damping model of a cantilever in the molecular flow regime [100, 101, 102]. Even with the large amount of mechanical damping the signal is still easily distinguishable, and this demonstrates the effectiveness of the nanophotonic optical cavity for transducing nanomechanical beams at atmospheric pressure.

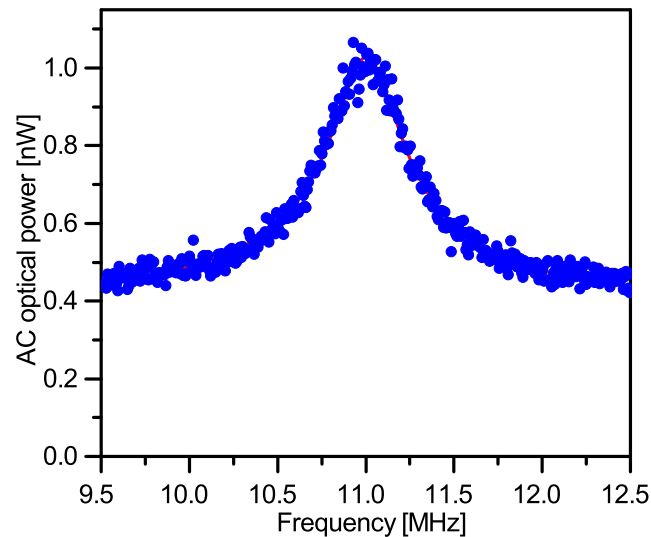


Figure 6.9: The thermomechanical noise response at atmosphere of a  $3.91\ \mu\text{m}$  long cantilever with a  $110\ \text{nm}$  wide gap spacing from the race-track resonator. The measurement is taken with a  $1\ \text{kHz}$  bandwidth and 16 times averaging. Adapted from [87]. Copyright 2014 IOP Publishing Ltd.

The atmospheric measurement also demonstrates the potential for using these devices in a gas viscosity sensor. The damping on a mechanical beam becomes dependent on gas viscosity as opposed to the gas pressure while oscillating in the viscous flow regime [102, 103, 104]. To measure the viscosity, the mechan-

ical Q-factor of the oscillating beam could be measured.

## 6.9 Discussion on the optomechanical transduction and mass sensitivity

Equation 6.7 suggests there are many photonic cavity system detection system properties that can be manipulated to maximize the transduction properties for nanomechanical beam motion. Looking at the cavity properties themselves, it makes sense that the signal is directly proportional to the power entering the cavity,  $T_0$ . The finesse of the cavity is important as the signal is also directly proportional to it. A high extinction ratio is required to be close to critically coupling in the optical resonator, but perfect critical coupling is not required to achieve satisfactory transduction results. With the mechanical beam characteristics the largest phase change in the optical cavity, and therefore greatest optical resonance shift, occurs when the mechanical beam is as close to the size of the cavity as possible. The beam should also be as close to the cavity as possible to maximize the optomechanical coupling constant. All these variables change the transduction coefficient linearly so any change in each of them will have the same proportional effect.

If operating the device as a nanomechanical mass sensor there are a few other factors to consider to maximize the mass sensitivity. If probing an unvarying mechanical device there is a certain limit in which the gains achieved from higher transduction coefficients no longer matter. This occurs when the noise floor determined by the optical cavity system is equal to the TM noise signal of the nanomechanical cantilever. This follows from the mass sensitivity metric of the minimal detectable frequency shift which is ultimately limited by the frequency fluctuations caused by the thermal displacement fluctuations of the nanomechanical beam.

If implemented into a phase-locked loop, these frequency fluctuations can be decreased by increasing the signal to noise ratio of the driven response to the

TM noise response. The ratio of these energies represents the dynamic range of the device which is always governed at its bottom end by the noise level of the system [18]. The maximum dynamic range is achieved when the device is driven just below the onset of mechanical non-linearity. No matter how low the system noise level is further improvements will not increase the dynamic range as the TM noise of the cantilever will remain the same.

Gains are achieved with a nanophotonic transduction system due to the system scaling down very well with smaller devices compared to other measurement systems. With better transduction capabilities the opportunity arises to always match the TM noise of the device. In this way the dynamic range can be maintained as devices become smaller (a method to increase the mass sensitivity), which is not the case with capacitive or free-space optical detection. The smaller nanomechanical devices lead to smaller displacements, and better optical cavities can compensate for the smaller detection thresholds. There is the added bonus that devices with smaller deflections can be placed closer to the optical cavity which then increases the optomechanical coupling constant and hence the measured signal further. The upper limit on the  $g_{om}$  is set by the critical amplitude of the nanomechanical resonator where the mechanical response becomes non-linear. If increasing the  $g_{om}$  does not bring the sensitivity level in line with the TM noise response of the beam, this can be compensated for by increasing the phase responsivity using the optical cavity properties. This flexibility to increase the detection limits is a significant advantage of using a nano-optomechanical sensing mechanism for transducing the motion of very small mechanical beams in a mass sensing application.

The mass sensitivity of these devices is expected to be similar to the Mach-Zehnder devices in chapter 5 and around the zeptogram level [67]. Improvements are expected since the transduction properties of the racetrack optical cavity are superior to that of the MZI. This is apparent in that the thermomechanical noise is measurable for similar devices with the racetrack resonator transducer, but not with the MZI transducer. Mass sensitivity gains are expected since stronger signals lead to reduced phase noise which allows better

feedback control using a phase-locked loop, and hence better frequency stability. Also, the racetracks allow the ultimate bottom end of the dynamic range to be detected with the TM noise. The zeptogram sensitivity level corresponds to the mass of individual proteins.

To differentiate between different proteins based on only their mass, yoctogram mass resolution is required. To circumvent this limitation other methods may be used in conjunction with mass sensing to analyze unknown proteins. As in gas chromatography the pre-separation of analytes may be used [27] to give more information on the analyte to allow for differentiation below the mass detection threshold. Surface functionalization of the mechanical beam may also be employed to target specified molecules for binding. This can be accomplished using gas phase silanization [105], or else by individually functionalizing specific mechanical beams using ink-jet printing [106, 107] or laser induced forward transfer [108]. The large deposition area of the latter two methods may be adapted for deposition onto a smaller nanomechanical beam with the use of an integrated nanostencil [109] such as that describe in chapter 8. An advantage of the integrated nanostencil is it could also be used to limit other effects on the mechanical beam frequency which are not due to mass loading such as changing surface tension or rigidity [110, 111, 112, 113, 114]. The deposition of mass could be targeted to the regions of low mechanical strain where the mass induced frequency change will dominate.

## 6.10 Consideration of other effects on the transduction responsivity

It is important to consider what other optical effects may come into play which could alter the transduction responsivity of the device. These could include other resonances or interferences beyond the effective index change. One such example is the Fabry-Perot cavity formed between the input and output grating couplers due to back reflections at the gratings [5]. These

cause the small power oscillations on the DC transmission scan across the entire grating bandwidth in figure 6.1 which have a period of approximately 3 nm and give a fringe visibility as high as 10%. This could translate into 10% responsivity variation depending on where the optical resonance of the racetrack falls in this pattern.

Reflections may also occur within the optical cavity itself. The presence of the cantilever causes a slight non-adiabatic change in the effective index of the ring which can cause reflections in the mode. This could possibly create interference effects along the length of the cantilever which could affect the phase change in this region. Since the cantilever does not support a guided mode a directional coupler type device will not be inadvertently created so these interferences should have small visibility and are not expected to have a noticeable effect. This is supported by the fact that evidence of these interferences is not present in the DC optical transmission versus wavelength curves as the optical dips have the expected shapes.

Leaky resonant modes of the cantilever are another potential source for interferometric enhancement or suppression of the transduction responsivity. Leaky resonances such as Mie modes have been shown to enhance light absorption in a nanowire with the proper geometry by over an order of magnitude [115, 116, 117]. In the present experimental geometry the  $k$ -vector of the light is parallel to the nanowire-like cantilever so no appreciable effect from these leaky mode resonances is expected. Although the Mie mode resonant enhancement occurs for a wide range of propagation angles it does tend to fall off as the light angle becomes parallel to the axis of the nanowire [117].

In addition to the angle argument the normalized nanowire diameter for the measured devices,  $nk d/2$ , where  $n$  is the refractive index,  $k$  is the optical wavevector, and  $d$  is the diameter [117] is about 1.1. This is only large enough to support the TM01 leaky mode resonance according to figure 2 (c) in reference [117], which is not supported by the TE mode light coupled into the device. Even if it was, the TM01 mode falls off more quickly due to the input angle than for the higher order modes. Most importantly, any appreciable

absorption of the cavity power by the cantilever into a leaky resonance mode would dramatically reduce the finesse of the optical cavity [118], and this reduction in finesse is not observed between devices with adjacent cantilevers and those without.

These other effects are important to consider when designing and analyzing NOMS devices. If the presence of one of these loss mechanisms inadvertently exists the transduction properties could fall off quite rapidly. These losses could be easily avoided with simple modifications to the sample geometry. It could be possible, however, to take advantage of these other mechanisms to enhance either the transduction or optomechanical interactions. For these reason it is important to be aware of them with similar device geometries.

## 6.11 Future perspectives

Integrated biosensors are currently being developed using several different approaches and technologies. As is typical with engineering problems the best solution will depend on the operation parameters of the sensor as well as the requirements of the sample preparation and sensor fabrication. If looking at the smallest limits of detection in a label-free environment, dynamic nanomechanical beam resonators have shown very good results compared to other techniques. These include optical micro-ring cavities on their own or sensing using nanowire field effect transistors [119]. Directly relevant to this work, dynamic mechanical beam limits of detection have been measured three orders of magnitude smaller than that of an optical micro-ring resonator on its own. Limits of detection for these devices have been measured at 0.3 pM versus 0.6 nM for unlabeled detection and 1.5 fM versus 6.5 pM for labeled detection for a mechanical beam and micro-ring, respectively. This result is not surprising considering that nanomechanical beams have exhibited single molecule detection [22, 23, 24, 16, 120]. This sensitivity comes at a cost, however, as nanomechanical beam detection is much more difficult to implement. This is especially true for detection of molecules in fluids where the damping on

the mechanical beam makes dynamic operation much more difficult. A static detection method such as a singular optical micro-ring would be much easier to implement if the base sensitivity required for the sensor was met. If ultra low levels of sensitivity are required which must use dynamic nanomechanical beam measurements, nanophotonic transduction is a very promising method for implementation.

## 6.12 Conclusion

Integrated optical cavities were used to transduce the motion of nanomechanical cantilever devices. This follows from previous experiments using nanophotonic Mach-Zehnder interferometer structures which were able to successfully detect beam motion. As expected, the use of an optical cavity in the form of a racetrack resonator provides much better signal transduction owing to the high finesse and increased optical interactions with the cantilever devices. This is most apparent by the ability to transduce the thermomechanical noise signals of the cantilevers with the racetrack resonator structures but not with the MZI structures.

The TM noise signals of cantilevers  $1.5\ \mu\text{m}$  to  $5\ \mu\text{m}$  long with cross sections of  $160\ \text{nm}$  by  $220\ \text{nm}$  were measured at room temperature and in vacuum. These signals were used to verify the transduction coefficient which is derived in relation to standard optical cavity metrics such as finesse and the optomechanical coupling constant. The optomechanical coupling constant is also extracted from the TM noise data for a group of devices with different cantilever-racetrack gap spacings.

As a proof of principle towards operation of the device in a mass sensing system the cantilever is both driven and detected using an all optical pump and probe setup using two separate laser sources. This demonstrates the system can fully operate optically to take advantage of the operational bandwidth advantages optical systems have over electronic ones. In support of operating the sensor in

a gaseous environment the TM noise of a cantilever is measured at atmospheric pressure and room temperature. This demonstration shows the effectiveness of using nanophotonics for detecting the motion of nanomechanical cantilevers even at high pressures. Overall, the transduction properties of a NOMS system show much potential for practical implementation into sensing systems.

---

---

## CHAPTER 7

---

### Multiplexing using nano-optomechanical systems

#### 7.1 Introduction

Nanomechanical beam resonators have demonstrated their ultimate target sensitivity at the yoctogram level [16]. The goal now is to utilize the technology in practically implemented sensor systems. Up until this point the avenue for reaching the desired sensitivity level was decreasing the device size while keeping transduction levels high and system noise down. This is how the yoctogram-level mass sensor came to be made of a carbon nanotube and was detected at temperatures below 58 K. Provided that measurement chamber conditions are not a concern there is still the general issue of the practicality of a nanomechanical resonator's size. The devices gain their point mass sensitivity due to their small size, but a smaller size implies that the capture area of the sensor is also small. A sensor will not function if the analyte particles cannot find the detector.

Luckily, nanomechanical sensors have been developed using traditional integrated circuit technologies. It follows that the fabrication processes are well suited to building thousands of these devices on a single chip. What a single nanomechanical beam lacks in capture area can be made up for using its integrability. If using an electronic detection system scaling the number of devices

up is not always trivial as an increased number of electrical connections must be integrated onto the chip. This can be mitigated if the entire array is detected using a full field interferometer [121] or else by connecting the array in a series-parallel configuration to address the entire array with a single input and output [26]. In the case of the full field interferometer a drawback is the entire array must be visible in the field of view, and this includes being able to resolve individual devices which will eventually meet diffraction limitations. In the series-parallel design the array of nanomechanical devices stop operating individually and instead operate as a single device with multiple parts. Each individual event is averaged across them all. Both of these methods are limited if looking to detect point masses on single nanomechanical beams.

Nanophotonic readout is well suited for the detection of multiple nanomechanical resonators. This follows from the ability to send multiple signals down a single photonic wire with a broad optical frequency range. A large array can be detected using a single probe and would not be limited by diffraction effects or signal averaging from the array. This has been demonstrated with the motion of 63 individual cantilevers being detected using the optical near field of an adjacent optical fiber [93]. The nanophotonic transduction in this case relies on scattering of the signal from the nanomechanical beams. This could cause issues because an increased number of devices lead to more signal scattering, and this could ultimately lead to more signal losses. In this chapter phase detection of multiple devices on a single nanophotonic waveguide bus is demonstrated.

## 7.2 Multiplex NOMS device design

Wavelength-division multiplexing (WDM) is a powerful property of optical fiber communication systems. It allows multiple signals sent at different carrier wavelength channels to be transported along a single fiber simultaneously [122]. This property has also transferred to integrated optical devices as well, especially with the use of optical ring resonator cavities [123]. It is easy to

imagine applying this technique to the detection of nanomechanical beam arrays using nanophotonic cavities.

To increase capture efficiency a large array of nanomechanical resonators must be implemented onto the chip. To decrease system complexity this ideally would be a multiplexed array where a single input and output could be used to measure all of the devices. To maintain signal independence the resonators' individual signals must be isolated, and a perfect way to do this would be through the use of WDM. This pairs perfectly with the fact that nanomechanical beam transduction is successfully executed using integrated optical cavities, devices which are also used for on-chip WDM.

To demonstrate nanophotonic device multiplexing two independent optical cavities are fabricated along a single nanophotonic waveguide in an all pass configuration as shown in 7.1. The racetrack resonators have a  $3\ \mu\text{m}$  straight portion and curves with a  $5\ \mu\text{m}$  radius. The mechanical doubly clamped beams are each about  $7.5\ \mu\text{m}$  long and  $160\ \text{nm}$  wide when viewed perpendicular to the surface of the wafer. There is a  $110\ \text{nm}$  gap spacing between the beam and the racetrack. The devices are fabricated on standard integrated photonic SOI wafers with a  $220\ \text{nm}$  thick device layer and  $2\ \mu\text{m}$  buried oxide layer and are patterned using I-line stepper lithography. The mechanical devices are released using a timed buffered oxide etch which releases the mechanical beams without releasing the  $430\ \text{nm}$  wide waveguides.

In figure 7.1 the red (left) and green (right) optical racetrack resonators are designed using identical dimensions but due to fabrication variations their optical resonance wavelengths are slightly different. This is also true regarding the mechanical frequencies of the beams. The DC transmission scan for the combined system is plotted in figure 7.2 (a). It can be thought of as two individual optical resonances that overlap as illustrated in figure 7.2 (b). Further separation of the optical resonance frequencies of the cavities could be achieved with device design changes. Each individual double clamped beam will only modulate the optical resonance of its respective optical racetrack.

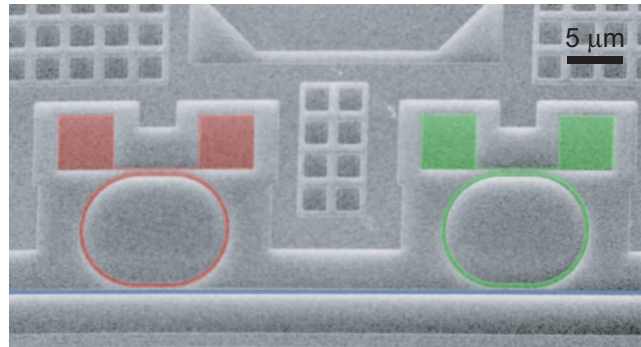


Figure 7.1: Colorized SEM of a multiplex readout NOMS system. Two separate racetrack resonator NOMS devices are fabricated on the same waveguide bus. The different optical resonance frequencies of each cavity allow the separate mechanical beams to be probed individually at their respective cavity wavelength.

### 7.3 Wavelength-division multiplexing measurements

To test the WDM properties of the two device set the probe wavelength is scanned while monitoring the thermomechanical noise frequency response of the devices. In the experiment the devices are placed under vacuum and measured using a Zurich lock-in amplifier with a measurement bandwidth of 200 Hz with 4 times averaging. The probe wavelength is set at different carrier channels of 1550.4 nm, 1550.7 nm, 1551.5 nm and 1552.0 nm. These correspond to the side of one optical resonance, bottom of the resonance, the middle peak between the two resonances and side of the second resonance, respectively, as can be seen in figure 7.2 (a). The response of the multiplexed device for these different probe wavelength channels is shown in figure 7.3. As the slope of the DC optical transmission curve at 1550.7 nm is 0 no signal is expected, and this signal is offset by  $-10$  nW to be seen on the plot.

The property of the overlapping optical resonance frequencies allow the device to pick up both mechanical signals at the same probe wavelength. This demon-

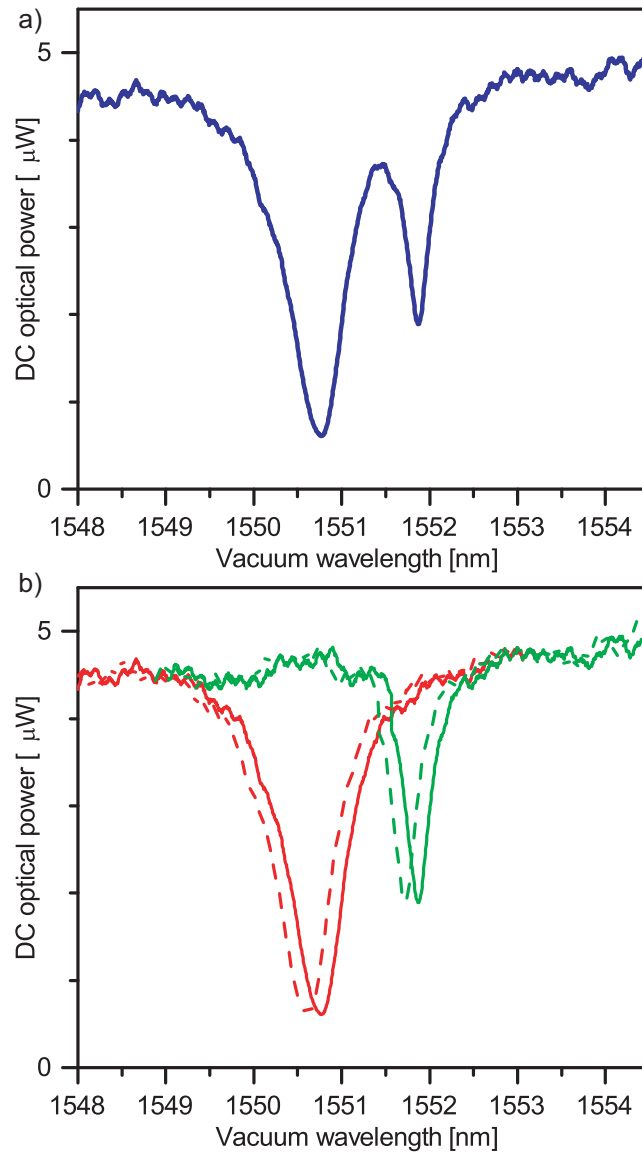


Figure 7.2: (a) DC optical transmission spectrum of a multiplexed racetrack resonator nanomechanical beam transducer system. (b) Conceptual scan of the two individual racetrack resonances and the hypothetical shift of each due to its respective doubly clamped beam resonator.

strates the potential of multiplexing different devices using the same optical cavity. Several devices on the same nanophotonic transducer would decrease

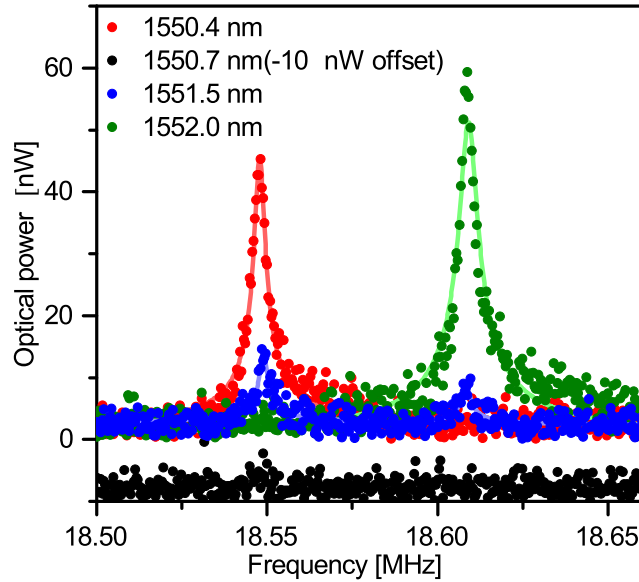


Figure 7.3: The thermomechanical noise response of a two device multiplex system while probed at different wavelength channels. As the probe wavelength increases the signal shifts from one mechanical resonance to the next. The overlap of the two optical resonances allow a single wavelength to probe the mechanical beams on both racetracks simultaneously.

the complexity further, and still avoid the potential power losses generated when measuring large numbers of devices using scattering. This owes to the phase detection mechanism as described in previous chapters. If operating in a mass sensor application, however, the frequency of these devices would need to be individually tracked. With a single cavity detection scheme there is no way to differentiate between devices except by using their mechanical resonance so the mechanical resonances would need to be designed sufficiently different from one another. Care would also be needed to track the changing frequencies to ensure a mass loading event does not cause one frequency to shift passed another thereby creating the potential to mix the two devices up. This especially important if the multiplex devices are functionalized differently and respond to different analytes.

## 7.4 Determining the probe channel of individual nanomechanical resonators

Wavelength-division multiplexed NOMS allow a set probe wavelength to differentiate between different mechanical devices as opposed to using their varying mechanical frequencies. With careful design and fabrication the wavelength channels for each device can be determined using the designed optical resonance of the device cavities. This can also be experimentally determined by monitoring the mechanical frequency of a device while locally changing its mechanical properties. The frequency shift will corroborate which wavelength probe frequency corresponds to each probe wavelength.

To reversibly change the mechanical properties of the doubly clamped beams a 0.5 mW 1064 nm laser is focused onto the substrate surface with 150  $\mu\text{m}$  beam diameter. The heat from the laser changes the optical ring resonances so the measurement is taken after the optical frequency has stabilized. Taking advantage of the overlapping optical cavity frequencies the probe wavelength is tuned so the magnitude of the mechanical response for each device is approximately equal. As above, this allows the mechanical frequency of both devices to be monitored simultaneously. To eliminate any heating caused by the probe laser its power is decreased by 3 times compared to the channel scanning experiment. The mechanical devices are driven using a shear-mode piezoelectric crystal to account for the lower transduction power. Both the devices are driven and detected using a HP 8752C network analyzer.

The heating laser is manually scanned across the multiplex device while monitoring the mechanical frequencies of both doubly clamped beams. As the heating laser is aimed preferentially to the left device in figure 7.1 the lower mechanical frequency, as independently measured with a 1550.4 nm wavelength probe, decreases which corresponds to the spring constant of the beam softening due to heating. Conversely while targeting the right side device the higher mechanical frequency decreases while the other frequency remains con-

stant. This is shown in figure 7.4. This experimentally matches the 1550.4 nm probe channel device to the left-most doubly clamped beam with a mechanical frequency of 18.55 MHz, and also the 1552.0 nm probe channel device to the right-most doubly clamped beam with a frequency of 18.615 MHz.

## 7.5 Conclusion

Wavelength-division multiplexing is demonstrated for a set of two doubly clamped beam resonators using nanophotonic transduction. Two racetrack resonator optical cavities are implemented along the same input and output waveguide in an all pass configuration, and each racetrack is coupled to its own adjacent nanomechanical doubly clamped beam resonator. The two optical cavities are designed to be identical, but due to fabrication variations their optical resonances are separated but overlap at their tails.

The probe wavelength is scanned across the two optical cavities and the frequency response of the thermomechanical noise of the doubly clamped beams is monitored. As the probe wavelength changes from one cavity to the next the mechanical frequency of each doubly clamped beam is measured. The beams can be measured independently if the probe wavelength sits on only a single optical resonance or they can be measured simultaneously if the probe is set to the overlapping region. The independent frequency measurements at different wavelengths verify wavelength-division multiplexing.

Finally, to experimentally determine which probe wavelength detection channel corresponds to each physical nanomechanical beam a heating laser is used to preferentially heat each device. A single probe wavelength is used to measure both devices simultaneously. The heating causes a downward shift in the mechanical frequency of each device and both shifts are detected individually. Knowing the wavelength channel for each independent mechanical resonator would allow for individual beams to be functionalized differently and detected simultaneously.

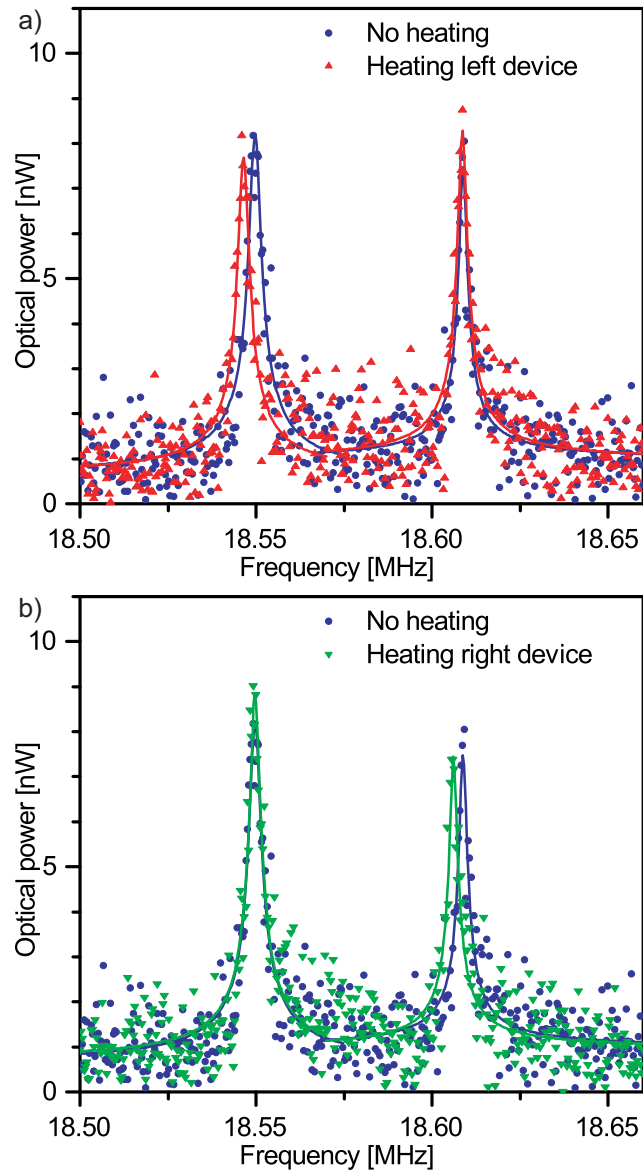


Figure 7.4: The simultaneous monitoring of both mechanical frequencies while the device is not heated (blue circles), the left device in figure 7.1 is heated (red triangles) (a) and the right device is heated (green inverted triangles) (b). The laser heating causes a reversible softening in the mechanical frequency. The measurements are taken with 300 Hz BW and 4 times averaging.

Multiplexing offers a possible solution to the capture area problem posed by nanomechanical beam sensors. Hundreds of devices can be implemented onto a single chip and detected with minimal complication due to the single input and output for the signals. Using optical cavity based nanophotonic detection allows for wavelength-division multiplexing where multiple signals are present simultaneously on the same waveguide bus. As the detection method is based on phase interactions as opposed to scattering effects the signal will not degrade with each additional device. Not only do nanophotonic systems offer excellent transduction properties of nanomechanical resonators, but they are also well suited for detecting multiplexed arrays.

---

---

## CHAPTER 8

---

# Device overshield for mass sensing enhancement (DOME)

### 8.1 Introduction

Two issues of concern arise with the prospect of nanomechanical beam mass sensing using nanophotonic detection. The first issue applies to resonating beam mass sensors as a whole and follows from the mechanical frequency shift dependence on the analyte mass' position on the beam (as discussed in chapter 2). Since there is generally little control of where the analyte will exactly land on the beam there is ambiguity in the amount of mass added if only the resonant frequency shift of a single mode is measured [19]. One solution to this problem is to measure the frequency shift of multiple multiple modes of the beam. A system of equations can be solved that equates the different frequency shifts from different modes (caused by their differing mode shapes imparting different amounts of energy) to give both the mass and position of the particle with no prior knowledge [32, 33, 21, 20]. This solution works very well if multiple beam modes can be detect.

A second issue specific to nanophotonic detection is the risk of analyte material disrupting the transduction system through deposition on the integrated

photonic components. For instance, foreign material deposited on a waveguide's surface could disrupt the propagation mode and create a scattering site. This could spoil the waveguide's ability to guide light, and, more importantly, if this occurs in an optical cavity the scattering site would drastically reduce the cavity's optical finesse and therefore the transduction ability [124, 87].

To address these issues the device overshield for mass sensing enhancement (DOME) structure has been developed using materials compatible with nanophotonic structures. It addresses the analyte deposition location issue by creating an integrated shadow mask, or nanostencil, which only allows analyte material to physically deposit on specified areas of the beam. This gives the additional advantage of targeting mass loading locations only to the areas giving the greatest frequency shifts to ensure the smallest possible masses are detectable during a loading event. It would also address the potential nanophotonic scattering issue by physically protecting the nanophotonic components with this same overshield layer. This chapter follows from the work in reference [109].

## 8.2 DOME structure fabrication

The DOME structure process flow is developed for simple integration with existing nanomechanical resonator fabrication techniques. It uses surface micromachining processes which are typical in many clean room facilities [125, 126]. It is assumed that the nanomechanical devices are fabricated from a silicon on insulator (SOI) wafer in which the silicon device layer is patterned on top of a sacrificial buried oxide (BOx) layer. The DOME fabrication process begins after the nanomechanical devices have been patterned and etched but before the sacrificial oxide layer has been etched away and the nanomechanical devices released. A full process flow is shown in figure 8.1.

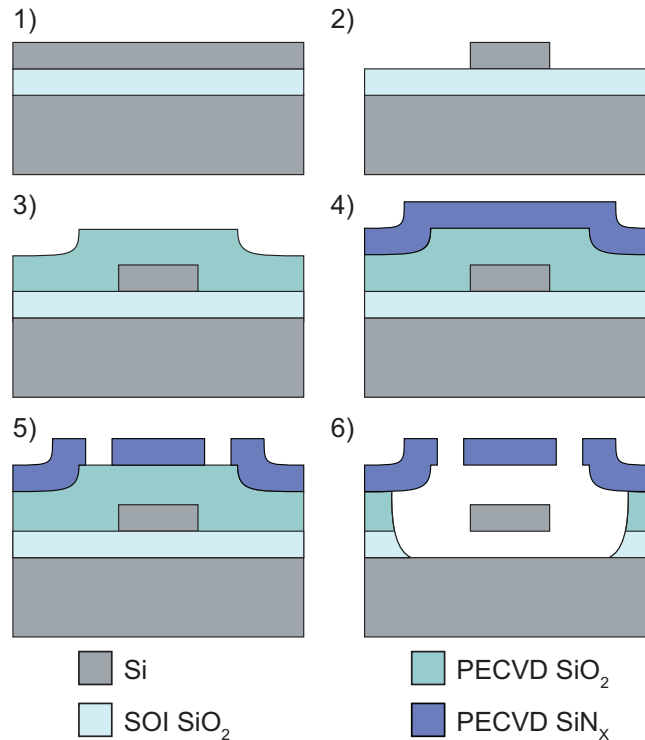


Figure 8.1: DOME structure fabrication process flow. 1-2) Pattern nanomechanical structure, 3) PECVD deposition of  $\text{SiO}_2$ , 4) PECVD deposition of  $\text{SiN}_x$ , 5) Patterning and RIE of  $\text{SiN}_x$ , 6) Release of nanomechanical resonator with BOE followed by critical point dry. Adapted from [109]. Copyright 2010 IOP Publishing Ltd.

Instead of the nanomechanical beam release step a structural silicon dioxide layer is deposited onto the sample using plasma enhanced chemical vapor deposition (PECVD). The thickness of the  $\text{SiO}_2$  is chosen to be approximately two times the thickness of the silicon device layer to ensure adequate spacing for the nanomechanical beam to resonate. In the experiment, SOI wafers with a 147 nm Si/136 nm  $\text{BOx}$  layer and 110 nm Si/134 nm  $\text{BOx}$  are used. With both of these device sets the oxide structural layer deposited is approximately 305 nm thick.

The deposited oxide layer is both a support layer and a sacrificial layer for the DOME device. The structural layer holds the nanostencil portion of the

DOME above the nanomechanical beam so the beam can freely oscillate without contacting the nanostencil. To freely oscillate, however, the structural layer must also be etched as a sacrificial layer above the silicon device layer. For this reason  $\text{SiO}_2$  is chosen as it has excellent isotropic etch selectivity against the silicon device layer using a buffered oxide etch (BOE) [127].  $\text{SiO}_2$  also has desirable electrical and optical properties. A DOME structure could be implemented with an electrical transduction scheme since no short circuits would be created as  $\text{SiO}_2$  layers are used to isolate metal interconnects on CMOS devices. It could also be implemented with a nanophotonic transduction scheme as  $\text{SiO}_2$  is already used in integrated photonic cladding layers.

The next step is to create the nanostencil layer. Silicon nitride ( $\text{SiN}_x$ ) is chosen for its mechanical, optical, electrical and chemical properties. PECVD is used to deposit 250 nm of  $\text{SiN}_x$  on top of the structural oxide layer. This thickness is chosen since it gives good structural stability. The mechanical properties for the nanostencil layer must be quite strong to avoid failures caused by external stresses of deposited film. Silicon nitride is a good choice for this as evident in its use for creating membrane structures. The optical properties allow for its compatibility with free space optical transduction and actuation [128] since it is transparent in the visible spectrum often used for these experiments. It has also been shown to be a practical material for use in nanophotonic devices [66]. A dielectric constant of about 6-9 [129] will not cause any adverse effects if implemented with an electrical detection or actuation system, as well. Finally,  $\text{SiN}_x$  could not be used in the structure if not for its etch resistance against BOE. This chemical property makes it compatible with the process step of etching the sacrificial oxide layers to release the nanomechanical resonator [127].

After depositing the overshield layer it is then patterned to define the mass loading location above the mechanical resonator. Holes are also patterned above the area adjacent to the resonator to allow access for BOE to facilitate a faster etch release step. Electron beam lithography is used to pattern the overshield layer primarily for its direct write characteristic. Depending on the

resolution of the nanostencil holes other forms of lithography may be used. ZEP520A about 410 nm thick is used as the resist; chosen for its etch resistance. To prevent charging during the EBL write an approximately 7 nm thin layer of aluminum is sputtered onto the sample after resist deposition. After exposure, and prior to EBL development, the Al layer is removed using CD-26 developer for 1 min.

After patterning, the  $\text{SiN}_x$  is etched using a reactive ion etch (RIE). An RIE is chosen to maintain resolution of the patterning by using an anisotropic etch. Care must be taken in the overshield design as it itself could act as a released resonating structure. This is especially true if using a non-specific actuation method such mounting the sample to a piezoelectric chip. To avoid false signals it is important to design any potential overshield resonance modes at a much different frequencies than the nanomechanical beam modes. After the RIE the resist is ashed away using an oxygen plasma.

The final step for creating the DOME structure is the release of the nanomechanical resonator. This is done using a single-step, timed, isotropic buffered oxide etch. As mentioned above the BOE selectively etches the  $\text{SiO}_2$  over the silicon device and the  $\text{SiN}_x$  overshield layer to remove the oxide surrounding the nanomechanical beam to allow it to freely vibrate. To avoid any stiction issues from either the mechanical resonator or the overshield the device is critically point dried. Devices fabricated were 250 nm wide, 147 nm or 110 nm thick with lengths 8  $\mu\text{m}$  to 14  $\mu\text{m}$ . The nanostencil openings were placed at 10% to 90% intervals along the beam length and were 600 nm wide. An exploded view of the structure is shown in figure 8.2.

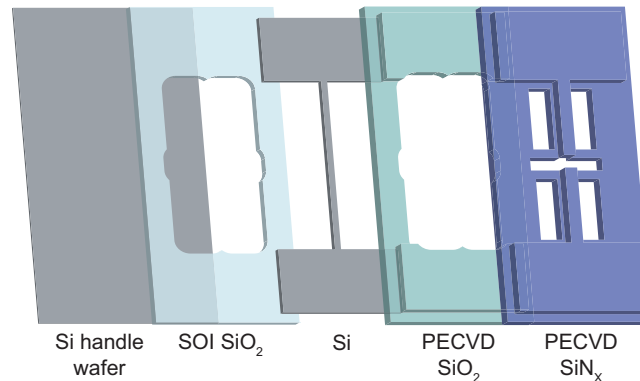


Figure 8.2: Dome structure exploded view. The four vertical holes in the  $\text{SiN}_x$  layer are the access holes for the BOE, and the horizontal hole is to allow analyte through to the beam. Adapted from [109]. Copyright 2010 IOP Publishing Ltd.

### 8.3 Characterization

The DOME structures are characterized by both visual inspection and also by looking at the mechanical quality factor of the nanomechanical beams. Scanning electron micrographs (SEMs) of typical fabricated devices are shown in figure 8.3. The image shows the overshield successfully suspended above the nanomechanical resonator with slit locations above various beam locations. At first glance the overshield appears to sag and collapse onto the beam, but on closer inspection it can be seen that overshield near the beam clamping points is raised based on the contours of the nitride around the slit. These cracking defects are caused by the compressive stress in the deposited PECVD  $\text{SiN}_x$  in addition to extra stress caused by the topography step of the patterned beam. As the film expands on either side of this height-discontinuity the stress is relieved by the cracking and the buckling upward at the anchors. Other than these cracks the rest of the overshield remains intact. As a result the cracks are not a concern as they do not propagate above the resonator to form gaps in the overshield directly over the beam which would thereby create another mass loading location.

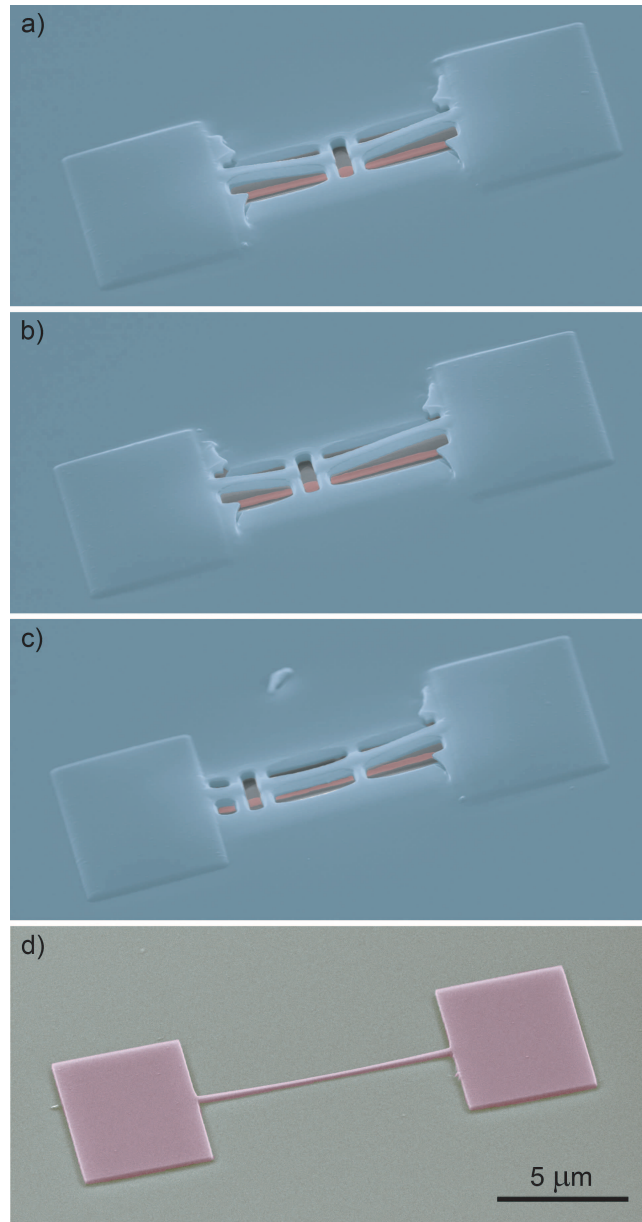


Figure 8.3: SEM of fabricated DOME structure over top of a 10  $\mu\text{m}$  long, 250 nm wide and 110 nm thick nanomechanical beam (pink) with a DOME structure (blue) on top with slit locations along the beam at (a) 50% (b) 30% and (c) 10% of its length. (d) 8  $\mu\text{m}$  long resonator fabricated without the DOME structure. Approximately 5 nm of Cr is deposited onto the DOME devices to prevent charge build-up from the SEM beam.

The second characterization technique investigates the effect the fabrication of the overshield has on the mechanical response of the resonator. This is most important as the mechanical response will determine the effectiveness of the device as a mass sensor. One way to characterize the mechanical response is to look at the mechanical quality factor (Q-factor). This describes the damping and amount of losses the nanomechanical resonator is subjected to during oscillation and is briefly described in section 2.4.2. The Q-factors of devices fabricated with and without the overshield are compared to look for detrimental effects causing a much lower Q.

The mechanical response of the beams was measured using a simple single beam interferometry setup with a 633 nm laser [82, 3]. The devices are actuated by mounting the sample chip to a piezoelectric disk and applying a signal to the disk using a network analyzer. The network analyzer is also used to detect the interference signal reflected off the chip and onto a photodiode. Measurements were taken at room temperature and below  $1 \times 10^{-5}$  Torr. The Q-factor is extracted by fitting the response to a Lorentzian fit. The resolution bandwidth of the measurement was set to 1 kHz to allow for timely data acquisition while limiting systematic error introduced into the measured Q values. Due to the finite measurement bandwidth used the measured Q-values are underestimated by approximately 10% to 20% with values of about 5000 to 10000, respectively. The smallest fabricated devices (8  $\mu\text{m}$  long, 250 nm wide and 110 nm thick) have Q-factors around 6000 which are acceptable for a top down fabricated device under these measurement conditions. A typical response is shown in figure 8.4.

As expected, the location of the mass loading slit has little effect on either the Q-factors or the resonant frequencies of the devices. This is shown in table 8.1 for two sets of 8  $\mu\text{m}$  long, 250 nm wide and 110 nm thick devices with overshield slits at different locations along the beam length. For comparison data from devices without overshields is also included. To ensure a valid control sample against the DOME structure fabrication process the non-overshield devices were fabricated on separate samples without any of the extra fabrication steps.

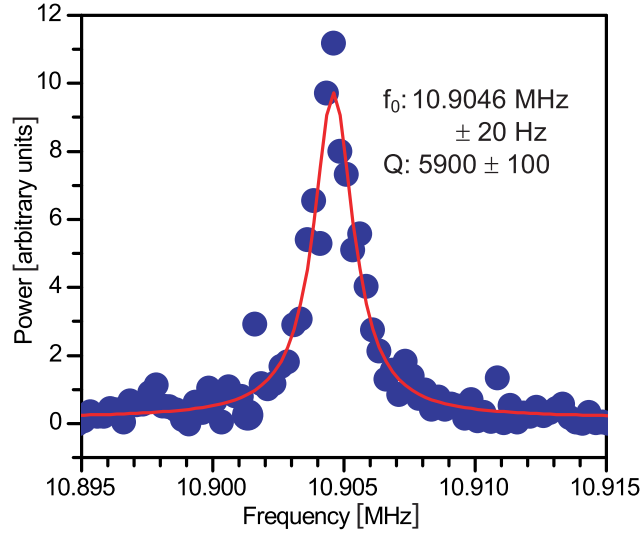


Figure 8.4: A typical response of an 8  $\mu\text{m}$  long, 250 nm wide and 110 nm thick doubly-clamped beam with a DOME structure over top. The diameter of the dots represent the error due to the 1 kHz measurement bandwidth. The red line is the Lorentzian fit from which the resonant frequency and Q-factors are extracted from. Adapted from [109]. Copyright 2010 IOP Publishing Ltd.

The non-overshield structures exhibit higher mechanical frequencies which is due to their smaller undercut. This could also contribute to their slightly higher Q-factors since a more precise undercut contributes to smaller clamping losses. Figure 8.5 plots the Q-factor data devices with various slit location along with the devices with no DOME structure. The average of the two data sets are within range suggesting there is not any significant degradation of the mechanical response due to the DOME structure fabrication process.

Finally, to test the nanostencil functionality of the DOME structure in blocking incoming masses approximately 23 nm of  $\text{Al}_2\text{O}_3$  is deposited onto the sample using evaporation. Evaporation is used to simulate collimated methods of mass loading [19, 22, 23, 24, 88]. A stictioned nanomechanical resonator is used for the deposition. As seen in figure 8.6 the overshield only allows the deposited material to land on the targeted area of the beam. A sharp transition can be seen between the covered and uncovered areas.

Table 8.1: 8  $\mu\text{m}$  long, 250 nm wide and 110 nm thick doubly-clamped beam response. Device Set A and B are identical series of devices fabricated on the same chip. The devices without overshields are fabricated on a different sample with resonators identical to those on the DOME devices. The higher frequency of these resonators is caused by the smaller undercut during BOE release.

Slit location (% of length from anchor)	Device set A		Device set B		Devices without overshields	
	$f_0$ (MHz)	Q-factor	$f_0$ (MHz)	Q-factor	$f_0$ (MHz)	Q-factor
10	10.71	5000 $\pm$ 300	10.90	5900 $\pm$ 100	11.88	12000 $\pm$ 1000
20	10.55	5200 $\pm$ 300	10.67	6000 $\pm$ 100	11.98	5100 $\pm$ 700
30	10.63	6300 $\pm$ 200	10.80	6300 $\pm$ 300	11.75	8000 $\pm$ 1000
40	-	-	10.74	7500 $\pm$ 400	11.94	7000 $\pm$ 1000
50	10.88	9000 $\pm$ 400	10.75	6100 $\pm$ 400	12.00	6300 $\pm$ 400
50	10.76	6430 $\pm$ 70	10.90	11000 $\pm$ 1000	11.88	5300 $\pm$ 600
60	10.91	6300 $\pm$ 100	10.67	4500 $\pm$ 200	11.74	7500 $\pm$ 500
70	10.73	5500 $\pm$ 100	10.92	5600 $\pm$ 100	11.88	13000 $\pm$ 2000
80	10.74	5500 $\pm$ 200	10.69	5000 $\pm$ 200	11.96	11000 $\pm$ 1000
90	10.73	5300 $\pm$ 100	10.79	5700 $\pm$ 100		

## 8.4 Discussion

The DOME structures are fabricated on top of doubly-clamped beam resonators to reduce the risk of stiction during fabrication. Due to a lower effective stiffness cantilevers are more susceptible to stiction, but the DOME structure fabrication process should work with cantilever devices as well. Cantilevers have some advantages over doubly clamped beams in that their mode shape gives them a lower effective mass factor by about a third which, all other things being equal, would lead to increased mass resolution. The dynamic range of an oscillating cantilever is also larger than that of a doubly clamped beam which also leads to higher sensitivity [18, 90, 130]. However, cantilever devices are at a disadvantage in that they cannot be put under tensile stress to form strings with high mechanical Q-factors. In a nanomechanical mass sensor either type might be best suited for the specific application so it is important that the fabrication of the DOME structure be compatible with both types.

There are many advantages to the fabrication process including its simplicity,

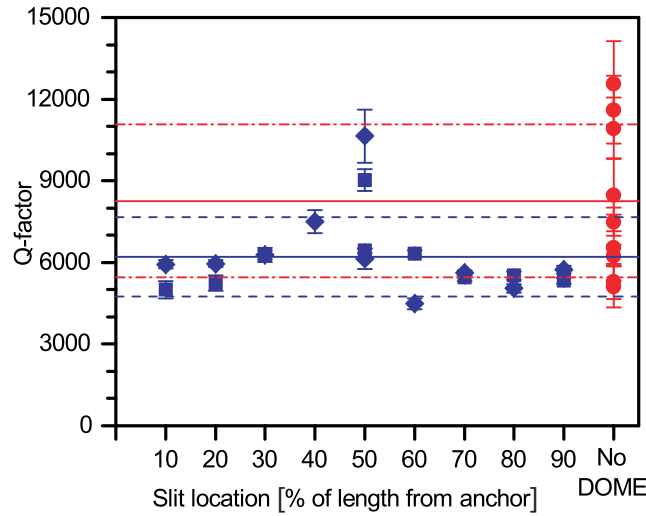


Figure 8.5: Q-factors of  $8\ \mu\text{m}$  long,  $250\ \text{nm}$  wide and  $110\ \text{nm}$  thick doubly-clamped beam resonators with DOME structures having various mass loading slit locations. The blue diamonds and squares represent different sets of similar devices. The blue solid line is the average value of the diamond and square data with the blue dash at the first standard of deviation, and the red solid line is the average Q-factor value of the devices fabricated without DOME structures with the red dash/dot line representing the standard of deviation. Adapted from [109]. Copyright 2010 IOP Publishing Ltd.

the temperature tolerance and its compatibility with various nanomechanical excitation and transduction methods. The single extra patterning step and two extra deposition layers lead to fairly straightforward troubleshooting options if any problems arise while fabricating upon different sample types. The single BOE step is also beneficial in that only the single critical point dry step is required to avoid stiction problems. The high thermal budgets for  $\text{SiO}_2$  and  $\text{SiN}_x$  allow for compatibility with high temperature processes like annealing, sample flashing or high temperature deposition methods, which could be required for fabricating complete device systems. The high temperature processes would still need to be tested but should be compatible due to the chosen materials. Since a variety of methods are currently used for nanomechanical transduction it is very beneficial that the process is compatible with most of

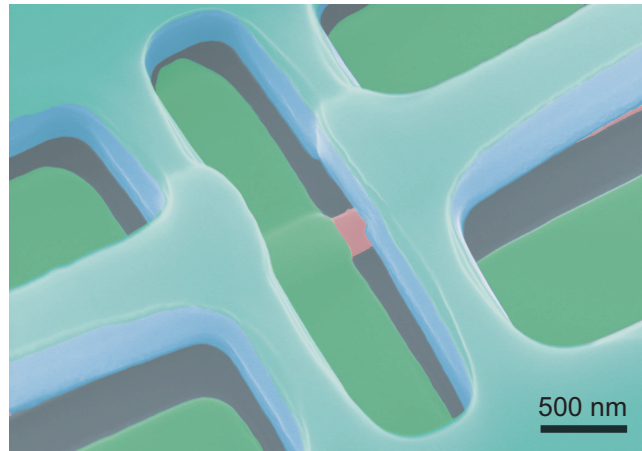


Figure 8.6: Colorized SEM of about 23 nm of  $\text{Al}_2\text{O}_3$  evaporated onto a DOME device. The beam (pink) is shielded from the deposited material (green) by the nanostencil (blue), except at the designed slit areas above the beam. Approximately 5 nm of Cr is deposited onto the DOME devices to prevent charge build-up from the SEM beam. Adapted from [109]. Copyright 2010 IOP Publishing Ltd.

them.

Although the cracks did not affect the operation of the DOME structure it would still be desirable to eliminate them. There are a few possibilities to remove these cracks caused by stress in the film near the topography discontinuities. As they are caused by stress in the  $\text{SiN}_x$  layer the stress could be removed with an annealing step after deposition. Alternatively a lower stress overshield layer could be deposited in the first place using a material such as low stress low pressure chemical vapor deposition (LPCVD)  $\text{SiN}_x$  or  $\text{SiCN}$  [131]. Another option would be to planarize the structural oxide layer to remove the topographical defects. While fabricating the devices these extra steps were avoided in the interest of process simplicity especially since the cracks did not affect device operation.

The stress in the deposited PECVD layers does not significantly alter the resonance characteristics of the nanomechanical beams as is witnessed in comparing the mechanical quality factors of devices fabricated with and without

overshields. This is a plausible result as the films are only in contact with the device on the device anchors after fabrication is complete. It is possible that residual stress exists on the resonator. If present, the stress caused by the compressive stress deposited films would cause a tensile stress on the resonator which could in fact increase the device performance [132].

A drawback to mass loading onto a DOME structure is the decreased capture efficiency caused by blocking most of the mechanical beam area. Here, the capture efficiency is defined by the analyte detected to the analyte used. This will cause potential data to be lost and time will also increase between mass loading events. If only a single mode of the beam is detected, however, the DOME structure will eliminate the ambiguity of the frequency shift caused by loading mass at different beam locations. The data collected will also will represent the device operating at only its highest responsivity so capture efficiency and data quantity are sacrificed in favor of higher data quality. The final sensing application will determine whether a decreased complexity in the device measurement is required (using a DOME structure) or whether a device is desired with maximum capture efficiency.

Finally, the nanostencil functionality of the structure lends its use toward accurately depositing materials onto released nanomechanical resonators without any intricate alignment mechanisms. External shadow masks have been used for targeted depositions onto released MEMS structures, but the method created an array of patterned material on and around the MEMS structure with no concern over the exact pattern location [133]. Targeted deposition has been realized but included the use of high resolution stages which could both be expensive and complicated to implement [134]. Targeted deposition could be used to deposit catalyst materials onto a nanomechanical beam for targeted carbon nanotube [135] or silicon nanowire [136] growth. The catalyst (i.e. Ni or Fe for SNT growth) is typically attacked by the BOE during the resonator release or otherwise it could be washed away if there is poor catalyst adhesion (i.e. Au for Si nanowire growth). Nanowire or nanotubes could greatly increase the surface area of the beam where they are deposited, and

could therefore be used to create more responsive sensors where surface area adsorption is important.

## 8.5 Conclusion

Device overshield for mass sensing enhancement (DOME) structures were fabricated and developed to overcome the issues of maximizing nanomechanical mass sensor responsivity for a loading event, as well as determining the exact location of mass loading for definitively determining the magnitude of the added mass. Standard fabrication processes were used to achieve this through an integrated nanostencil design which operates as a shadow mask directly above the nanomechanical resonator. The materials of the DOME structure process allow for many different options for nanomechanical beam actuation and detection such as optical, electrical and nanophotonic methods.

The DOME structure is not found to have a significant effect on the mechanical resonator's frequency response. Nanostencil operation is successfully demonstrated with the deposition of evaporated material onto specific beam locations. The structures could help achieve the goal of nanomechanical sub-Dalton measurement devices by offering a way to protect the nanomechanical device and its transduction components while decreasing the complexity of the mass readout analysis.

---

---

## CHAPTER 9

---

### Future Work

#### 9.1 Introduction

The work in this thesis explores much of the groundwork for using nanophotonic transduction in a nanomechanical mass sensor. This groundwork includes transducing cantilever structures that are not limited to a minimum size compared to previous NOMS designs. Also, the transduction mechanisms are investigated to gain a better understanding of which nanophotonic optical properties will lead to the best signal transduction. A nanophotonic friendly fabrication process is also developed to prevent waveguides from suffering scattering losses when mass is deposited on top of them. To pursue the ultimate sub-Dalton mass sensitivity goal many design options may be required, such as using cantilevers or doubly clamped beams, and this work demonstrates that more of these options are available. In addition the focus was on creating devices that could easily translate into practical devices. As such the devices were always fabricated with large scale integrable methods such as stepper lithography along top down fabrication processes, and measurements were completed at room temperature with studies toward using them at atmospheric pressure as well.

Although much of the groundwork has been laid these devices still need to

be demonstrated in a definitive mass sensing system. The superior transduction properties of the nanophotonic method have been demonstrated, but that demonstration has not seen much extension into low level mass detection analysis. Future work would look directly along these lines at the practical limitations and operating conditions of a nanomechanical mass sensor using nanophotonic readout.

## 9.2 Basic mass measurements

The most obvious next step is measuring the mass of an analyte particle by measuring the frequency shift of a nanomechanical mass sensor. On a short term basis the nanomechanical resonant frequency of a beam is fairly stable, but it can easily see minor shifts when exposed to atmospheric conditions over a period of time. To measure small additions of mass, then, real-time in-situ measurements would need to take place so the frequency shift can be directly attributed to the analyte mass as opposed to uncontrollable contaminant mass which could occur while removing the sample from vacuum to place in a secondary deposition chamber. Consequently the experimental design must be modified to facilitate this mass deposition.

The simplest method for achieving this goal is simply to bleed analyte gas into the vacuum chamber and look for the frequency shift of the mechanical beam with the added gas. The majority of the initial experiments took place under high vacuum,  $1 \times 10^{-5}$  Torr, but this vacuum may be too high to allow the analyte gas to adsorb onto the sample surface in a time that is detectable by the system. At atmosphere, however, the noise on the signal may be too high to resolve a frequency shift of small additional masses. A pressure in between these levels, such as about 1 Torr, may be a good place to start. The mechanical damping on the device would still be minimal to allow for good mechanical signal transduction, but the gas pressure would allow the analyte gas more time to interact with the device instead of being immediately pumped away.

Discrete frequency changes could be detected which correspond to individual gas molecules adsorbing onto the nanomechanical device. This frequency shift would vary depending on where the analyte adsorbs onto the nanomechanical beam so statistics would need to be used to determine the added mass amount [19]. Another option would be to monitor two mechanical modes simultaneously to give a definitive mass and position information at the same time [32, 33, 21, 20]. A second possibility is a constant frequency shift at equilibrium could be measured depending on the adsorption/desorption time and the amount of analyte gas in the system. This equilibrium shift would correspond to the rate of adsorption/desorption such that a total equilibrium amount of analyte particles would be present on the nanomechanical device after a set amount of time. This type of study could both give both gas kinetic and mass information on the analyte.

The biggest assumption in this type of study is the analyte material has a minimal effect on the nanophotonic components of the device. Nanophotonic rings are used themselves as sensors, but are more adept at detecting layers as opposed to point particles [119]. An optical frequency shift caused by the analyte material will have an effect on the sensor in that it will change the most efficient probe laser frequency. This will reduce the nanomechanical signal but will only be a problem if the shift is so large the signal is lost completely. Since minimal amounts of analyte material are added this optical shift is not expected to be large enough to cause this complete signal loss. This also assumes that the analyte does not cause irreparable signal losses in the integrated optical system. This could occur if a lossy material such as a metal is deposited on the device. The photon energy would be lost to plasmonic modes of the metal which could destroy the optical throughput of the devices. To avoid these potential losses the same type of measurements could be completed but with an implemented DOME structure.

### 9.3 Nanophotonic DOME integration

The DOME structure utilizes dielectric materials in its fabrication, both of which are used in integrated photonics, so no problems are anticipated for its integration. That being said, the DOME device should be fabricated on top of nanophotonically transduced nanomechanical beams for further mass loading tests and analysis. To do this the DOME fabrication steps would be completed after the nanophotonic chip is patterned and etched, but prior to the mask-less BOE release.

Testing will need to be done to determine the exact characteristics of the fabricated overshield. This includes the height of the silicon nitride nanostencil over the nanophotonic waveguide as determined by the deposited silicon dioxide sacrificial structural layer thickness. The amount of this structural oxide layer around the waveguide can also be modified depending on its influence on the propagating mode. For instance, it could be chosen to keep this oxide around the waveguide as a cladding layer or it could be removed completely, and both these options could be explored to achieve optimal integration.

To explore these options it would be pertinent to first simulate the expected results using finite difference time domain (FDTD) simulations. The main metric for these simulations would be to examine the effective index versus the gap distance between the nanophotonic waveguide and the nanomechanical resonator. The rate of change of this value relates directly to the transduction coefficient so it is important to verify that the slope of this curve remains approximately the same with the DOME integrated configuration. From here it is only a matter of fabricating the devices within tolerance of these results. Process flow improvements could also be tested to reduce stress in the nanostencil layer to remove the cosmetic cracking that was previously observed.

## 9.4 Advanced mass detection

Once the DOME structures are successfully integrated with the NOMS resonating beams, advanced level mass detection experiments can take place. Here, advanced level mass detection refers to two specific cases. One, the real-time measurement of single low mass particles, or, two, the detection of optically lossy materials which traditional nanophotonic methods cannot detect. Both types of experiments simulate the advanced application of the device as a state-of-the-art mass sensor aspiring to proton level sensitivity in a smaller, inexpensive package.

In the first case the DOME structure is used to converge the frequency shift range for the added masses by limiting the mass deposition location on the nanomechanical beam. It also protects the waveguide from the added material either shifting the optical resonance conditions, so maximum transduction is maintained, or by creating scattering losses along the length of the waveguide. For highest sensitivity the measurements may need to take place in vacuum so another experimental setup design change may be required.

Instead of leaking arbitrary gas into the system a more targeted approach to mass deposition would be required. This can be achieved by depositing analyte onto the nanomechanical beams using a more kinetic, instead of diffusive, mechanism. The vacuum system design with the optical window allows for laser deposition methods to be easily implemented into the chamber. One such method is using matrix assisted laser desorption and ionization (MALDI). MALDI is a traditional mass spectrometry technique to apply charges to fragile analyte materials. The analyte is embedded in a host chemical crystal matrix which is then irradiated with an ultra-violet or infrared laser to expel the particles into the gas phase with little damage [137]. The MALDI matrix could be implemented within the vacuum chamber with the sample irradiated through the optical window to launch analyte particles toward the sample. The nanomechanical beams could be measured in real-time to mark the deposition events. An added advantage to this system is the neutral parti-

cles of the MALDI expulsion method could be investigated as nanomechanical mass measurement is charge independent. This potentially new information on the MALDI expulsion process could allow for better implementation of the technology as it is currently used.

The optical window allows for other laser based deposition methods to be studied as well. One such method is laser induced forward transfer (LIFT). Applying this method would both study this laser deposition process as well as demonstrate the practical implementation of the DOME structure on a mass sensor. LIFT is traditionally an experimental microscale deposition and patterning technique based on laser direct write addition. A transparent donor substrate is coated with the material to be deposited and a laser irradiates this material from the backside of the substrate to expel the deposited material off the front side through laser ablation [138]. Exact mechanisms of the process are still under study and these NOMS devices could be used to directly measure the amount of material transferred under differing laser conditions. Currently characterization is achieved through imaging techniques such as SEM or AFM where it is difficult to determine exact volumes deposited. A better understanding of the process would lead to better applications.

The DOME implemented NOMS mass sensors would be especially useful in studying the LIFT deposition of metals. As mentioned earlier metals can cause significant losses in optical waveguides due to plasmonic modes in the metal. The photon energy oscillates the electrons in the metal at the plasmon resonance which oscillates with higher losses. The DOME structure would prevent the metal from interacting with the nanophotonic waveguide by keeping the material a sufficient distance away. In this instance the superior transduction properties of a NOMS system could be used without worrying about the limitations a metal analyte may cause.

## 9.5 Conclusion

Mass loading experiments are the next step following the basic studies of this work involving nanophotonic detection of nanomechanical resonators. The potential of using this type of system for measuring point masses is demonstrated due to the effectiveness of transducing smaller and smaller nanomechanical beam resonators. The next steps potentially involve depositing masses in the current experimental system, but opportunities also exist to bring this technology into arbitrary experimental systems as well.

The current experimental setup is ideal for prototype devices due to its flexibility in probing different optical structures. Once an ideal design is fabricated, however, this flexibility may no longer be required and a fixed method of photonic laser input/output may be used. A device with fixed inputs could be easily implemented into an existing deposition setup due to the existence of vacuum fiber optic feedthroughs. With both optical actuation and detection along the same input and output fiber the device could be discretely placed inside any type of experimental chamber to provide mass loading data in other types of experiments. The fundamentals are in place and now it is just a matter of applying these fundamentals in practical applications.

---

## CHAPTER 10

---

### Conclusion

The advent of nanotechnology has seen the development of many novel systems. These range over a variety of different fields from medicine and new cancer fighting methods to resource extraction and hardness and wear coatings. One type of system which has attracted interest is the use of nanomechanical beam resonators to detect particle masses. The potential for this type of device is to replace a large traditional mass spectrometry system with a much smaller and cheaper unit to proliferate the technology and reduce its barrier of access. The traditional table-top system in which users send their samples to the lab could potentially be replaced by a hand held detector which is directly present where it is needed.

The focus of this work is the creation and study of these novel types of nanomechanical sensors for use toward on-chip mass sensing. The largest issue concerning these nanomechanical beams has been transducing their motion. The detection of this motion forms the quantitative basis for mass analysis. The target of increased mass sensitivity is approached using the two main metrics of physical nanomechanical beam size versus the noise in transducing the nanomechanical beam signal. In this work these issues are managed with the transduction of nanomechanical beam motion using nanophotonic structures. Nanophotonic structures are very well suited for detecting smaller and smaller

nanomechanical beams. The reason is two-fold. First, nanomechanical structures tend to increase in frequency as they become smaller due to effective stiffening of the beams. The optical methods of detection and actuation that nanophotonics use are not susceptible to any high frequency limitations that electronic circuits must contend with. Nanophotonics is especially useful over traditional optical techniques as they do not suffer the same size limitations due to diffraction effects. This follows from nanophotonics operating in the optical near-field where diffraction is not a primary concern. Second, nanophotonic systems have the potential to increase their transduction properties with decreasing device sizes. Smaller nanomechanical devices generally have smaller amplitudes of motion which lead to smaller output signals. The smaller range of motion in a nanophotonic system, however, allows the device to increase its signal transduction as the optomechanical coupling can be increased by placing the nanomechanical beam in closer proximity with the nanophotonic element detecting the beam. These properties make nanophotonics a very promising technology for transducing nanomechanical beams for use in mass sensing systems.

To achieve the ultimate goal of a practical nanomechanical device with sub-dalton mass resolution it is important to demonstrate design flexibility and make various tools available for achieving this goal. The approach for this work involved increasing the available tools by transducing the motion of nanomechanical cantilevers using nanophotonic detection methods. Previous methods either studied nanomechanical doubly clamped beams or else cantilevers that had minimum size limitations due to the requirement of the cantilever directly carrying a nanophotonic optical mode. It is important to demonstrate the detection of cantilevers as, all other things being equal, they would have three times higher mass sensitivity compared to a doubly clamped beam since their effective mass factor is three times smaller. The removal of the size limitation on the cantilever is also important as arbitrarily small beams may be required to achieve the mass sensitivity goal. This thesis demonstrated these types of devices and studied the transduction mechanisms as well.

The implementation of these devices into practical sensors is also considered. A drawback of using nanomechanical sensors is that their small size limits the capture area of incoming molecules. However, this can be mitigated using an array of nanomechanical beams which is easy to fabricate using integrated circuit fabrication methods. Integrated photonics is well suited to measuring arrays of NOMS devices and this is demonstrated using wavelength division multiplexing of multiple devices on a single input/output waveguide. Another practical concern is addressed with the development of an integrated protective nanostencil structure. Materials adsorbed onto a waveguide surface could cause losses due to scattering or through unwanted plasmonic modes and an integrated nanostencil would protect the waveguides from interacting with any analyte material at all. It can also be used to maximize the measured frequency shift of a nanomechanical beam by only allowing material to be deposited on the beam location which gives the highest mechanical response. The fabrication process is developed using nanophotonic friendly materials with typical micro and nanofabrication processes.

This thesis lays much groundwork for using nanophotonic detection in nanomechanical mass sensors. It is shown to be a viable method, and the next steps involve implementing the technology to measure various masses directly. The technology looks best suited to measure very small point masses with very small mass thresholds through implementation into a vast array to overcome the small capture area of individual nanomechanical beams. It is hopeful that one day these devices will eventually see application in hand-held mass spectrometry systems. This could allow for mass measurement diagnostic tests to become more accessible, faster and less expensive. This added accessibility to mass spectrometry systems could see them become a standard tool wherever particle analysis is needed.

# Bibliography

- [1] K. Ekinici, X. Huang, M. Roukes, *Appl. Phys. Lett.* **84**, 4469 (2004).
- [2] T. Kouh, D. Karabacak, D. H. Kim, K. L. Ekinici, *Appl. Phys. Lett.* **86**, 013106 (2005).
- [3] D. Karabacak, T. Kouh, K. L. Ekinici, *J. Appl. Phys.* **98**, 124309 (2005).
- [4] K. L. Ekinici, M. L. Roukes, *Rev. Sci. Instrum.* **76**, 061101 (2005).
- [5] M. Li, W. H. P. Pernice, C. Xiong, T. Baehr-Jones, M. Hochberg, H. X. Tang, *Nature* **456**, 480 (2008).
- [6] G. Anetsberger, O. Arcizet, Q. P. Unterreithmeier, R. Rivière, A. Schliesser, E. M. Weig, J. P. Kotthaus, T. J. Kippenberg, *Nat. Phys.* **5**, 909 (2009).
- [7] W. Bogaerts, P. De Heyn, T. Van Vaerenbergh, K. De Vos, S. Kumar Selvaraja, T. Claes, P. Dumon, P. Bienstman, D. Van Thourhout, R. Baets, *Laser Photon. Rev.* **6**, 47 (2012).
- [8] J. Chan, T. P. M. Alegre, A. H. Safavi-Naeini, J. T. Hill, A. Krause, S. Gröblacher, M. Aspelmeyer, O. Painter, *Nature* **478**, 89 (2011).
- [9] E. Verhagen, S. Deléglise, S. Weis, A. Schliesser, T. J. Kippenberg, *Nature* **482**, 63 (2012).
- [10] A. H. Safavi-Naeini, J. Chan, J. T. Hill, T. P. M. Alegre, A. Krause, O. Painter, *Phys. Rev. Lett.* **108**, 033602 (2012).

- [11] A. H. Safavi-Naeini, S. Gröblacher, J. T. Hill, J. Chan, M. Aspelmeyer, O. Painter, *Nature* **500**, 185 (2013).
- [12] J. T. Hill, A. H. Safavi-Naeini, J. Chan, O. Painter, *Nat. Commun.* **3**, 1196 (2012).
- [13] J. Bochmann, A. Vainsencher, D. D. Awschalom, A. N. Cleland, *Nat. Phys.* **9**, 712 (2013).
- [14] X. Sun, X. Zhang, M. Poot, C. Xiong, H. X. Tang, *Appl. Phys. Lett.* **101**, 221116 (2012).
- [15] L. Fan, X. Sun, C. Xiong, C. Schuck, H. X. Tang, *Appl. Phys. Lett.* **102**, 153507 (2013).
- [16] J. Chaste, A. Eichler, J. Moser, G. Ceballos, R. Rurali, A. Bachtold, *Nat. Nanotechnol.* **7**, 301 (2012).
- [17] A. N. Cleland, *New J. Phys.* **7**, 235 (2005).
- [18] K. L. Ekinci, Y. T. Yang, M. L. Roukes, *J. Appl. Phys.* **95**, 2682 (2004).
- [19] A. Naik, M. Hanay, W. Hiebert, X. Feng, M. Roukes, *Nat. Nanotechnol.* **4**, 445 (2009).
- [20] M. S. Hanay, S. Kelber, A. K. Naik, D. Chi, S. Hentz, E. C. Bullard, E. Colinet, L. Duraffourg, M. L. Roukes, *Nat. Nanotechnol.* **7**, 602 (2012).
- [21] S. Schmid, S. r. Dohn, A. Boisen, *Sensors (Basel)*. **10**, 8092 (2010).
- [22] K. Jensen, K. Kim, A. Zettl, *Nat. Nanotechnol.* **3**, 533 (2008).
- [23] H.-Y. Chiu, P. Hung, H. W. C. Postma, M. Bockrath, *Nano Lett.* **8**, 4342 (2008).
- [24] B. Lassagne, D. Garcia-Sanchez, A. Aguiasca, A. Bachtold, *Nano Lett.* **8**, 3735 (2008).

- [25] S. Schmid, M. Kurek, J. Q. Adolphsen, A. Boisen, *Sci. Rep.* **3**, 1288 (2013).
- [26] I. Bargatin, E. B. Myers, J. S. Aldridge, C. Marcoux, P. Brianceau, L. Duraffourg, E. Colinet, S. Hentz, P. Andreucci, M. L. Roukes, *Nano Lett.* **12**, 1269 (2012).
- [27] M. Li, E. B. Myers, H. X. Tang, S. J. Aldridge, H. C. McCaig, J. J. Whiting, R. J. Simonson, N. S. Lewis, M. L. Roukes, *Nano Lett.* **10**, 3899 (2010).
- [28] T. P. Burg, M. Godin, S. M. Knudsen, W. Shen, G. Carlson, J. S. Foster, K. Babcock, S. R. Manalis, *Nature* **446**, 1066 (2007).
- [29] J. Lee, W. Shen, K. Payer, T. P. Burg, S. R. Manalis, *Nano Lett.* **10**, 2537 (2010).
- [30] R. A. Barton, B. Ilic, S. S. Verbridge, B. R. Cipriany, J. M. Parpia, H. G. Craighead, *Nano Lett.* **10**, 2058 (2010).
- [31] S. Timoshenko, D. H. Young, W. J. Weaver, *Vibration problems in engineering* (New York, Wiley [c1974], 1974), fourth edn.
- [32] S. Dohn, W. Svendsen, A. Boisen, O. Hansen, *Rev. Sci. Instrum.* **78**, 103303 (2007).
- [33] S. Dohn, S. Schmid, F. Amiot, A. Boisen, *Appl. Phys. Lett.* **97**, 044103 (2010).
- [34] M.-H. Bao, *Analysis and Design Principles of MEMS Devices*. (Elsevier, Amsterdam, 2005).
- [35] A. N. Cleland, *Foundations of Nanomechanics: from Solid-State Theory to Device Applications* (Springer-Verlag, Berlin Heidelberg, 2003).
- [36] M. I. Younis, *MEMS Linear and Nonlinear Statics and Dynamics*, Microsystems (Springer, New York; London, 2011).

- [37] J. Roels, Actuation of integrated nanophotonic devices through the optical gradient force, Phd thesis, Ghent University (2011).
- [38] D. Allan, *Proc. IEEE* **54**, 221 (1966).
- [39] G. Lifante, *Integrated Photonics: Fundamentals* (Wiley, Chichester, West Sussex, 2003), first edn.
- [40] W. Bogaerts, D. Taillaert, B. Luyssaert, P. Dumon, J. Van Campenhout, P. Bienstman, D. Van Thourhout, R. Baets, V. Wiaux, S. Beckx, *Opt. Express* **12**, 1583 (2004).
- [41] W. Bogaerts, R. Baets, P. Dumon, V. Wiaux, S. Beckx, D. Taillaert, B. Luyssaert, J. Van Campenhout, P. Bienstman, D. Van Thourhout, *Light. Technol. J.* **23**, 401 (2005).
- [42] V. R. Almeida, R. R. Panepucci, M. Lipson, *Opt. Lett.* **28**, 1302 (2003).
- [43] A. Sure, T. Dillon, J. Murakowski, C. Lin, D. Pustai, D. Prather, *Opt. Express* **11**, 3555 (2003).
- [44] D. Taillaert, W. Bogaerts, P. Bienstman, T. Krauss, P. Van Daele, I. Moerman, S. Verstuyft, K. De Mesel, R. Baets, *IEEE J. Quantum Electron.* **38**, 949 (2002).
- [45] D. Taillaert, P. Bienstman, R. Baets, *Opt. Lett.* **29**, 2749 (2004).
- [46] D. Taillaert, F. Van Laere, M. Ayre, W. Bogaerts, D. Van Thourhout, P. Bienstman, R. Baets, *Jpn. J. Appl. Phys.* **45**, 6071 (2006).
- [47] S. Scheerlinck, J. Schrauwen, F. Van Laere, D. Taillaert, D. Van Thourhout, R. Baets, *Opt. Express* **15**, 9625 (2007).
- [48] F. Van Laere, G. Roelkens, M. Ayre, J. Schrauwen, D. Taillaert, D. Van Thourhout, T. F. Krauss, R. Baets, *J. Light. Technol.* **25**, 151 (2007).
- [49] G. Roelkens, D. Vermeulen, D. Van Thourhout, R. Baets, S. Brisson, P. Lyan, P. Gautier, J.-M. Fedeli, *Appl. Phys. Lett.* **92**, 131101 (2008).

- [50] F. Van Laere, T. Claes, J. Schrauwen, S. Scheerlinck, W. Bogaerts, D. Taillaert, L. O'Faolain, D. Van Thourhout, R. Baets, *IEEE Photonics Technol. Lett.* **19**, 1919 (2007).
- [51] B. E. A. Saleh, M. C. Teich, *Fundamentals of Photonics* (Wiley, 1991), first edn.
- [52] K. Iizuka, *Elements of Photonics, Volume II: For Fiber and Integrated Optics* (Wiley-Interscience, New York, 2002).
- [53] K. Kawano, T. Kitoh, *Introduction to Optical Waveguide Analysis: Solving Maxwell's Equation and the Schrödinger Equation* (Wiley, New York, 2001).
- [54] B. Rahman, J. Davies, *J. Light. Technol.* **2**, 682 (1984).
- [55] B. Rahman, F. Fernandez, J. Davies, *Proc. IEEE* **79**, 1442 (1991).
- [56] E. Schweig, W. Bridges, *IEEE Trans. Microw. Theory Tech.* **32**, 531 (1984).
- [57] K. Bierwirth, N. Schulz, F. Arndt, *IEEE Trans. Microw. Theory Tech.* **34**, 1104 (1986).
- [58] V. Brankovic, D. Krupezevic, F. Arndt, *IEEE Trans. Microw. Theory Tech.* **40**, 2272 (1992).
- [59] W. Hofer, *IEEE Trans. Microw. Theory Tech.* **34**, 1464 (1986).
- [60] D. Sheen, S. Ali, M. Abouzahra, J. Kong, *IEEE Trans. Microw. Theory Tech.* **38**, 849 (1990).
- [61] K. S. Chiang, *Appl. Opt.* **25**, 2169 (1986).
- [62] I. De Vlaminck, J. Roels, D. Taillaert, D. Van Thourhout, R. Baets, L. Lagae, G. Borghs, *Appl. Phys. Lett.* **90**, 233116 (2007).

- [63] R. G. Hunsperger, *Integrated Optics: Theory and Technology* (Springer, 2009), 6th edn.
- [64] T. Baehr-Jones, M. Hochberg, C. Walker, A. Scherer, *Appl. Phys. Lett.* **86**, 081101 (2005).
- [65] M. Li, W. H. P. Pernice, H. X. Tang, *Appl. Phys. Lett.* **97**, 183110 (2010).
- [66] K. Y. Fong, W. H. P. Pernice, M. Li, H. X. Tang, *Appl. Phys. Lett.* **97**, 073112 (2010).
- [67] V. T. K. Sauer, Z. Diao, M. R. Freeman, W. K. Hiebert, *Appl. Phys. Lett.* **100**, 261102 (2012).
- [68] B. Little, J. Foresi, G. Steinmeyer, E. Thoen, S. Chu, H. Haus, E. Ippen, L. Kimerling, W. Greene, *IEEE Photonics Technol. Lett.* **10**, 549 (1998).
- [69] K. J. Vahala, *Nature* **424**, 839 (2003).
- [70] D. K. Armani, T. J. Kippenberg, S. M. Spillane, K. J. Vahala, *Nature* **421**, 925 (2003).
- [71] K. Srinivasan, H. Miao, M. T. Rakher, M. Davanço, V. Aksyuk, *Nano Lett.* **11**, 791 (2011).
- [72] P. H. Kim, C. Doolin, B. D. Hauer, A. J. R. MacDonald, M. R. Freeman, P. E. Barclay, J. P. Davis, *Appl. Phys. Lett.* **102**, 053102 (2013).
- [73] A. H. Safavi-Naeini, T. P. Mayer Alegre, J. Chan, M. Eichenfield, M. Winger, Q. Lin, J. T. Hill, D. E. Chang, O. Painter, *Nature* **472**, 69 (2011).
- [74] M. Eichenfield, J. Chan, R. M. Camacho, K. J. Vahala, O. Painter, *Nature* **462**, 78 (2009).
- [75] M. Notomi, *Reports Prog. Phys.* **73**, 096501 (2010).
- [76] A. C. Hryciw, P. E. Barclay, *Opt. Lett.* **38**, 1612 (2013).

- [77] W. H. P. Pernice, *J. Nanophotonics* **7**, 073095 (2013).
- [78] D. Van Thourhout, J. Roels, *Nat. Photonics* **4**, 211 (2010).
- [79] L. Novotny, B. Hecht, *Principles of nano-optics* (Cambridge University Press, Cambridge; New York, 2006).
- [80] M. L. Povinelli, M. Loncar, M. Ibanescu, E. J. Smythe, S. G. Johnson, F. Capasso, J. D. Joannopoulos, *Opt. Lett.* **30**, 3042 (2005).
- [81] Z. Diao, J. E. Losby, V. T. K. Sauer, J. N. Westwood, M. R. Freeman, W. K. Hiebert, *Appl. Phys. Express* **6**, 065202 (2013).
- [82] D. W. Carr, H. G. Craighead, *J. Vac. Sci. Technol. B Microelectron. Nanom. Struct.* **15**, 2760 (1997).
- [83] W. K. Hiebert, D. Vick, V. Sauer, M. R. Freeman, *J. Micromechanics Microengineering* **20**, 115038 (2010).
- [84] W. H. P. Pernice, M. Li, H. X. Tang, *Opt. Express* **17**, 12424 (2009).
- [85] W. H. P. Pernice, M. Li, H. X. Tang, *Opt. Express* **17**, 1806 (2009).
- [86] K. K. Lee, D. R. Lim, H.-C. Luan, A. Agarwal, J. Foresi, L. C. Kimerling, *Appl. Phys. Lett.* **77**, 1617 (2000).
- [87] V. T. K. Sauer, Z. Diao, M. R. Freeman, W. K. Hiebert, *Nanotechnology* **25**, 055202 (2014).
- [88] Y. Yang, C. Callegari, X. Feng, K. Ekinici, M. Roukes, *Nano Lett.* **6**, 583 (2006).
- [89] J. L. Arlett, M. L. Roukes, *J. Appl. Phys.* **108**, 084701 (2010).
- [90] H. W. C. Postma, I. Kozinsky, A. Husain, M. L. Roukes, *Appl. Phys. Lett.* **86**, 223105 (2005).
- [91] M. Li, W. H. P. Pernice, H. X. Tang, *Nat. Photonics* **3**, 464 (2009).

- [92] O. Basarir, S. Bramhavar, K. L. Ekinici, *Opt. Express* **20**, 4272 (2012).
- [93] O. Basarir, S. Bramhavar, K. L. Ekinici, *Nano Lett.* **12**, 534 (2012).
- [94] P. Dumon, Ultra-Compact Integrated Optical Filters in Silicon-on-insulator by Means of Wafer-Scale Technology, Phd thesis, Ghent University (2007).
- [95] M. L. Gorodetsky, A. Schliesser, G. Anetsberger, S. Deleglise, T. J. Kippenberg, *Opt. Express* **18**, 23236 (2010).
- [96] F. Tian, G. Zhou, F. Siong Chau, J. Deng, R. Akkipeddi, *Appl. Phys. Lett.* **102**, 081101 (2013).
- [97] M. Eichenfield, C. P. Michael, R. Perahia, O. Painter, *Nat. Photonics* **1**, 416 (2007).
- [98] J. Roels, I. De Vlaminck, L. Lagae, B. Maes, D. Van Thourhout, R. Baets, *Nat. Nanotechnol.* **4**, 510 (2009).
- [99] T. J. Kippenberg, K. J. Vahala, *Science* **321**, 1172 (2008).
- [100] W. E. Newell, *Science (80-. )*. **161**, 1320 (1968).
- [101] M. Li, H. X. Tang, M. L. Roukes, *Nat. Nanotechnol.* **2**, 114 (2007).
- [102] O. Svitelskiy, V. Sauer, N. Liu, K.-M. Cheng, E. Finley, M. R. Freeman, W. K. Hiebert, *Phys. Rev. Lett.* **103**, 244501 (2009).
- [103] O. Svitelskiy, V. Sauer, D. Vick, K.-M. Cheng, N. Liu, M. R. Freeman, W. K. Hiebert, *Phys. Rev. E* **85**, 056313 (2012).
- [104] B. A. Bircher, L. Duempelmann, K. Renggli, H. P. Lang, C. Gerber, N. Bruns, T. Braun, *Anal. Chem.* **85**, 8676 (2013).
- [105] C. K. Riener, C. M. Stroh, A. Ebner, C. Klampfl, A. A. Gall, C. Romanin, Y. L. Lyubchenko, P. Hinterdorfer, H. J. Gruber, *Anal. Chim. Acta* **479**, 59 (2003).

- [106] A. Bietsch, J. Zhang, M. Hegner, H. P. Lang, C. Gerber, *Nanotechnology* **15**, 873 (2004).
- [107] J. T. Kirk, G. E. Fridley, J. W. Chamberlain, E. D. Christensen, M. Hochberg, D. M. Ratner, *Lab Chip* **11**, 1372 (2011).
- [108] C. Boutopoulos, V. Tsouti, D. Goustouridis, S. Chatzandroulis, I. Zergioti, *Appl. Phys. Lett.* **93**, 191109 (2008).
- [109] V. T. K. Sauer, M. R. Freeman, W. K. Hiebert, *J. Micromechanics Microengineering* **20**, 105020 (2010).
- [110] G. Y. Chen, T. Thundat, E. A. Wachter, R. J. Warmack, *J. Appl. Phys.* **77**, 3618 (1995).
- [111] P. Lu, H. Lee, C. Lu, S. OShea, *Phys. Rev. B* **72**, 085405 (2005).
- [112] J. Tamayo, D. Ramos, J. Mertens, M. Calleja, *Appl. Phys. Lett.* **89**, 224104 (2006).
- [113] H. Craighead, *Nat. Nanotechnol.* **2**, 18 (2007).
- [114] E. Gil-Santos, D. Ramos, J. Martínez, M. Fernández-Regúlez, R. García, A. San Paulo, M. Calleja, J. Tamayo, *Nat. Nanotechnol.* **5**, 641 (2010).
- [115] D. Ramos, E. Gil-Santos, V. Pini, J. M. Llorens, M. Fernández-Regúlez, A. San Paulo, M. Calleja, J. Tamayo, *Nano Lett.* **12**, 932 (2012).
- [116] L. Cao, J. S. White, J.-S. Park, J. A. Schuller, B. M. Clemens, M. L. Brongersma, *Nat. Mater.* **8**, 643 (2009).
- [117] L. Cao, P. Fan, A. P. Vasudev, J. S. White, Z. Yu, W. Cai, J. A. Schuller, S. Fan, M. L. Brongersma, *Nano Lett.* **10**, 439 (2010).
- [118] G. Hernandez, *Appl. Opt.* **24**, 3062 (1985).
- [119] J. L. Arlett, E. B. Myers, M. L. Roukes, *Nat. Nanotechnol.* **6**, 203 (2011).
- [120] W. Hiebert, *Nat. Nanotechnol.* **7**, 278 (2012).

- [121] A. Sampathkumar, K. L. Ekinici, T. W. Murray, *Nano Lett.* **11**, 1014 (2011).
- [122] G. E. Keiser, *Opt. Fiber Technol.* **5**, 3 (1999).
- [123] B. Little, S. Chu, P. Absil, J. Hryniewicz, F. Johnson, F. Seiferth, D. Gill, V. Van, O. King, M. Trakalo, *IEEE Photonics Technol. Lett.* **16**, 2263 (2004).
- [124] G. T. Reed, A. P. Knights, *Silicon Photonics - An Introduction* (John Wiley & Sons Ltd, Chichester, West Sussex, 2004).
- [125] J. Bustillo, R. Howe, R. Muller, *Proc. IEEE* **86**, 1552 (1998).
- [126] J. W. Judy, *Smart Mater. Struct.* **10**, 1115 (2001).
- [127] K. Williams, K. Gupta, M. Wasilik, *J. Microelectromechanical Syst.* **12**, 761 (2003).
- [128] B. Ilic, S. Krylov, H. G. Craighead, *J. Appl. Phys.* **107**, 034311 (2010).
- [129] L.-Q. Xia, M. Chang, *Handb. Semicond. Manuf. Technol.*, R. Doering, Y. Nishi, eds. (CRC Press, Boca Raton, FL, 2008), chap. 13, second edn.
- [130] N. Kacem, J. Arcamone, F. Perez-Murano, S. Hentz, *J. Micromechanics Microengineering* **20**, 045023 (2010).
- [131] L. M. Fischer, N. Wilding, M. Gel, S. Evoy, *J. Vac. Sci. Technol. B Microelectron. Nanom. Struct.* **25**, 33 (2007).
- [132] S. S. Verbridge, J. M. Parpia, R. B. Reichenbach, L. M. Bellan, H. G. Craighead, *J. Appl. Phys.* **99**, 124304 (2006).
- [133] J. Brugger, J. W. Berenschot, S. Kuiper, W. Nijdam, B. Otter, M. Elwenspoek, *Microelectron. Eng.* **53**, 403 (2000).

- [134] J. Arcamone, M. Sansa, J. Verd, A. Uranga, G. Abadal, N. Barniol, M. van den Boogaart, J. Brugger, F. Pérez-Murano, *Small* **5**, 176 (2009).
- [135] M. Meyyappan, L. Delzeit, A. Cassell, D. Hash, *Plasma Sources Sci. Technol.* **12**, 205 (2003).
- [136] J. Westwater, D. P. Gosain, S. Tomiya, S. Usui, H. Ruda, *J. Vac. Sci. Technol. B Microelectron. Nanom. Struct.* **15**, 554 (1997).
- [137] F. Hillenkamp, J. Peter-Katalinic, eds., *MALDI MS: A Practical Guide to Instrumentation, Methods and Applications* (Wiley–VCH, Weinheim, 2007).
- [138] V. Sametoglu, V. T. K. Sauer, Y. Y. Tsui, *Opt. Express* **21**, 18525 (2013).

# Appendices

---

---

# APPENDIX A

---

## Publications

### A.1 Archival Journal

#### A.1.1 Published

- [1] Sauer, V.T.K., Diao, Z., Freeman, M.R., and Hiebert, W.K. Optical racetrack resonator transduction of nanomechanical cantilevers. *Nanotechnology* **25**, 055202-1-11 (2014).
- [2] Diao, Z., Losby, J., Burgess, A.J., Sauer, V.T.K., Hiebert, W.K., and Freeman, M.R. Stiction-free fabrication of lithographic nanostructures on resist-supported nanomechanical resonators. *Journal of Vacuum Science and Technology: B* **31**, 051805-1-5 (2013).
- [3] Sametoglu, V., Sauer, V.T.K., and Tsui, Y.Y. Production of 70-nm Cr dots by laser-induced forward transfer. *Optics Express* **21**, 18525-18531 (2013).
- [4] Diao, Z., Losby, J., Sauer, V.T.K., Westwood, J.N., Freeman, M.R., and Hiebert, W.K. Confocal scanner for highly sensitive photonic transduction of nanomechanical resonators. *Applied Physics Express* **6**, 065202-1-4 (2013).

- [5] Sametoglu, V., Sauer, V., and Tsui, Y.Y. Nanoscale Laser-Induced Forward Transfer Through Patterned Cr Films. *Applied Physics A: Materials Science & Processing* **110**, 823-827 (2013).
- [6] Gupta, M., Sauer, V., and Tsui, Y.Y. Pulsed Laser Deposition of uniform semiconductor nanodot arrays. *Applied Physics A: Materials Science & Processing* **110**, 817-821 (2013).
- [7] Sauer, V.T.K., Diao, Z., Freeman, M.R., and Hiebert, W.K. Nanophotonic detection of side-coupled nanomechanical cantilevers. *Applied Physics Letters* **100**, 261102-1-4 (2012).
- [8] Svitelskiy, O., Sauer, V., Vick, D., Cheng, K.M., Liu, N., Freeman, M.R., and Hiebert, W.K. Nanoelectromechanical devices in a fluidic environment. *Physical Review E* **85**, 056313-1-12 (2012).
- [9] Hiebert, W.K., Vick, D., Sauer, V., and Freeman, M.R. Optical interferometric displacement calibration and thermomechanical noise detection in bulk focused ion beam fabricated nanoelectromechanical systems. *Journal of Micromechanics and Microengineering* **20**, 115038-1-11 (2010).
- [10] Sauer, V.T.K., Freeman, M.R., and Hiebert, W.K. Device overshield for mass-sensing enhancement (DOME) structure fabrication. *Journal of Micromechanics and Microengineering* **20**, 105020-1-6 (2010).
- [11] Vick, D., Sauer, V., Fraser, A.E., Freeman, M.R., and Hiebert, W.K. Bulk focused ion beam fabrication with 3-dimensional shape control of nanoelectromechanical systems. *Journal of Micromechanics and Microengineering* **20**, 105005-1-9 (2010).
- [12] Davis, J.P., Vick, D., Burgess, J.A.J., Fortin, D.C., Li, P., Sauer, V., Hiebert, W.K., and Freeman, M.R. Observation of magnetic supercooling of the transition to the vortex state. *New Journal of Physics* **12**, 093033-1-10 (2010).

- [13] Svitelskiy, O., Sauer, V., Liu, N., Cheng, K.M., Finley, E., Freeman, M.R., and Hiebert, W.K. Pressurized Fluid Damping of Nanoelectromechanical Systems. *Physical Review Letters* **103**, 244501-1-4 (2009).
- [14] Liu, N., Giesen, F., Belov, M., Losby, J., Moroz, J., Fraser, A.E., McKinnon, G., Clement, T.J., Sauer, V., Hiebert, W.K., and Freeman, M.R. Time-domain control of ultrahigh-frequency nanomechanical systems. *Nature Nanotechnology* **3**, 715-719 (2008).
- [15] Svitelskiy, O., Liu, N., Sauer, V., Cheng, K.M., Finley, E., Belov, M., Freeman, M.R., and Hiebert, W.K. A simple cell for the analysis of nanoelectromechanical systems under gas pressure. *Review of Scientific Instruments* **79**, 093701-1-5 (2008).

### A.1.2 In review

- [1] Westwood, J., Sauer, V.T.K., Kwan, J.K, Hiebert, W.K., and Sit J., Fabrication of high surface area nanoelectromechanical systems via the integration of glancing angle deposition thin films. *Journal of Micromechanics and Microengineering* (in review).

## A.2 Book Chapters

### A.2.1 In review

- [1] Sauer, V.T.K., Diao, Z., and Hiebert, W.K. Cantilever resonance detection using nanophotonic structures. *Nanocantilever Beams: Modeling, Fabrication and Applications* Editors: Mona Zaghoul, Ioana Voiculescu. Pan Stanford Publishing (in review with editors as of November 2013).

### A.3 Selected conference presentations

- [1] Sauer, V.\*, Diao, Z., Freeman, M.R., and Hiebert, W.K. Multiplexed nanomechanical devices and single wavelength nanophotonic actuation and detection. Oral presentation at *AVS 60th International Symposium and Exhibition*, Long Beach, California, Oct. 27-Nov. 1 (2013).
- [2] Sauer, V.\*, Diao, Z., Freeman, M.R., and Hiebert, W.K. Nanomechanical displacement detection using racetrack resonator optical cavities. Poster presentation at *10th International Workshop on Nanomechanical Sensing*, Stanford, California, May 1-3 (2013).
- [3] Sauer, V.\*, Diao, Z., Freeman, M.R., and Hiebert, W.K. Nanomechanical resonator detection using racetrack resonator structures for use in mass sensing. Oral presentation at *AVS 59th International Symposium and Exhibition*, Tampa, Florida, Oct. 28-Nov. 2 (2012).
- [4] Sauer, V.\*, Diao, Z., Freeman, M.R., and Hiebert, W.K. Detection of Resonant Cantilevers using the Evanescent Fields of Silicon Nanophotonic Waveguides. Oral presentation at *International Conference on Nanoscience and Technology*, Paris, France, July 23-27 (2012).
- [5] Sauer, V.\*, Diao, Z., Freeman, M.R., and Hiebert, W.K. Detection of Resonant Cantilevers using the Evanescent Fields of Silicon Nanophotonic Waveguides. Oral presentation at *SPIE Photonics West*, San Francisco, CA, Jan. 21-26 (2012).
- [6] Sametoglu, V., Sauer, V.\*, and Tsui, Y.Y. Nanoscale Laser-Induced Forward Transfer through patterned Cr films. Poster presented at *COLA 2011*, Playa del Carmen, MX, Nov. 13-19 (2011).
- [7] Gupta, M., Sauer, V.\*, and Tsui, Y.Y. Pulsed Laser Deposition of Uniform Semiconductor Nanodot Arrays. Poster presented at *COLA 2011*, Playa del Carmen, MX, Nov. 13-19 (2011).

- [8] Sauer, V.\*, Freeman, M.R., and Hiebert, W.K. Fabrication of Device Over-shields for Use in Mass Sensing. Poster presented at *7th International Conference on Nanomechanical Cantilever Sensors*, Banff, AB, May 26-28 (2010).
- [9] Sauer, V.\*, Freeman, M.R., and Hiebert, W.K. Device Overshield for Mass-sensing Enhancement (DOME) Fabrication. Poster presented at *MRS Spring Meeting*, San Francisco, April 5-9 (2010).
- [10] Sauer, V.\*, Freeman, M.R., and Hiebert, W.K. Fabrication of a NEMS Resonator Over-shield for Mass Sensing. Oral presentation at *APS March Meeting*, New Orleans, LA, Mar 10-14 (2008).